ANALYSIS AND MODELING OF DIFFUSE ULTRASONIC SIGNALS FOR STRUCTURAL HEALTH MONITORING

A Thesis
Presented to
The Academic Faculty

by

Yinghui Lu

In Partial Fulfillment
of the Requirements for the Degree
Doctor of Philosophy in the
School of Electrical and Computer Engineering

Georgia Institute of Technology
August 2007

ANALYSIS AND MODELING OF DIFFUSE ULTRASONIC SIGNALS FOR STRUCTURAL HEALTH MONITORING

Approved by:

Professor Jennifer E. Michaels,
Advisor
School of Electrical and Computer
Engineering
Georgia Institute of Technology

Professor Gregory D. Durgin
School of Electrical and Computer
Engineering
Georgia Institute of Technology

Professor Thomas E. Michaels
School of Electrical and Computer
Engineering
Georgia Institute of Technology

Professor Laurence J. Jacobs
School of Civil and Environmental
Engineering
Georgia Institute of Technology

Professor George Vachtsevanos
School of Electrical and Computer
Engineering
Georgia Institute of Technology

Date Approved: June 15, 2007

To my wife, I-Wen

for her patience, support, and unending love

ACKNOWLEDGEMENTS

I would like to earnestly thank my advisor, Dr. Jennifer Michaels, for her excellent guidance and patience, and for providing me with an excellent atmosphere for doing research. Throughout my doctoral work, Dr. Michaels always gave me the freedom to pursue my own interests and provided valuable guidance and support. Dr. Michaels frequently brought new ideas to my research, solved many technical details with me, encouraged me to develop independent thinking and research skills, greatly assisted me with scientific writing, and often worked long hours with me. Dr. Michaels loves research and teaching, and her dedication to her career has continually inspired me. Jenny, thanks for everything. As your student, I will always refer to your advice throughout my career and try to prove that your effort is not in vain.

I would like to thank Dr. Thomas Michaels for providing valuable advice on many of my experiments, teaching me how to make ultrasonic transducers and use experimental equipments, spending countless time in reading and revising my papers throughout my doctoral research, and as one of my doctoral committee members, encouraging and helping me to finish my dissertation.

I am very grateful for having an exceptional doctoral committee and wish to thank Dr. Laurence Jacobs, Dr. George Vachtsevanos, and Dr. Gregory Durgin for their continual support and encouragement.

This research was funded by the National Science Foundation through contract number ECS-0401213, and I am grateful for the support.

I wish to thank Dr. John Chiasson and Dr. Leon Tolbert. They were my advisor and co-advisor when I was studying for my Master's degree in the University of Tennessee at Knoxville. Dr. Chiasson enrolled me in his research group from China

in 2000, which provided me the opportunity to start my journey of graduate studies in the United States. Dr. Tolbert encouraged me to pursue the Ph.D. degree. Without his encouragement and help, I would not have had the courage and opportunity to obtain this degree from Georgia Tech.

I am extremely grateful to Mr. Li Cheng, my best friend for more than a decade. Li and I came to the United States for graduate study together in 2000. During the past seven years, he has been a constant source of good advice, good conversation, and good times.

I would like to thank my father, Mingjian Lu, and my mother, Hanfen Wu. Their intellectual guidance put me on this path at an early age; this is partly their achievement. Even though I have been living on the opposite side of the world for the past seven years, they have always found a special way to care for me. I constantly feel the warmth of my family through their sharing cooking tips with me over the phone, and preparing and mailing packages to me.

I am grateful to my younger brother, Yinghua, for his unconditional encouragement and good advice. Since he moved to Atlanta in 2005 for his graduate study, we have spent many good times together, which is something I cherish a lot and hope we can have many more to come in the future.

TABLE OF CONTENTS

LIST OF TABLES

LIST OF FIGURES

SUMMARY

Structural Health Monitoring (SHM) refers to the process of nondestructive autonomous *in situ* monitoring of the integrity of critical structures such as airplanes, bridges and buildings. Ultrasonic wave propagation is an ideal interrogation method for SHM because ultrasound is the elastic vibration of the material itself and is thus directly affected by any structural damage occurring in the paths of the propagating waves. Such methods have been the subject of much research, where the primary emphasis has been the use of narrowband guided ultrasonic waves which are tuned to the specific structure being monitored. An alternative is to use broadband diffuse waves which are readily generated by an impulse excitation and formed from the scattering from microstructure or the reflections from structural boundaries over a long time interval. They are an appealing interrogation tool for SHM because of their simple excitation, independence of structure, and large volume coverage. The difficulties of using diffuse ultrasonic waves for SHM are the complex nature of the received signals and their sensitivity to environmental changes, such as temperature and surface condition changes, compared to damage.

The objective of this thesis is to provide a comprehensive damage detection strategy for SHM using diffuse ultrasonic waves. This strategy includes a systematic temperature compensation method, differential feature extraction methods optimized for discriminating benign surface condition changes from damage, and data fusion methods to determine the structural status.

The temperature compensation method is based upon a set of pre-recorded baselines. Using the methods of baseline selection and baseline correction, a baseline that best matches a monitored signal in temperature is provided.

For the differential feature extraction, three types of features are proposed. The first type includes basic differential features such as mean squared error. The second type is derived from a matching pursuit based signal decomposition. An ultrasonic signal is decomposed into a sum of characteristic wavelets, and differential features are extracted based upon changes in the decomposition between a baseline signal and a monitored signal. The third type is a phase space feature extraction method, where an ultrasonic signal is embedded into phase space and features are extracted based on changes of the phase portrait.

The structural status is determined based on a data fusion strategy consisting of a threshold selection method, fusion at the feature level, and fusion at the sensor level.

The proposed damage detection strategy is applied to experiments on aluminum specimens with artificial defects subjected to a variety of environmental variations. Results as measured by the probability of detection, the false alarm rate, and the size of damage detected demonstrate the viability of the proposed techniques.

Major contributions of this thesis are:

- Development and implementation of a comprehensive strategy for damage detection for structural health monitoring based on diffuse ultrasonic signals
- Investigation of the combined effects of temperature and damage on diffuse ultrasonic waves, and development of a temperature compensation method
- Development of distributed and constrained matching pursuit signal decomposition methods for diffuse ultrasonic signals
- Implementation and demonstration of phase space feature extraction for monitoring of changes in diffuse ultrasonic signals
- Implementation and demonstration of feature and sensor fusion for damage detection using diffuse ultrasonic waves

CHAPTER I

INTRODUCTION

Structural Health Monitoring (SHM) refers to the process of the nondestructive autonomous *in situ* damage detection and evaluation of engineering structures. For aerospace, civil, and mechanical industries, technologies for earlier damage identification in both manufacturing and service processes are demanded by the impact of product quality and the safety during the life of service. SHM provides an efficient solution because of the capability of long term *in situ* damage detection and the cost effectiveness resulted from in-service evaluation and minimal human involvement.

The objective of this thesis is to develop a foundation for using diffuse ultrasonic waves as the interrogation method for SHM. The research focuses on the signal processing and modeling of diffuse ultrasonic waves for feature extraction, feature and sensor fusion methods for decision making, as well as methodologies to compensate the effects of benign environmental changes, including temperature and surface condition changes, to provide a comprehensive strategy for damage detection.

The remainder of this chapter introduces the background of SHM (Sec. 1.1), identifies the motivation for this research and the problems to solve (Sec. 1.2), summarizes the contributions of the research (Sec. 1.3), and provides the organization of the remaining chapters (Sec. 1.4).

1.1 Background

SHM is a newer approach for damage identification compared to Nondestructive Testing and Evaluation (NDT&E). NDT&E is primarily used for damage detection and characterization after a possible damage location has been identified. Inspection is usually carried out off-line where actuators and sensors are temporarily coupled to

the specimen in the vicinity of possible locations of damage. For SHM, actuators and sensors are permanently mounted on or embedded in the structure so that on-line *in situ* monitoring is possible. In addition, if actuators and sensors are distributed, SHM provides the capability of global structural monitoring rather than a local inspection as is typical for NDT&E methods.

There are different approaches for SHM according to the specific application. First, an SHM system can monitor the structure in an active or a passive manner. For the active method, the structure is excited by actuators and the system response is received by sensors. For the passive method, actuators are not required and the response of the structure is captured by "listening" sensors. Second, an SHM system can be designed to have a local or a global monitoring capability using different choices of actuators and sensors combined with different interrogation mechanisms. Third, for damage detection, the recorded measurements for an SHM system can be processed in two ways. One is to directly analyze the measured signals to determine the structural status, and the other is to compare a measured signal to historical records and identify the structural status based on the change of measurements at different times. The latter approach is available for SHM because signals recorded from permanently mounted sensors are repeatable, which is generally not practical for NDT&E due to long intervals between inspections and variations in sensors and coupling conditions.

Passive SHM methods rely on either excitation from the environment, such as the vibrations of bridges, buildings, and airplanes experienced during normal operation, or from the damage mechanism itself such as the elastic waves resulting from an impact or generated by acoustic emissions from a growing crack. Passive methods have the advantage of not requiring actuators, but have the serious disadvantage of having uncontrolled and possibly inadequate excitations.

For active interrogation, the vibration-based method and ultrasonic wave propagation method are two major accepted diagnostic methods [1]. The principle of the vibration-based method is to excite vibrations in the structure, measure the response, determine one or more physical properties of the structure (e.g. stiffness), and then correlate changes in physical properties to the integrity of the structure. According to the extent of the vibration, vibration-based methods can be further divided into two approaches: global vibrations and local vibrations. For the global vibration method, low-frequency global responses of the structure are normally measured. Physical properties such as mass, stiffness and damping, and modal parameters such as natural frequency and mode shape, are correlated to the structural integrity [2]. For the local vibration method, high-frequency ($>\sim$ 30 KHz) vibrations are excited locally by an active sensor such as a piezoelectric wafer, and change in electro-mechanical (E/M) impedance is used to detect damage [3, 4, 5]. Fig. 1 is a flowchart for a generic SHM system using the active interrogation method where the differential signal analysis method is used for damage detection.

The primary difficulty with the global vibration method is that damage is typically a local phenomenon and thus may not have a significant influence on the low-frequency vibrations of the structure [6]. The local vibration method is more sensitive to damages because of its high-frequency excitation, but the interrogation area is limited.

The idea of the ultrasonic wave propagation method is to interrogate the structure using active ultrasound. Elastic waves with frequency higher than 20 KHz are called ultrasound because they are not audible. For industrial applications, typical frequencies range from 100 KHz to 25 MHz, with some applications as high as $100 - 200$ MHz. Because ultrasonic waves are elastic vibrations of the material itself, they are directly affected by any structural changes occurring in the paths of the propagating waves. Therefore, ultrasound is an ideal method for damage detection. The detection sensitivity can approach the microstructural level when high-frequency transducers

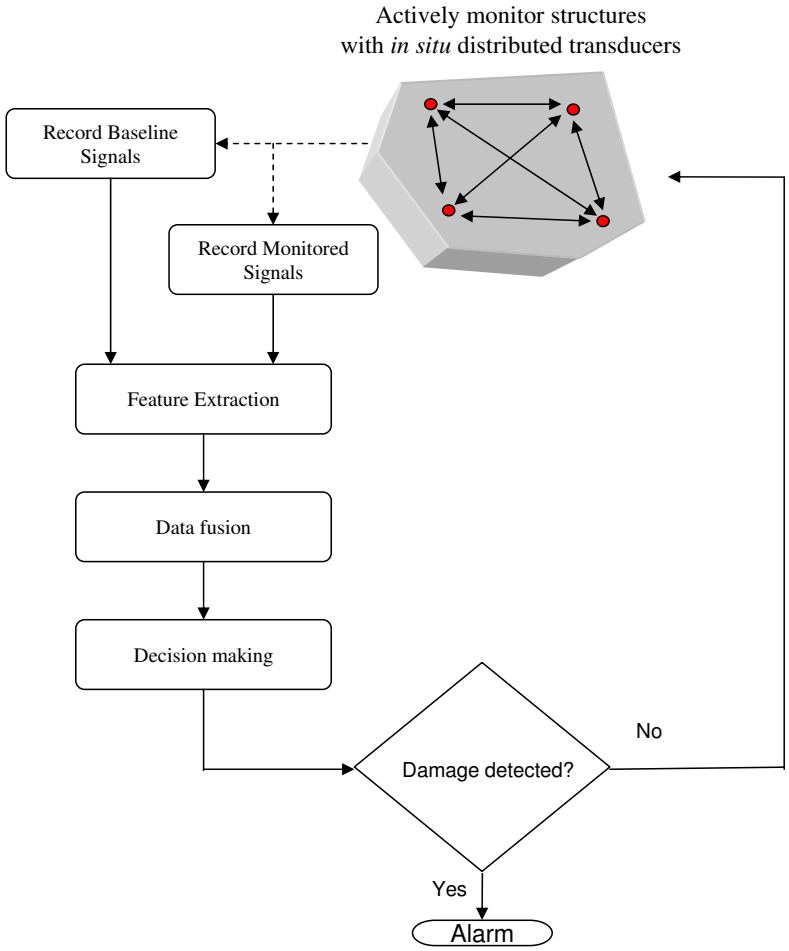

Figure 1: A basic flowchart of structural health monitoring using active interrogation and differential signal analysis method.

are used.

Ultrasonic waves can be produced and received by many techniques for different applications. For example, electromagnetic acoustic transducers (EMATS) can generate and receive ultrasonic waves in metals using the electromagnetic effects [7]. For solids, a laser can be used to generate ultrasound by the thermoelastic effect, and the waves can be received by laser interferometers. For SHM, transducers made from piezoelectric materials such as lead zirconate titanate (PZT) are appealing because they are applicable to virtually any type of structure; each transducer can be used as an actuator or sensor; and they are easy to mount on or embed in the structure.

Recently, piezoelectric transducers made from the piezoelectric wafer alone, without backing materials, have been proposed to enable sensor embedding, and they are frequently referred to as piezoelectric wafer active sensors (PWAS) [8]. In addition, a thin dielectric film with an embedded network of distributed piezoelectric transducers is patented for SHM [9]. Such thin layers can be surface-mounted on metallic structures or embedded inside composite structures.

For ultrasonic SHM, ultrasonic waves can either be generated by one transducer and received by another one in a different location on the structure, or generated and received by the same transducer. Depending upon the geometry of the structure and the time of the received signal, it is possible to interrogate a large material volume with a small number of sensor. If properly designed, the ultrasonic wave propagation method can have a global monitoring capability similar to that of the global vibration method. Moreover, it can still be sensitive to local damage because of the wavelength of the ultrasonic waves.

The global ultrasonic wave propagation method can also be divided into two categories according to two types of waves used for interrogation, namely, guided ultrasonic waves and diffuse ultrasonic waves.

Guided ultrasonic waves refer to well-behaved wave modes formed and traveling in structures with particular shapes, such as rods, plates, and pipes. Examples of guided ultrasonic waves are Lamb waves, Rayleigh waves, and Love waves. They have been extensively used for SHM because for simple structures, sensors can be designed so that waveforms can be interpreted to provide information concerning damage.

A diffuse ultrasonic field is defined as one in which wave modes of all propagation directions and frequencies are excited with random amplitudes that are independent to each other and random phases that are uniformly distributed [10]. A strictly diffuse ultrasonic field is rarely realized in practice, but diffuse-like ultrasonic waves can be generated by an impulse excitation and formed from the waves scattered from

microstructure or the reflections from structural boundaries over a long time interval [11]. Because diffuse (or diffuse-like) ultrasonic waves result in complex measured signals, it is difficult to analyze or simulate the waveforms using physical models. Therefore, they have not been considered for very many SHM applications.

1.2 Motivation and Problem Statement

Several active interrogation methods that can be used for SHM were introduced in the previous section and are summarized in Fig. 2. For the global wave propagation methods, guided waves have been extensively studied and applied for SHM, while diffuse ultrasonic waves have not been the subject of much research.

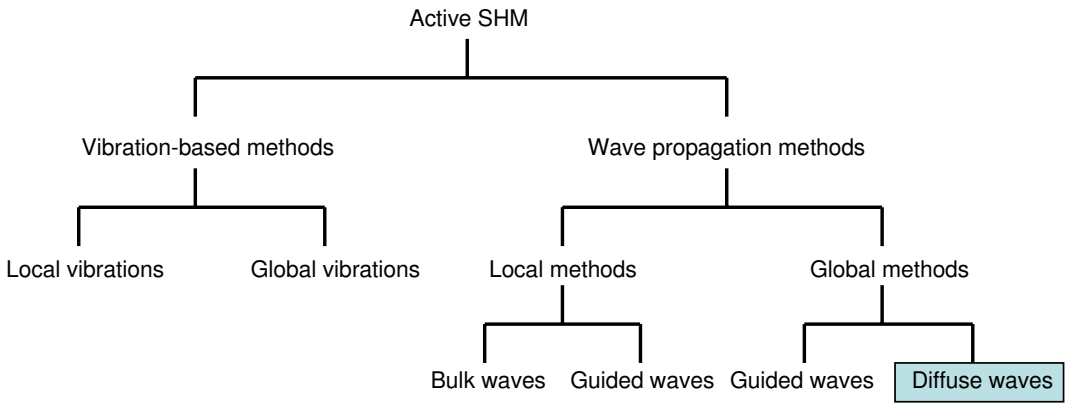

Figure 2: Active interrogation methods for structural health monitoring

However, there are three attractive reasons to use diffuse ultrasonic waves for SHM. First, compared to vibration-based methods, SHM using diffuse ultrasonic waves is able to interrogate a large volume with much higher sensitivity using a small number of sensors. Second, compared to guided ultrasonic waves, diffuse ultrasonic waves can almost always be generated in a bounded structure regardless of its geometry and complexity. Third, the generation and reception of diffuse ultrasonic waves are simple and structure-independent. They can be generated by an impulse or tone

burst and received by any broadband receive transducers, while the excitation of specific guided ultrasonic wave modes has to be tuned according to a specific structural geometry. Therefore, using diffuse ultrasonic waves for SHM can be advantageous and is often the only realistic option.

The difficulties of using diffuse ultrasonic waves for SHM exist in two aspects. First, it is difficult to analyze the complex ultrasonic signals. There are no accepted methods to correlate changes in diffuse ultrasonic signals with the status of the structure being interrogated.

Second, diffuse ultrasonic signals are sensitive not only to structural damage, but also to benign environmental changes such as temperature and surface condition changes. In fact, these environmental changes also affect guided ultrasonic waves, although they may not obscure responses from damage for single modes. However, in either case, effects of environmental changes have not been the subject of many investigations since laboratory conditions are typical for most reported research.

For these reasons, the subject of this thesis is to develop a comprehensive damage detection strategy to provide a foundation for using diffuse ultrasonic waves for SHM. This strategy includes a systematic compensation method for temperature variations, differential feature extraction methods optimized for discriminating benign surface condition changes from damage, and data fusion methods for the declaration of the structural status as "damaged" or "undamaged".

1.3 Contributions

The first and most important contribution of this research is a comprehensive damage detection strategy for SHM using diffuse ultrasonic waves. The research results demonstrate the feasibility of using diffuse ultrasonic waves for SHM and provide a foundation for future research.

The second contribution of this research is that it investigates the combined effects

of temperature and damage on diffuse ultrasonic waves for SHM, and develops a systematic temperature compensation method.

The third contribution of this thesis is that it develops and implements a numerical implementation method of matching pursuit signal decomposition for ultrasonic signals. Based on this implementation, distributed and constrained matching pursuit decomposition methods are proposed and implemented for extracting features from diffuse ultrasonic signals.

The fourth contribution of this thesis is that it implements and demonstrates a phase space feature extraction method for diffuse ultrasonic signals based on embedding theory and chaos theory.

The fifth contribution of this thesis is that it implements and demonstrates the feature and sensor fusion methods for damage detection using diffuse ultrasonic waves.

1.4 Thesis Outline

The remainder of the thesis is organized as follows. Chapter II presents a review of the existing literature and the state-of-art for ultrasonic diffuse waves to provide a deeper background and foundation for the thesis. The literature survey focuses on the background of diffuse ultrasonic waves, their prior application to NDT&E and SHM, and the effects of benign environmental changes on diffuse ultrasonic waves. At the end of the chapter, the objective and scope of the research presented in this thesis is placed in the context of the review work.

Chapter III describes the setups, measurements, and recorded data from three experiments that are designed to investigate the subjects of this thesis. The first two experiments are designed to study the effects of both damage and temperature changes on diffuse ultrasonic waves. The third experiment is conducted to investigate the effects of surface condition changes, including surface wetting and contact.

Chapter IV introduces the theory and mathematical methods that are used in

this thesis. First, the theory of temperature effects on diffuse ultrasonic waves developed by Weaver [11] is explained and then illustrated using experimental data. Second, the theory of matching pursuit decomposition is introduced, and a numerical implementation designed for ultrasonic signal decomposition is proposed. Methods of distributed and constrained matching pursuit decomposition are also proposed for extracting features from changes in diffuse ultrasonic waves. Third, the theory of embedding and chaotic signals is introduced, which is used later for the phase space feature extraction.

Chapter V proposes the overall damage detection procedure for SHM with diffuse ultrasonic waves. It consists of a systematic temperature compensation method, feature extraction methods, and data fusion strategies to improve the performance of an SHM system. In the end of Chapter V, feature extraction techniques using the theory of embedding are introduced separately, providing a preliminary study on phase space feature extraction for diffuse ultrasonic waves.

Chapter VI presents the experimental results. First, the efficacy of the temperature compensation method with various sizes of baseline sets is evaluated. Second, the proposed feature extraction methods combined with the feature fusion and sensor fusion strategies are applied to the experimental data, demonstrating the overall performance of an SHM system for damage detection. Finally, the results of the phase space feature extraction method are presented.

Chapter VII concludes this thesis and gives recommendations for future research.

CHAPTER II

REVIEW OF DIFFUSE ULTRASONIC WAVES

This chapter serves as a review of diffuse ultrasonic waves to provide the necessary background and foundation for the research presented in this thesis. In Sec. 2.1, an overview of ultrasonic wave propagation is given. In Sec. 2.2, the background of diffuse ultrasonic waves is reviewed along with applications to both NDT&E and SHM. Then, in Sec. 2.3, research related to environmental effects on diffuse ultrasonic waves is reported. Finally, In Sec. 2.4, the objective and scope of the research of this thesis is placed in the context of prior work.

2.1 Overview of Ultrasonic Wave Propagation

Ultrasonic waves in solid, also called elastic waves or stress waves, are of great interest because of their continued critical role in the interrogation of engineering structures for damage. Both bulk and guided wave mode are briefly reviewed.

2.1.1 Bulk Ultrasonic Waves

In an infinite isotropic solid medium, two basic ultrasonic wave modes can exist, namely longitudinal waves and transverse waves. For longitudinal waves (also called pressure waves, primary waves or P-waves), the direction of particle motion is parallel to the direction of propagation. For transverse waves (also called shear waves, secondary waves, or S-waves), the direction of particle motion is normal to the direction of propagation, and there are two polarizations. Both longitudinal and shear waves are called bulk waves. They are non-dispersive, meaning that their speeds only depend on the properties of the medium, e.g., Lamé constants and density.

2.1.2 Guided Ultrasonic Waves

If waves propagate in a medium with boundaries, multiple reflections and mode conversions occur, causing constructive and destructive interferences. As a result, more complicated but well-behaved wave modes can be formed which travel in the structure. These waves are called guided waves and the structure that forces the formation of the guided waves is referred to as the wave guide. Some natural wave guides are plates, rods, pipes, and multi-layer structures. Guided waves are often dispersive, i.e., their speeds depend upon frequency in addition to material properties and geometrical parameters.

2.1.2.1 Surface Acoustic Waves

Surface acoustic waves are evanescent waves that propagate along the surface of a medium and whose propagating disturbance decays exponentially with the distance from the surface [12]. This type of ultrasonic wave was first discovered in 1887 by Lord Rayleigh, who proved that on the free surface of an elastic half-space, an elastic wave can travel along the surface and localize its disturbance energy in the vicinity about one wavelength from the surface. These surface waves which are non-dispersive are the simplest ultrasonic guided waves, and are called Rayleigh waves. In 1924, Stoneley recognized that a surface wave can sometimes exist at the interface between two solid materials, and it is called a Stoneley wave. In 1926, Love showed that shear horizontal (SH) waves in a thin layer attached to a host medium with different elastic properties can support a surface wave in the host medium. Such waves are consequently called Love waves.

Silk [13] did early research on the use of Rayleigh waves for surface crack detection based upon time delay measurements. Resch et al. [14, 15] applied Rayleigh waves to monitor the growth of surface fatigue cracks. Yuce et al. studied Rayleigh waves for fatigue crack detection in aluminum and steel by calculating the so-called

reflection coefficient. The reflection coefficient was also used by Khuri-Yakub and Kino for surface crack detection in ceramics [16]. For monitoring applications, several researches have applied Rayleigh waves to track fatigue crack growth [17, 18, 19]. Besides Rayleigh waves, Love waves and Stoneley waves have also been investigated for surface-breaking crack detection [20, 21].

In addition to the above classical surface waves, a wave mode called the subsurface longitudinal (SSL) wave has also been investigated for near-surface inspection. It is a longitudinal wave traveling underneath and along the surface after a longitudinal wave is incident on the surface at or near the first critical angle [22]. For SSL waves, there is no disturbance decay with the distance from the surface, as they only exist in close proximity to the surface. Therefore, SSL waves are suited for crack detection in subsurface layers of isotropic materials [23, 24]. Some authors also call SSL waves head waves or creeping waves.

2.1.2.2 Lamb Waves and Shear Horizontal Waves

Lamb waves and SH waves are two types of guided waves that can propagate in plates. Because they can travel a long distance in a plate and are well understood both in mathematics and mechanics, they are commonplace in the inspection of plate-like structures, such as airplane wings, rolled steel sheets, and ship hulls.

Lamb waves occur when the thickness of the plate is of the same order as the wavelength. According to the modes of particle motion, there are two types of Lamb waves; i.e., symmetric and asymmetric Lamb waves, as shown in Fig. 3. Lamb waves are governed by the well-known Rayleigh-Lamb frequency equation [12]. The solutions of the equation result in dispersion curves, which relate frequency and wave number for all possible Lamb wave modes.

Lamb waves are frequently used for the damage detection and characterization in plate-like specimens. Usually, a single mode is excited in the specimen and the

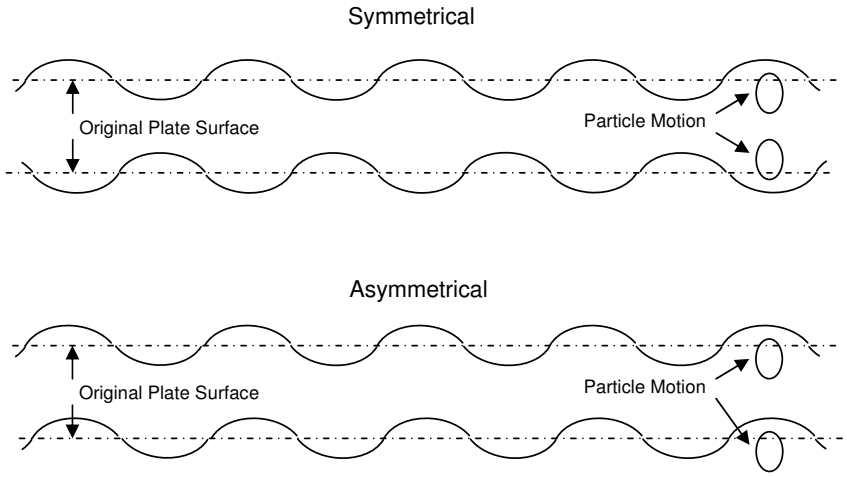

Figure 3: Illustration of Lamb wave propagation

damage is evaluated by the changes of the waveform. Comprehensive reviews on Lamb waves for SHM and NDT&E can be found in [25, 26] and [27, 28], respectively. One key issue for using Lamb waves is that of wave mode tuning for specific applications. For example, in the inspection of water-loaded structures, the energy of the Lamb wave could leak into the water if there is significant out-of-plane particle motion. In such a case, a particular mode in the dispersion curves should be selected so that the out-of-plane particle motion is minimized [29, 30].

The SH wave differs from the Lamb wave in that the former only has in-plane particle motion and the direction of particle motion is perpendicular to the direction of propagation. It has advantages over the Lamb wave in certain applications. For example, for the water-loaded structures, shear horizontal waves intrinsically would not leak energy because of their pure in-plane particle motion.

The choice of Lamb or SH waves for structural inspection is application dependent. For instance, in [31], the SH wave is shown to have better performance for ship hull inspection, while in [32], the Lamb wave is demonstrated to perform better for inspection of cold rolled steel sheets.

2.1.2.3 Ultrasonic Phased Arrays for Guided Waves

The traditional method for guided wave generation is to use wedge transducers to produce an angle beam incident in the structure. The direction of wave propagation is determined by the position and angle of the transducer. For Lamb waves and SH waves, a specific mode can be obtained by tuning the transducer center frequency and the incident angle.

As an alternative, an ultrasonic phased array can excite guided ultrasonic waves which can be electronically controlled in direction, amplitude, and mode. Thus, transducer replacement and movement are dramatically reduced for NDT&E, and a larger area can be interrogated. Using a phased array for NDT&E was first shown in Viktorov's book in 1967 [33]. The mechanism of controlling the direction of propagation and mode selection is well introduced in [34, 35]. In Fig. 4, several modes of a linear ultrasonic phased array are illustrated. In addition to these generation mode, interdigital array elements are frequently used to generate specific Lamb wave modes by adjusting their spacing and frequency of excitation [36, 37].

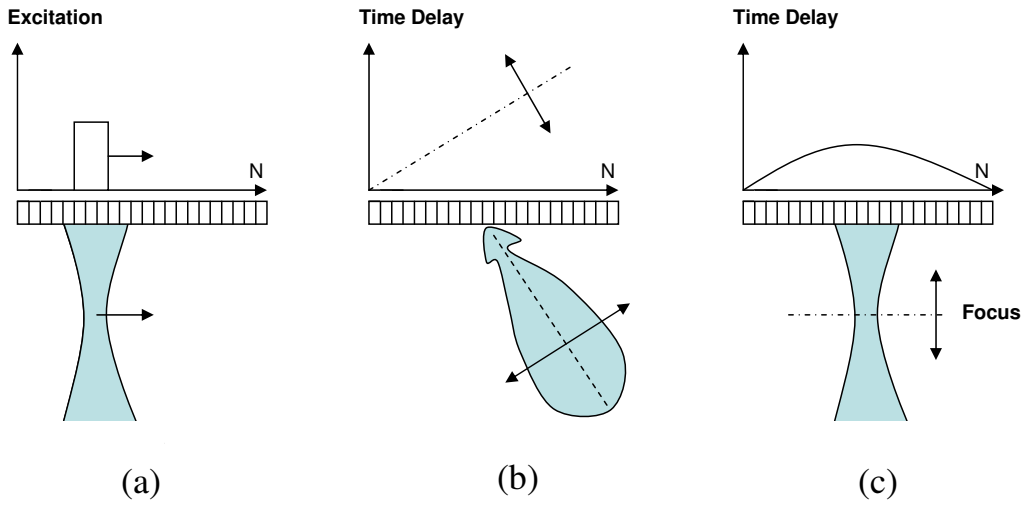

Figure 4: Example of electronically controlled ultrasonic beams using Phase arrays. (a) Parallel scanning, (b) Angular scanning, (c) Variation of focusing

Because of the capability of electronic propagation direction control and mode selection, ultrasonic guided wave phases arrays have been studied and applied to both SHM and NDT&E. In [38], the authors give a mathematical model of a comb transducer phased array with regard to the transducer design for NDT&E. In [39, 40], different array transducers and synthetic phase tuning methods are proposed for wave mode selection. Wilcox *et al.* [41, 42] proposed and implemented omnidirectional Lamb wave array using EMATS and including dispersion compensation. Giurgiutiu and Yu *et al.* implemented the ultrasonic phased array using embedded piezoelectric wafers for SHM, which they called embedded ultrasonic structural radar (EUSR) [43, 44]. Applications in thin plate and cylindrical specimens and signal processing issues are given in their papers.

2.2 Diffuse Ultrasonic Waves

All the guided wave modes introduced in the previous section are structure dependent, and tuning excitation is required to generate a pure wave mode. If the monitored structure supports guided waves, such as a plate or a rod, guided wave modes are preferred to obtain a clear response from damage via a single mode. However, if the structure is irregular or the material is strongly scattering, guided waves either do not exist or are difficult to interpret. For these situations, diffuse ultrasonic waves can be formed in the structure by an impulse excitation. The difficulty associated with diffuse waves is the complexity of the waveforms, because for diffuse waves, as many modes as the structure can support can exist during the propagation. For traditional NDT, one method that involves diffuse ultrasonic waves is the Acousto-Ultrasonic (AU) method. For SHM, using diffuse waves is a relatively new topic.

2.2.1 The Background of Diffuse Ultrasonic Waves

As previously stated, a diffuse ultrasonic field is one in which wave modes of all propagation directions and frequencies are excited with random amplitudes that are

independent of each other and random phases that are uniformly distributed [10]. A diffuse ultrasonic field can result from elastic wave propagation in strongly scattering media such as fluids with random solid inclusions and heterogeneous solids [45, 46]; or, it can be formed in a solid specimen by multiple boundary reflections [47]. The theory of diffuse ultrasonic waves in solid media was developed in the early 1980s by Egle [10] and Weaver [48]. Theoretical and experimental studies on diffuse waves formed from boundary reflections were conducted by Weaver in the same time period [49, 47].

The propagation of diffuse ultrasonic waves is typically described using the diffusion approximation, where the phase information is ignored; the energy density E is treated as a particle undergoing a random walk and is approximated by the diffusion equation [46, 50, 51],

$$\frac{E(\boldsymbol{r},t)}{\partial t} = P(\boldsymbol{r},t) + D\nabla^2 E(\boldsymbol{r},t) - \sigma E(\boldsymbol{r},t) \tag{1}$$

where P is the initial energy deposition rate, D is the ultrasonic diffusivity, and σ is the dissipation. In practice, the energy source P can be approximated by an impulse excitation at the coordinate origin [46]; $P = E_0\delta(\boldsymbol{r})\delta(t)$. The diffusion approximation has been used successfully to describe diffuse ultrasonic wave propagation in random media including samples consisting of glass beads immersed in water [50], glass bead slurry [46], aluminum foam [52], aluminum plates [47], and concrete [53, 54, 55].

Until recently, phase information has been neglected in the study of diffuse ultrasonic waves, by assuming all phase information is lost during the scattering process (i.e., becomes completely random). However, this thinking has changed somewhat by the research of Weaver and Lobkis [11], in which the authors show that complex waveforms recorded from a diffuse wave field undergo almost a pure dilation when subjected to a temperature change. Lobkis and Weaver have also shown that the long time cross correlation of two signals recorded from separate locations from a diffuse

wave field can be used to recover the Green's function of the specimen [56]. Michaels and Michaels have demonstrated that by using the short time cross correlation of two diffuse ultrasonic signals recorded from the same transmitter and receiver, before and after damage, the structural change in a simple aluminum specimen can be tracked [57]. Short time cross correlation is a measure of the local coherence of two signals, thus the results in [57] suggests the potential usefulness of phase information of diffuse ultrasonic waves.

2.2.2 Diffuse Ultrasonic Waves for Nondestructive Testing

In parallel with the theoretical study of diffuse ultrasonic waves, the use of diffuse ultrasonic waves for NDT has been investigated. One application is developed as the Acousto-Ultrasonic (AU) method.

The AU method was given to its name because it combines some aspects of the passive Acoustic Emission (AE) method and the active ultrasonic techniques. For AE, high-sensitivity ultrasonic sensors are mounted on the surface of a structure to passively record the elastic waves generated by internal damage mechanisms such as opening cracks. To improve AE analysis methods, Egle *et al.* [58, 59] investigated the simulation of emission stress waves using various excitation methods. Based on this idea of stress wave excitation, Vary [60] proposed the concept of the AU method, in which a complex diffuse-like wave field is generated by a broadband excitation at one position on a surface of the structure, and the response of the excitation is received at another position on the same surface. A comprehensive review and the theoretical basis of the AU method can be found in [61] and [62], respectively.

The AU method was originally conceived to test the strength of composite structures such as lamina and fiber-matrix interfaces. The objective is to rate the relative efficiency of stress wave propagation in such materials; a better energy transfer as assessed by a lower attenuation usually means better structural integrity [61]. Another

application of AU is to deal with distributed damage where individual identification of flaws is impractical and unnecessary. The objective for this application is to evaluate the overall structural strength using the collective information deduced concerning distributed damage [61].

For both of these applications, it is preferred that the received signal be the result of multiple interactions with the material microstructure and possible damage; i.e., an essentially diffuse ultrasonic wave is desired. However, reverberating bulk and guided waves are formed as part of an AU test. Therefore, the selection of the center frequency of the broadband excitation is important as well as the bandwidth and sensitivity of the receiving transducer [61, 63].

Received AU signals are typically analyzed by calculating parameters called stress wave factors. Stress wave factor (SWF) is the general name for a feature extracted from the received AU stress wave signal and can be defined in both the time and frequency domains. Typical SWFs include ultrasonic decay rate, centroid, and higher moments of the power spectrum. In addition, mean time skewing factor, peak voltage, and ring-down count, are all considered for SWFs [61].

The AU method has been used to evaluate various materials and structures. In [64], adhesively bonded carbon-fiber reinforced plastic-aluminum joints are evaluated using the AU method. In [65], corrosion between riveted plates is detected using the AU method. In [66], the AU method is used to characterize the carbon fiber reinforced silicon carbide composite under loadings. In [67], the AU method is applied for the characterization of composite laminated plates.

There are several limitations of the AU method. First, the AU method was developed to evaluate the overall strength of a structure. It is not capable of recognizing discrete detects or subtle material anomalies[61]. Second, the AU signal is affected by the condition of transducer-specimen coupling including the type and amount of couplant, applied pressure, and the type and position of the transducers [61]. The

effects of the transducer-specimen coupling on calculated SWFs have been considered to evaluate the efficacy of the AU method [68, 69]. One implication of this limitation is that AU signals are not repeatable from test to test, making it difficult if not impossible to track structural changes over time using the AU method.

2.2.3 Diffuse Ultrasonic Waves for Structural Health Monitoring

The scenario of SHM using diffuse ultrasonic waves is similar to the AU NDT method, where transmit and receive transducers are typically mounted on the same side of the specimen, and diffuse (or diffuse-like) ultrasonic waves are excited to interrogate a large volume of the structure. However, they differ in two aspects: (1) In SHM, transducers are permanently mounted on the structure for *in situ* monitoring, while the transducers are temporarily coupled to the structure surface for the AU method; (2) For SHM, the goal is to detect and quantify structural damage, while for the AU method, the purpose is to obtain an overall estimate of structural strength. The permanently mounted transducers in SHM offer a significant advantage over the AU method because they avoid the lack of reproducibility of measurements resulting from variations in transducers and coupling conditions.

Recently, using permanently attached transducers has been considered for the AU NDT method to obtain repeatable measurements [70, 71]. However, development of new signal processing methods for diffuse ultrasonic waves for SHM is still an important issue for the purpose of damage detection and characterization instead of an overall strength evaluation.

As a relatively new research area, not much work on the signal processing of diffuse ultrasonic waves for SHM has been done. As described in Sec. 2.2.1, diffuse ultrasonic wave energy propagation is well approximated by the diffusion equation [52, 50], thus estimated diffusive and dissipation coefficients of the diffusion equation can be correlated to the material and structural changes for SHM. The application of this idea

was implemented by Becker [54] and Punurai [55] for concrete specimens. Michaels and Michaels [57] compared three methods for analyzing diffuse ultrasonic signals, namely, time domain differencing, spectrogram differencing, and the local temporal coherence. These methods are based on the comparison of a monitored signal to a non-flaw baseline signal that is known *a priori*. Biemans [72] considered various feature extraction methods for diffuse ultrasonic waves in the time, frequency, and wavelet domains, where static and dynamic loads were used in the experiments. Michaels *et al.* [73] suggested using the Fisher Discriminant Ratio to select features extracted from diffuse ultrasonic waves.

2.3 Environmental Effects on Diffuse Ultrasonic Waves

Environmental variations, such as temperature and surface condition changes, can substantially affect the detection of damage for an SHM system. For vibration-based SHM, the effects of temperature have become of increasing concern in recent years [74, 75, 76, 77, 78]. For ultrasonic SHM, the effects of environmental changes have not been the subject of much research and, when considered at all, the approaches have not been systematic. The progress of research on ultrasonic SHM in general and diffuse ultrasonic waves in particular is reviewed here.

The effect of temperature variations on diffuse ultrasonic waves was investigated by Weaver and Lobkis [11, 79] and Snieder [80]. Their research results establish a theoretical basis for analyzing the effects of temperature changes using the phase information of diffuse ultrasonic signals.

To compensate the effect of temperature variations on ultrasonic SHM, Mazzeranghi implemented several case-based ultrasonic methods [81]. For these proposed methods, online temperature measurements are required and none of the methods is a generic approach for systematically and effectively addressing the problem. Rajic investigated the effects of temperature on the response of surface-mounted piezotransducers [82].

The effects of temperature changes on the transducer are measured and empirically removed, but other temperature effects are not considered.

Based on the theoretical work of Weaver, Lobkis, and Snieder [11, 79, 80], Michaels and Michaels [57] considered temperature variations in the context of using the local temporal coherence for damage detection. Lu and Michaels [83] performed a study on the effect of temperature on diffuse ultrasonic signals in the context of SHM, and their results are reported in this thesis.

Recently, Betz *et al.* [84] proposed the idea of temperature-damage cross sensitivity where features that are sensitive to damage but insensitive to temperature changes are selected for decision making. In [85], additional transducers are added near the monitoring transducers. By assuming that the possible location of damage is known and is not located near the monitoring transducer, the effect of temperature can be compensated using the the signals from the additional transducers as a temperature reference for the monitoring one. Konstantinidis *et al.* suggested the use of a group of baselines recorded from early operating cycles to compensate for temperature effects [86, 87]; their methodology is similar to that developed in [83].

For the effects of environmental variations other than temperature changes, Takatsubo et al. [88] discuss the effects of surface wetting and load on tone burst ultrasonic waves using ultrasonic spectroscopy. For diffuse ultrasonic waves, there is no published research work on the effects of surface condition changes until now.

2.4 Research Context

From the literature review on ultrasonic SHM, one can see that SHM using diffuse ultrasonic waves is not a mature and accepted technology and there has been only some preliminary progress regarding their use. Therefore, it is necessary to provide a foundation for using diffuse ultrasonic waves for SHM. Since diffuse ultrasonic waves can easily be generated by an impulse excitation, existing and emerging transducer

technologies, such as PZT transducers, PWAS, and film sensor layers, are all suitable for wave generation; similarly, these same transducers, along with fibre optic based sensors can be used for signal reception. The major difficulties and challenges thus exist in the signal processing of diffuse ultrasonic signals for the purpose of damage detection and evaluation.

The first task of signal processing is to extract efficient features that can be correlated to the change of structural status. In this research, several feature extraction techniques used for guided ultrasonic waves and the AU method are utilized, such as mean squared error, loss of coherence, correlation coefficient, etc. In addition, new features are proposed and implemented according to the properties of diffuse ultrasonic waves. These new features are based on two methodologies, matching pursuit decomposition and embedding of chaotic signals, which are proposed for diffuse ultrasonic signal analysis for the first time.

The second task of signal processing is to analyze and model the effects of benign environmental changes, including temperature and surface condition changes. In this thesis, experiments are designed to investigate these environmental effects. The temperature effect is successfully compensated using a theoretical model. The effect of surface condition changes is addressed based on feature extraction and data fusion methods, where two surface conditions, wetting and contact, are considered.

Based on the feature extraction methods, a decision making strategy consisting of a threshold selection method followed by feature and sensor fusion is proposed and implemented in this thesis. The integration of all these methodologies provides a comprehensive damage detection strategy for SHM using diffuse ultrasonic waves.

CHAPTER III

EXPERIMENTS

Three experiments were performed on aluminum structures. The first two experiments were designed to study the effect of temperature on diffuse ultrasonic waves as well as to support the development of feature extraction methods for damage detection. Some surface condition changes were introduced during the experiments to test the selectivity of features. The third experiment was designed to systematically investigate surface condition changes. Features that are sensitive to damage but insensitive to given surface condition changes are developed based on the experimental data.

3.1 Notch Experiment (#1)

For this experiment, the specimen was a 6061 aluminum plate, 50.8 mm × 152.4 mm × 6.35 mm (2 in. × 6 in. × 0.25 in.). This specimen geometry was chosen to be typical of a machined component fabricated from a constant thickness plate. If the plate were infinite, propagating Lamb waves would form [22] and radiate out from the transmitter, and a diffuse field would not exist. Since the plate is finite in extent, with the shortest distance from the source transducer to a boundary being only four times the thickness, reflections occur before guided waves are fully formed. Received signals are observed to be diffuse-like in that individual reflections are not distinguishable; nor can specific longitudinal, shear or guided wave mode arrivals be identified. Even though the wave field is probably not truly diffuse, it is complex and typical of what might be expected for a real structural component.

The specimen for the first experiment is shown in Fig. 5. Two epoxy-backed piezoelectric transducers were attached to the top surface of the specimen using cyanoacrylate adhesive, and the specimen was supported by three small rubber spacers to minimize the effects of the support structure on the waveforms. The transducers were constructed of 12.5 mm diameter, longitudinally polarized, 2.25 MHz broadband PZT disks backed with epoxy for mechanical protection. A conventional ultrasonic pulser receiver (Panametrics 5072PR) was used for spike mode transducer excitation and waveform reception. The ultrasound was generated by transducer #1 and the diffuse waveform was received at transducer #2.

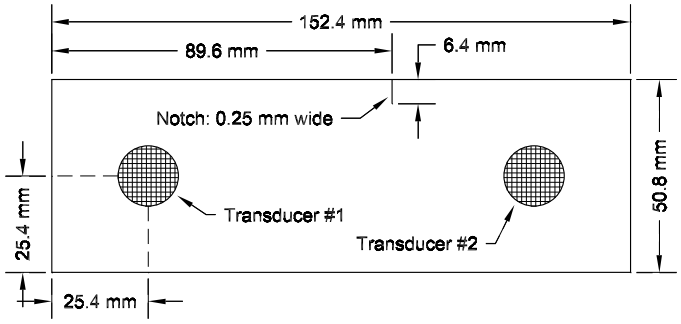

Figure 5: Specimen with notch from experiment #1.

Received signals were amplified and low pass filtered with a cutoff frequency of 10 MHz. Waveforms were digitized using a PC digitizer with a sampling rate of 25 MHz and a resolution of eight bits. Each recorded waveform was the average of 50 signals to minimize electronic noise. The waveforms were recorded for 2000 μs after transmit for a total of 50,000 data points per waveform. Figure 6 shows a typical recorded diffuse ultrasonic wave and its spectrum.

The experiment consisted of two stages: (1) before and (2) after the introduction of artificial damage. In the first stage, the undamaged specimen was subjected to temperature changes ranging from 5 °C to 40 °C. Waveforms were recorded at every integer degree (°C), and this procedure was repeated to obtain two sets of waveforms

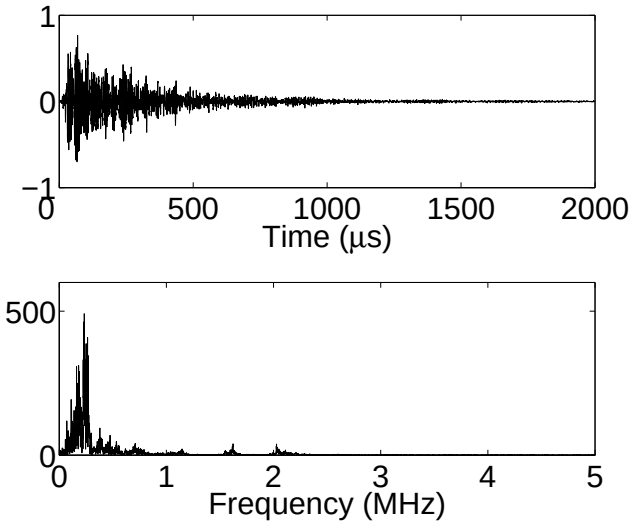

Figure 6: A typical diffuse ultrasonic wave and its spectrum

at each temperature. Multiple waveforms were also recorded at temperatures of approximately 18 °C, 25 °C, and 33 °C, representing low, room, and high temperatures, respectively. All these waveform are used for studying the effect of temperature.

In addition, at the low, room, and high temperatures, various surface condition changes were introduced. These changes include:

- Placing a small oil-coupled aluminum block on the surface.
- Placing a oil-coupled steel ruler on the surface.
- Putting oil droplets on the surface.
- Partially immersing the specimen in water
- Introducing varying amounts of water on the surface

Figure 7 shows the locations of the aluminum block and the steel ruler. The aluminum block was placed in various areas with two different orientations. As shown by the colored regions of Fig. 7, one position is to put the block on its green surface, and the four corresponding locations are labeled as 1, 2, 3, and 4 on the specimen. The other

position is to put the block on its cyan surface, and the two corresponding locations are area 123 and area 234. The steel ruler was placed in two different areas as shown in the figure. These cases were used to simulate variable surface contact conditions.

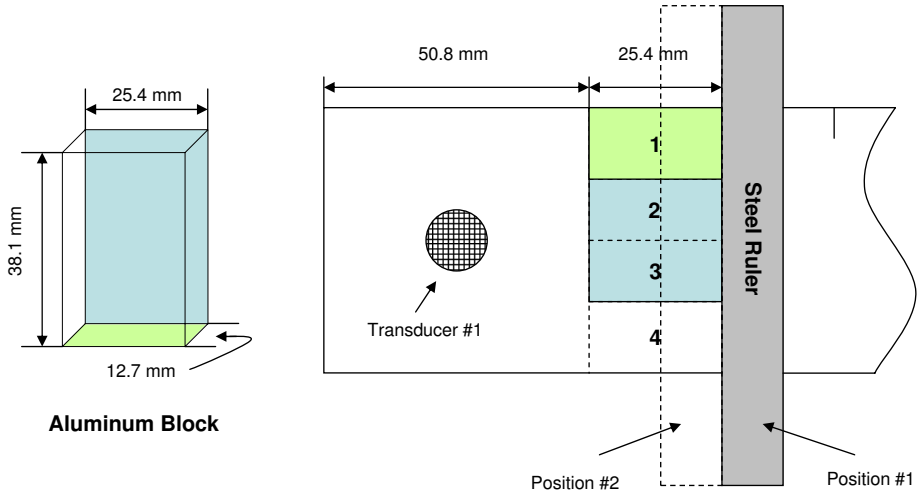

Figure 7: Surface contact conditions for experiment #1.

Figure 8 illustrates the surface wetting conditions which were achieved by adding oil droplets and water to the specimen surface as indicated by the drawing of Fig. 8(a). Two extreme conditions were simulated by partially immersing the specimen in water, as illustrated in the drawing of Fig. 8(b).

In the second stage of this experiment, an artificial flaw was introduced by cutting a through thickness notch of width 0.25 mm (0.01 in.) in the specimen to simulate a crack, as shown at its final length in Fig. 5. The starting notch length was 0.64 mm (0.025 in.) and it was increased in increments of 0.64 mm (0.025 in.) to a final length of 6.35 mm (0.25 in.) for a total of 10 steps. At each step, the specimen was subjected to temperatures ranging from 5 °C to 40 °C, as was done in the first stage for the undamaged specimen. Waveforms were recorded at every integer degree and also at low, room, and high temperatures, as described previously. At every

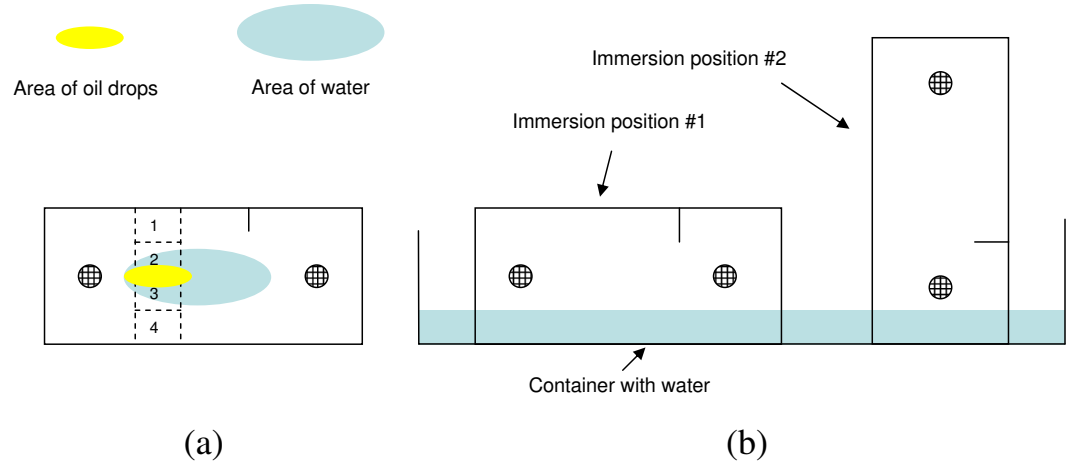

Figure 8: Surface wetting conditions for experiment #1.

other notch length increment, surface condition changes the same as those applied in the first stage were also introduced at low, room, and high temperatures. All the measurements from the experiment are summarized in Table 1.

Table 1: Summary of measurements for experiment #1 before and after introduction of a through-thickness edge notch.

Waveform Description	Number of Waveforms	Temperature Range (°C)	Notch Length (mm)
Baselines	36	5.0 : 1.0 : 40.0	N/A
No Damage or Surface Condition Change	36	5.0 : 1.0 : 40.0	N/A
No Damage or Surface Condition Change	29	17.6 – 34.3	N/A
Surface Condition Change Only	50	17.6 – 34.3	N/A
Damage Only	397	5.0 : 1.0 : 40.0	0.64 : 0.64 : 6.35
Damage and Surface Condition Change	105	14.5 – 34.8	0.64 : 1.28 : 5.71

3.2 Hole Experiment (#2)

In the second experiment, the specimen geometry and the experimental setup were the same as for the first, except that the sampling frequency in the second experiment was reduced to 12.5 MHz and each waveform was recorded for 1000 μs for a total of

12,500 data points. The sampling frequency of 12.5 MHz was high enough to prevent aliasing given that there was insignificant energy above 5 MHz.

For this experiment, a different type of flaw in a different location was introduced by drilling a hole. The initial size of the hole was 1.98 mm (5/64 in.) in diameter and it was subsequently enlarged in 10 steps to a final diameter of 6.35 mm (1/4 in.), as shown in Fig. 9. Similar to the first experiment, before and after the introduction of the flaw, waveforms were recorded at different temperatures with and without surface condition changes. The types of surface condition changes applied in this experiment were:

- Placing a small oil-coupled aluminum block on the surface.
- Introducing varying amounts of uncontrolled water on the surface.

Figure 10 illustrates these two types of surface condition changes, where the size of the small aluminum block is the same as for the first experiment. Table 2 summarizes the measurements.

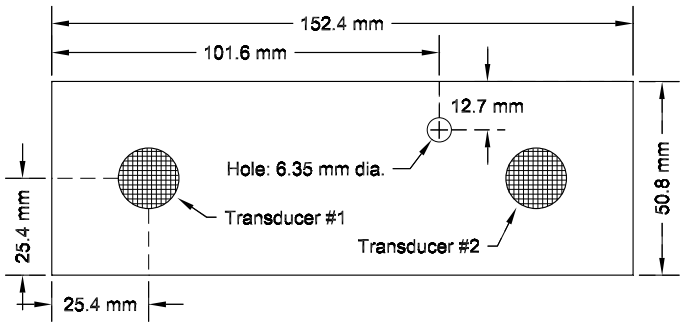

Figure 9: Specimen with hole from experiment #2.

In both experiments #1 and #2, a heating pad and an ice pack were used to vary the temperature. The specimens were contained in a partially insulated enclosure to minimize temperature instability and gradients during each measurement. Temperatures were measured using a multi-meter (Fluke 16) with an integral temperature

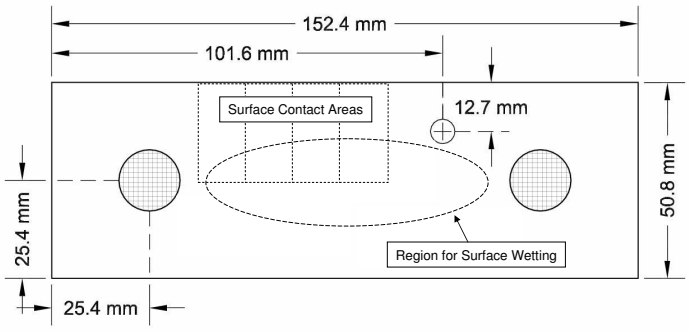

Figure 10: Surface condition changes for experiment #2.

Table 2: Summary of measurements for experiment #2 before and after introduction of a through-hole.

Waveform Description	Number of Waveforms	Temperature Range (°C)	Hole Diameter (mm)
Baselines	27	8.9 : 1.1 : 37.8	N/A
No Damage or Surface Condition Change	98	10.0 – 32.2	N/A
Surface Condition Change	44	23.6 – 32.2	N/A
Damage Only	40	10.0 – 25.6	1.98 – 6.35
Damage and Surface Condition Change	10	23.8 – 23.9	3.97 and 6.35

probe (Fluke 80BK). The instrumentation accuracy of the combined probe and meter is estimated to be ±1 °C, and the measurement resolution is 0.1 °C.

3.3 Surface Condition Experiment (#3)

In the third experiment, the specimen was an aluminum plate with a center through thickness hole. The size of the plate was 152.4 mm × 152.4 mm × 6.35 mm (6 in. × 6 in. × 0.25 in.), and the diameter of the through thickness hole was 2.54 mm (1 in.). The flaw in this experiment was simulated by a through thickness hole whose diameter was enlarged in steps. The initial diameter was 1 mm, it was enlarged with a step size of 0.5 mm, and the final diameter was 6 mm after 11 steps. Fig. 11 shows a drawing of the specimen.

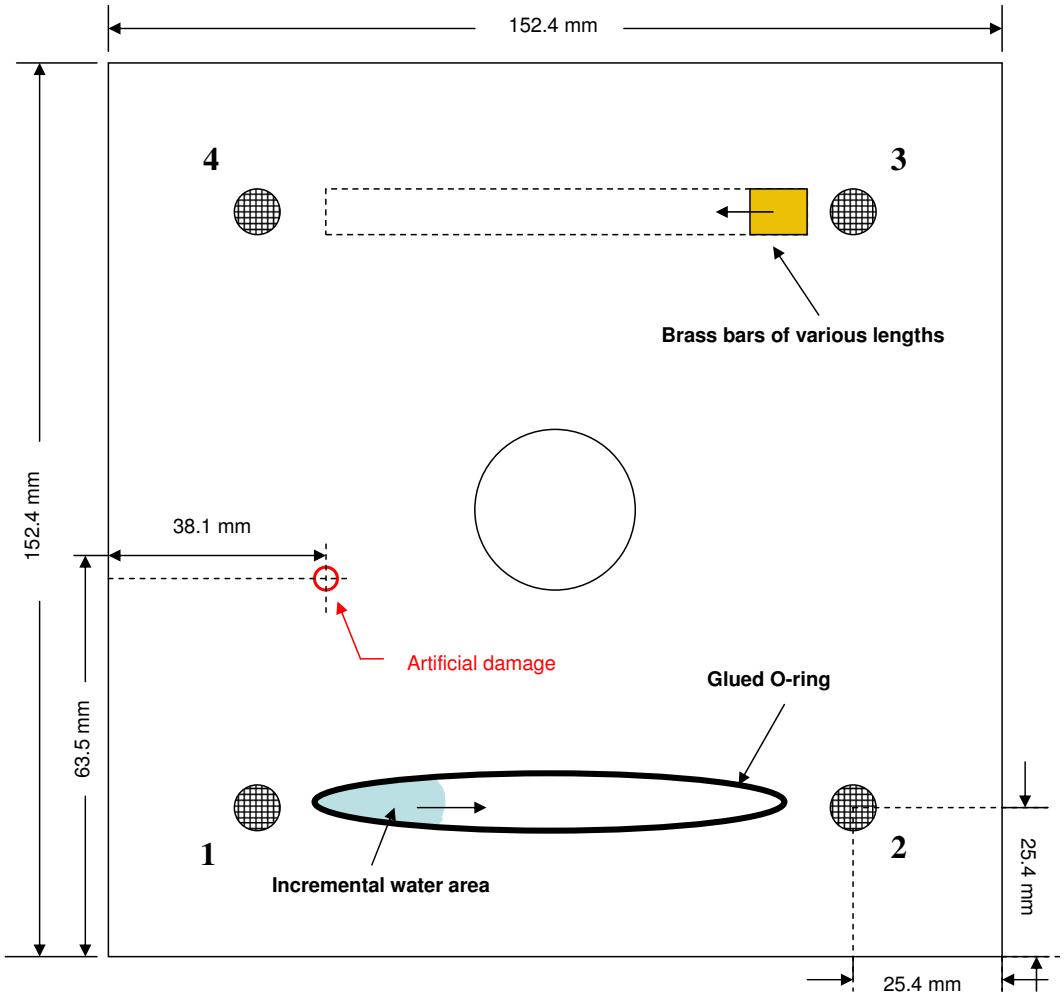

Figure 11: Experiment #3.

In the undamaged condition and for each step of damage, well controlled incremental surface condition changes were applied to the specimen; the changes were surface wetting and contact. The wetting condition was controlled by adding water into an area constrained by an O-ring glued between transducers #1 and #2, as shown in Fig. 11. A syringe was used to add water to the leftmost part of the O-ring with 10 drops (approx. 0.12 ml) added per step. The specimen was tilted with the right side slightly higher than the left side. Therefore, with each step of adding water, the water area on the surface increased towards the right end of the O-ring; the whole

area of the O-ring was covered with water after 13 steps (approx. 1.56 ml). Three more steps were added to increase the thickness of the water layer, resulting in a total of 16 steps (approx. 1.92 ml).

Surface contact conditions were simulated by brass bars of various lengths coupled to the surface by oil. The cross section of the brass bars is 6.35 mm $\times$ 6.35 mm (0.25 in. $\times$ 0.25 in.), and the lengths of the bars varied from 6.35 mm (0.25 in.) to 76.2 mm (3.0 in.) in a step size of 6.35 mm (0.25 in.). As illustrated in Fig. 11, brass bars were oil coupled to the surface one piece a time, from the shortest to the longest. With the same alignment point close to transducer #3, this successive procedure could be viewed as a bar with growing length, resulting in a controlled incremental surface contact change.

For each structural status and surface condition, all six through-transmission diffuse ultrasonic signals were recorded at 12.5 MHz for 1000 μs (12500 points). These six signals correspond to six transducer pairs (pair 1-2, pair 1-3, pair 1-4, pair 2-3, pair 2-4, and pair 3-4), where for each pair, the first transducer was excited by an impulsive excitation and the second transducer received the signal. As for the previous two experiments, each signal is the average of 50 waveforms. Measured data are summarized in Tables 3 and 4, where each set contains six signals from the six transducer pairs.

Table 3: Summary of measurements for experiment #3, surface wetting (204 sets of signals)

Surface Condition		**Structural Status: Hole Diameter (mm)**				
Step	Description	0	1.0	1.5	...	6.0
0	No water	set 0,0	set 0,1	set 0,2	...	set 0,11
1	10 drops (not filled)	set 1,0	set 1,1	set 1,2	...	set 1,11
2	20 drops (not filled)	set 2,0	set 2,1	set 2,2	...	set 2,11
...		...				
13	130 drops (filled)	set 13,0	set 13,1	set 13,2	...	set 13,11
14	140 drops (over filled)	set 14,0	set 14,1	set 14,2	...	set 14,11
15	150 drops (over filled)	set 15,0	set 15,1	set 15,2	...	set 15,11
16	160 drops (over filled)	set 16,0	set 16,1	set 16,2	...	set 16,11

Table 4: Summary of measurements for experiment #3, brass bar contact (182 sets of signals)

Surface Condition		**Structural Status: Hole Diameter (mm)**						
Step	Length (mm)	0	0	0	1.0	1.5	...	6.0
0	0	set 0,0	set 0,1	set 0,2	set 0,3	set 0,4	...	set 0,13
1	6.35	set 1,0	set 1,1	set 1,2	set 1,3	set 1,4	...	set 1,13
2	12.7	set 2,0	set 2,1	set 2,2	set 2,3	set 2,4	...	set 2,13
...		...						
12	76.2	set 12,0	set 12,1	set 12,2	set 12,3	set 12,4	...	set 12,13

CHAPTER IV

THEORY

In this chapter, three aspects of the theory and mathematical background used for the methodology of SHM with diffuse ultrasonic waves are introduced. The first is the effect of temperature on diffuse ultrasonic waves, which is illustrated with experimental examples. The second is the method of matching pursuit signal decomposition, including a numerical implementation designed for ultrasonic waves, and distributed and constrained decompositions for diffuse ultrasonic waves. The third is the theory of embedding and chaotic signals.

4.1 Effect of Temperature on Diffuse Ultrasonic Waves

The influence of environmental changes on SHM with diffuse ultrasonic signals has not been the subject of much research, as was summarized in Sec. 2.3. Among various environmental conditions, temperature changes are of particular interest because temperature is an unavoidable global environmental condition and its variations substantially alter the recorded waveforms. This section introduces the theoretical basis for temperature effects, which is used later in the proposed temperature compensation method described in Sec. 5.1. The material presented here was previously published in [83] and is summarized here.

The effects of temperature changes on diffuse ultrasonic waves are considered in [11, 79, 80]; it is shown that the primary effect of a temperature change is to stretch or compress the signal, and a secondary effect is to distort the shape. In [11], the authors show that, as the specimen cools or heats, the diffuse wave is compressed or stretched, respectively. Furthermore, the shape of the waveform is increasingly distorted as the temperature change and the time-of-flight increase. Figure 12 illustrates the waveform

stretching using data from the first experiment. Figures 12(a) and 12(b) show two waveforms recorded from the undamaged specimen at 25 °C and 35 °C, respectively. Figure 12(c) shows sections of these two waveforms from a 50 μs window centered at 45 μs, and Fig. 12(d) shows similarly windowed sections centered at 445 μs. Note that the waveform at 35 °C is shifted to the right compared to the one at 25 °C, and the time shift is greater in the later time window (Fig.12(d)) than in the earlier time window (Fig.12(c)); these plots illustrate the time-dependent time shift caused by the temperature difference.

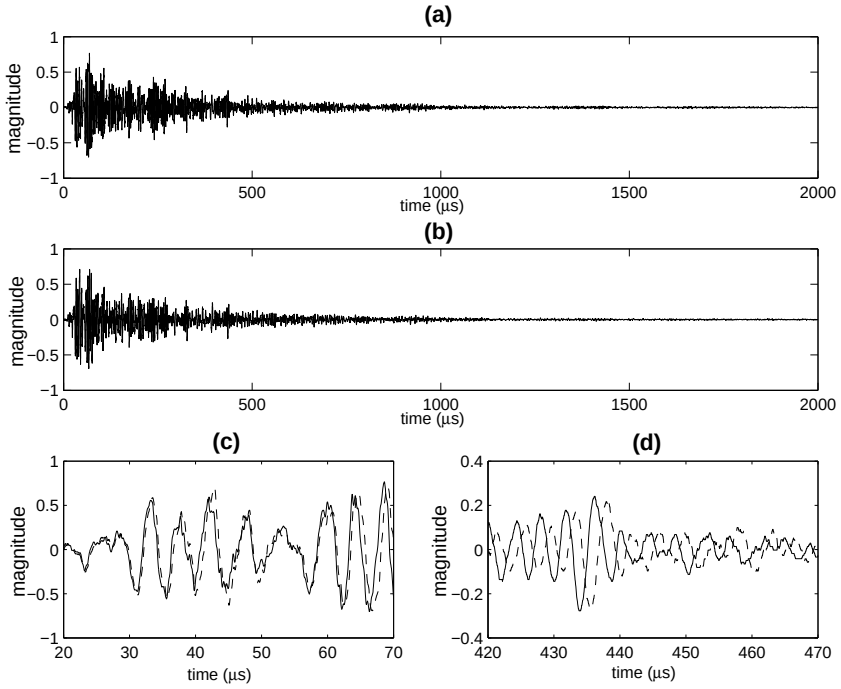

Figure 12: Illustration of the temperature dependence of diffuse ultrasonic waveforms from experiment #1. (a) Waveform from the specimen at 25 °C, (b) waveform from the specimen at 35 °C, (c) time window centered at 45 μs, and (d) time window centered at 445 μs. Solid lines correspond to 25 °C and dashed lines to 35 °C

Similar to the methods used in [11] and [57], a linear phase shift (i.e., time shift) can be characterized using the short time cross correlation,

$$\hat{R}_{xy}(\tau, t_c) = \begin{cases} \int_{t_c-\frac{T}{2}+\tau}^{t_c+\frac{T}{2}} x(t) \cdot y(t-\tau)dt; & \tau > 0 \\ \int_{t_c-\frac{T}{2}}^{t_c+\frac{T}{2}+\tau} x(t) \cdot y(t-\tau)dt; & \tau < 0 \end{cases} \tag{2}$$

where $x(t)$ and $y(t)$ are waveforms, t_c is the time window center, T is the time window length, and τ is the cross correlation lag. Following [57], the estimated time delay $\hat{D}_{xy}(t_c)$ is calculated as the lag of the peak of $\hat{R}_{xy}(\tau, t_c)$ as a function of t_c:

$$\hat{D}_{xy}(t_c) = \arg\max_{\tau}\{|\hat{R}_{xy}(\tau, t_c)|\}. \tag{3}$$

This time delay is linear with respect to the center of the time window t_c for a perfect dilation or compression of $y(t)$ relative to $x(t)$, and is positive in sign for a dilation.

Figure 13 shows the result of the short time cross correlation of the 25 °C and 35 °C waveforms of Fig. 12 as a plot of time delay versus the center of the time window. For this and subsequent plots, the time window was 200 μs, the time increment was 50 μs, and the range of lags considered was limited to $\pm$ 35 μs. Consistent with the results in [11], the time delay increases linearly with the center of the time window, which describes the dependence of the diffuse wave phase on temperature. There is a small offset as well as small systematic variations, probably due to the wave field not being completely diffuse. A consequence of this stretching is that a segment of the waveform at a later time is shifted more than a segment at an earlier time, as is seen in Fig. 12. This stretching (or compressing) can be expressed as

$$y(t) = x(t - \xi t), \tag{4}$$

where $x(t)$ and $y(t)$ are diffuse waveforms at two temperatures and ξ is the slope of the straight line that fits the local time delays to the centers of the time window. Since an increase in temperature results in a time delay (i.e., a later arrival), the minus sign is used so that ξ is positive as temperature increases.

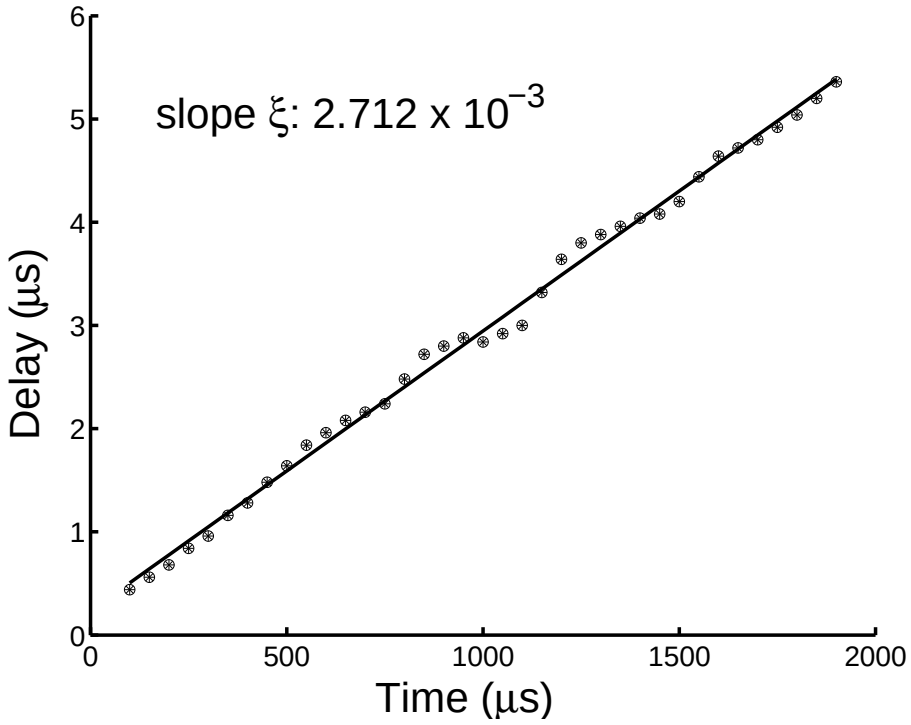

Figure 13: Time delay curve calculated from the short time cross correlation of waveforms from experiment #1 at 25 °C and 35 °C.

Theoretically, two effects contribute to the temperature dependence of the diffuse wave phase. One is the thermal expansion of the structure, and the other is the temperature dependence of both the longitudinal and transverse wave velocities. The temperature change results in a change in the length of the waveform path because of thermal expansion. If the original path length of an ultrasonic wave at temperature T_0 is $P(T_0)$, then the path $P(T)$ after the temperature change is

$$P(T) = [1 + \alpha(T - T_0)]P(T_0) \tag{5}$$

where α is the coefficient of thermal expansion ($2.43 \times 10^{-5}/\,^{\circ}\mathrm{C}$ for 6061 aluminum [89]).

The velocities of the longitudinal and shear waves also change as temperature changes. The velocities of these two wave modes at a given temperature can be calculated by using the coefficients of velocity change:

$$c_l(T) = c_l(T_0) + \kappa_l(T - T_0) \tag{6}$$

$$c_s(T) = c_s(T_0) + \kappa_s(T - T_0) \tag{7}$$

where c_l and c_s are the longitudinal and shear wave velocities, T_0 is a reference temperature, and κ_l and κ_s are the coefficients of longitudinal and shear velocity change with respect to temperature T. For the 6061 aluminum used in the experiments, c_l and c_s are $6270m/s$ and $3080m/s$ (assumed to be at 25 °C) [7]. Values of $-1.089m/s/\,^{\circ}\mathrm{C}$ and $-0.752m/s/\,^{\circ}\mathrm{C}$ are used for κ_l and κ_s. These values are estimates and were obtained by averaging published measurements for 6063 aluminum [90].

The total path of a diffuse wave can be thought of as being comprised of a longitudinal portion and a shear portion [91]:

$$P = P_l + P_s. \tag{8}$$

Consequently, the arrival time at a given temperature T can be expressed as

$$t(T) = t_l(T) + t_s(T) = \frac{P_l(T)}{c_l(T)} + \frac{P_s(T)}{c_s(T)}, \tag{9}$$

where $t_l(T)$ and $t_s(T)$ denote the longitudinal and shear contributions in time.

For an arrival time $t(T)$ at a given temperature T, the time difference with respect to the arrival time at a reference temperature T_0 is

$$\Delta t(T) = t(T) - t(T_0) = \left[\frac{P_l(T)}{c_l(T)} + \frac{P_s(T)}{c_s(T)}\right] - \left[\frac{P_l(T_0)}{c_l(T_0)} + \frac{P_s(T_0)}{c_s(T_0)}\right]. \tag{10}$$

Differentiating Eq. 10 with respect to temperature T, we obtain after some algebra

$$\frac{d}{dT}[\Delta t(T)] = t(T)\left\{\alpha - \frac{t_l(T)}{t(T)}\,\frac{d}{dT} ln[c_l(T)] - \frac{t_s(T)}{t(T)}\,\frac{d}{dT} ln[c_s(T)]\right\}. \tag{11}$$

For diffuse waves in metals, Weaver [48] shows that the ratio R of shear energy to longitudinal energy is a fixed value that is a function of only Poisson's ratio ν (0.33 for 6061 aluminum [89]):

$$R = 2\Big(\frac{2-2\nu}{1-2\nu}\Big)^{3/2}. \tag{12}$$

Thus, the fraction of shear energy is

$$f_s = \frac{R}{1+R} \tag{13}$$

and the fraction of longitudinal energy is

$$f_l = \frac{1}{1+R}. \tag{14}$$

If we assume that the fractions of shear and longitudinal energy are equal to the time fractions, Eq. 11 can be written as

$$\frac{d}{dT}[\Delta t(T)] = t(T)\big[\alpha - f_l\ \frac{d}{dT} ln[c_l(T)] - f_s\ \frac{d}{dT} ln[c_s(T)]\big]. \tag{15}$$

This equation, which is in agreement with that given in [11], can be simplified using Equations 6 and 7:

$$\frac{d}{dT}[\Delta t(T)] = t(T)\big[\alpha - f_l\ \frac{k_l}{c_l(T)} - f_s\ \frac{k_s}{c_s(T)}\big]. \tag{16}$$

In the neighborhood of a reference temperature T_0, the change in time can be approximated as

$$\Delta t(T) \approx t(T)\big[\alpha - f_l\frac{\kappa_l}{c_l(T_0)} - f_s\frac{\kappa_s}{c_s(T_0)}\big](T - T_0). \tag{17}$$

This approximation is very good for realistic temperature changes ($\pm 50\,^{\circ}$C). The expression for $\Delta t(T)$ can be recognized as the time delay $\hat{D}_{xy}(t)$ at a specific temperature T:

$$\hat{D}_{xy}(t) = t\big[\alpha - f_l\frac{\kappa_l}{c_l(T_0)} - f_s\frac{\kappa_s}{c_s(T_0)}\big](T - T_0) \tag{18}$$

where t is the time at temperature T; that is, it is a specific time on the ultrasonic signal measured at temperature T.

Figure 14 shows this calculated time delay for the 25 °C waveform of Fig. 12(a) for a +10 °C temperature change. The experimental curve from Fig. 13 is shown along with the contribution from thermal expansion only. The slope of the theoretical curve is in very close agreement with the experimental results; the experimental curve does have a small unexplained non-zero intercept of approximately 0.1 μs.

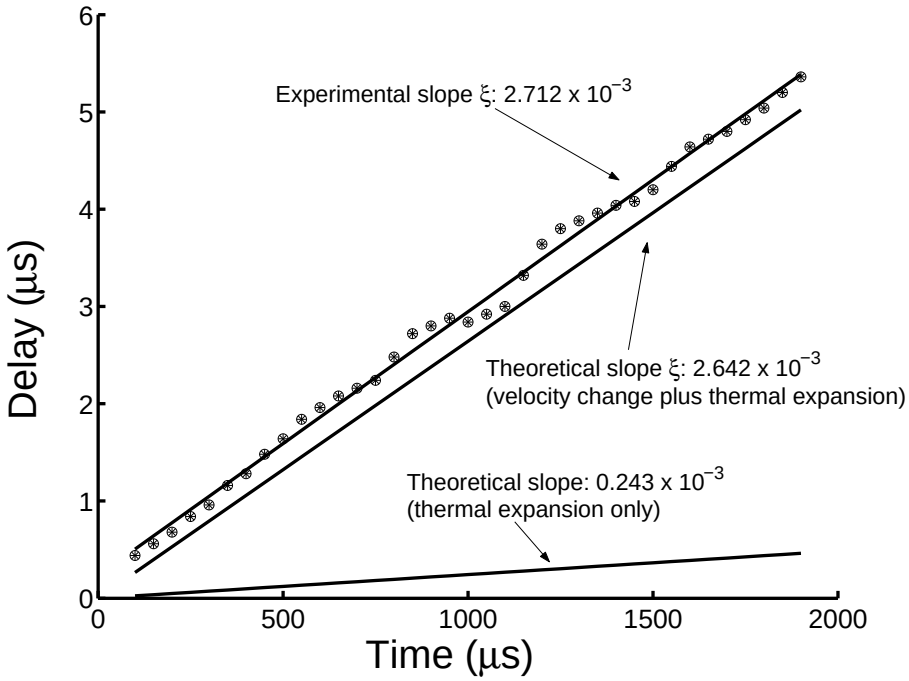

Figure 14: Experimental and theoretical time delay curves for waveforms from experiment #1 at 25 °C and 35 °C.

At a fixed temperature, slope ξ defined in Eq. 4 is simply the time delay divided by time,

$$\xi = \frac{d\hat{D}_{xy}(t)}{dt} = \big[\alpha - f_l\ \frac{\kappa_l}{c_l(T_0)} - f_s\ \frac{\kappa_s}{c_s(T_0)}\big](T - T_0). \tag{19}$$

Thus, in addition to the linearity between the time delay and the time window center for a constant temperature change, the slope ξ that represents this linearity also increases linearly as the temperature change increases. Figure 15 shows time delays obtained from the short time cross-correlation of seven pairs of waveforms recorded from the undamaged specimen in the first experiment for seven different temperature changes. Although there is some distortion in the linearity of the time delay vs. the time window center curves, especially for waveform pairs with large temperature differences (for example, 10 °C and 25 °C), the coefficient ξ is seen to be linear with temperature change. This linearity is shown explicitly in Fig. 16, where both experimental and theoretical curves of slopes ξ vs. temperature difference are plotted. This dependence of the phase, or time shift, of a diffuse ultrasonic wave on temperature is not a function of the presence or size of flaw, but only of material properties (Poisson's ratio, coefficient of thermal expansion, ultrasonic wave velocities, and temperature dependence of the wave velocities).

4.2 Matching Pursuit Signal Decomposition

In this section, the general idea of matching pursuit signal decomposition is introduced. Then, a numerical implementation designed for ultrasonic signals is proposed and implemented. Finally, the methods of distributed and constrained matching pursuit decomposition are introduced; these methods are used to extract feature from changes in diffuse ultrasonic signals, as is described in Sec. 5.2.

4.2.1 The Idea of Matching Pursuit

Matching pursuit is a signal decomposition method whereby a signal is decomposed into a linear combination of functions that are selected from a redundant (i.e., non-orthogonal) set, called a dictionary. Matching pursuit was developed independently by Mallat and Zhang [92] and Qian and Chen [93] for the purpose of signal compression and approximation, and can be viewed as a derivative of the wavelet transform

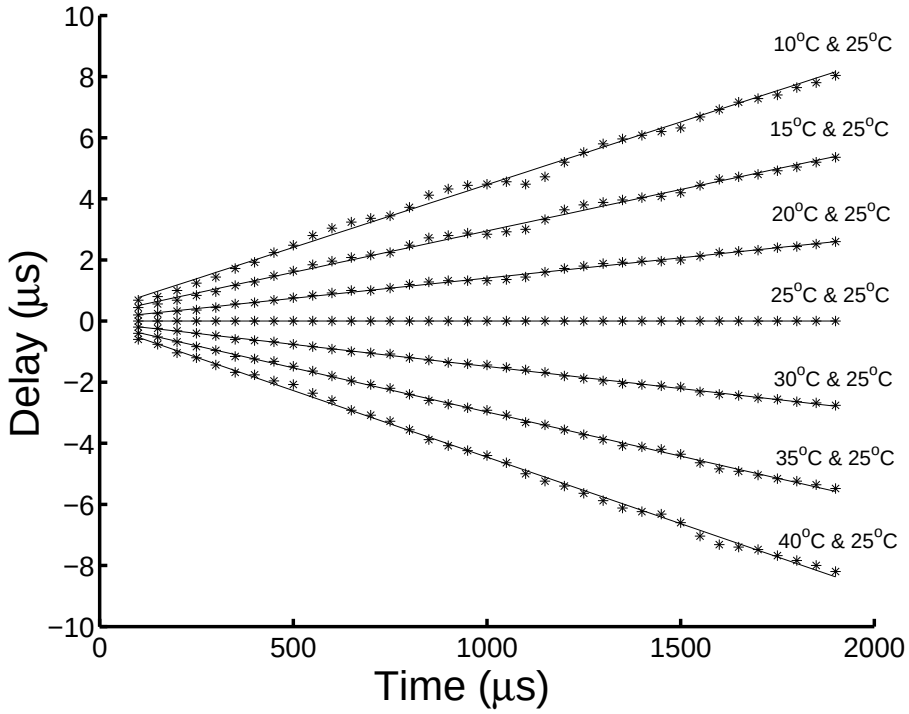

Figure 15: Time delay curves calculated from the short time cross correlation of waveforms from experiment #1 at various temperatures.

[94]. It inherits the concept of approximating signals with time localized basis functions, but differs from the wavelet decomposition in that the basis functions are not orthogonal. The purpose of using redundant basis functions is to maximize the waveform matching between the basis functions and the signal, which cannot be achieved if the basis functions are restricted by orthogonality.

As originally proposed by Mallat and Zhang [92], a family of Gabor functions was used as the basis functions. Each Gabor function $g_\gamma(t)$ is the product of a Gaussian function with a complex sinusoid, and is specified by time shift, frequency and scale,

$$g_\gamma(t) = \frac{1}{\sqrt{2\pi}s} e^{-\frac{(t-u)^2}{2s^2}} e^{i\xi t}. \tag{20}$$

In this equation, u and s are the time shift and scale, respectively, of the Gaussian envelope, and ξ is the radian frequency of the complex modulating sinusoid (not to be confused with the slope ξ of Eq. 4). All possible Gabor functions are specified by the

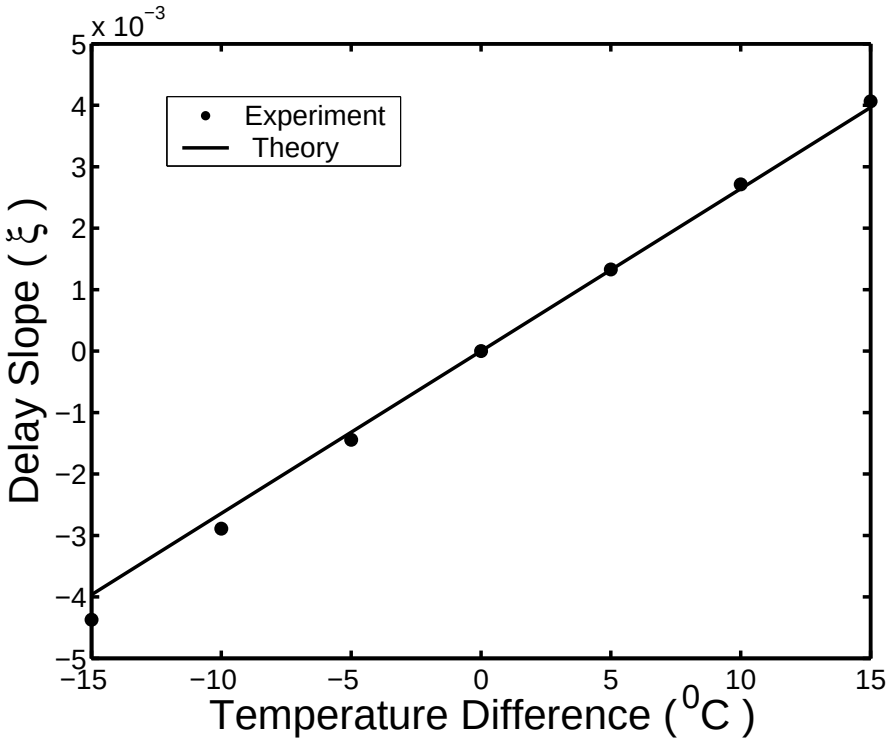

Figure 16: Temperature dependence of the slope of the time delay curve.

parameter set $\gamma = (u, s, \xi) \in R^3$. Compared to wavelet functions, u corresponds to the translation parameter and s corresponds to the dilation parameter. The parameter ξ explicitly sets the center frequency of the Gabor function and it is an extra free parameter that wavelet functions do not have. Finally, all three parameters, u, s, and ξ, can be chosen independently, yielding a redundant basis for matching pursuit.

Because these Gabor functions are qualitatively and quantitatively very similar to ultrasonic echoes, matching pursuit with Gabor functions has been frequently used to identify and estimate echoes present in ultrasonic signals for a wide range of NDT&E and SHM applications. Hong et al. [95] use matching pursuit with Gabor functions in guided wave damage inspection. Raghavan and Cesnik [96] use a dictionary of modified Gabor functions to separate overlapping guided wave modes. Ruiz-Reyes *et al.* [97] apply matching pursuit to enhance echoes in scattered ultrasonic waves. Lu and Michaels [98] show the capability and efficacy of matching pursuit in

identifying both discrete and overlapping echoes from reverberating ultrasonic signals. In addition to complex Gabor functions, frequency modulated real Gaussian functions [99, 100, 101], redundant Morlet wavelets [102], and chirplet functions [103, 104] are also used as basis functions in applications of ultrasonic echo estimation. In this thesis only Gabor functions are used as basis functions.

To decompose a signal via matching pursuit with Gabor functions, the match between a Gabor basis function and a signal is first defined by the inner product,

$$< f, g_\gamma >= \int_{-\infty}^{+\infty} f(t)\bar{g}_\gamma(t)dt = Ae^{i\phi}, \tag{21}$$

where $\bar{g}_\gamma(t)$ denotes the complex conjugate of $g_\gamma(t)$. The result of the inner product, $Ae^{i\phi}$, is complex for real signals. Its phase, ϕ, and parameters (u, s, ξ) determine the real waveform associated with the Gabor function. Since each Gabor function has unit energy, the magnitude of the inner product result, A, indicates the degree of matching between the real waveform associated with the Gabor function and the signal.

Using the definition of matching in Eq. 21, a signal is iteratively decomposed via matching pursuit. In each iteration, the best matching Gabor function in the dictionary is identified by finding the largest magnitude A of all the inner products. Then, its associated real waveform, determined by (A, ϕ, u, s, ξ), is subtracted from the signal, leaving a residual signal. This search and subtraction process is repeated on the residual signal until a stopping criterion is reached, such as a fixed number of iterations or when the norm of the residual signal reaches a threshold. The decomposition result consists of the sequence $(A_m, \phi_m, u_m, s_m, \xi_m)_{m\in M}$, where M is the number of iterations (and the resulting number of matching Gabor functions). The reconstructed signal using the matching pursuit decomposition is given by,

$$\hat{f}(t) = \sum_{m=1}^{M} Re\{< f, g_{\gamma_m} > g_{\gamma_m}(t)\}. \tag{22}$$

4.2.2 Numerical Implementation

The numerical implementation of matching pursuit requires the discretization of the dictionary, the search for the best matching basis functions, and the strategy to enhance the resolution of decomposition. The corresponding approaches depend upon the specific applications and the chosen basis functions. For example, Gribonval and Bacry [105] propose a dictionary of harmonically related Gabor functions and an implementation method for audio signal decomposition. Czerepinski *et al.* [106] discuss the dictionaries and fast implementation of matching pursuit for video coding. In [107, 108], a wave-based dictionary and associated algorithm are introduced for target identification. Fast implementation methods for Gaussian Chirplet functions are discussed in [109, 110] from the view of optimization. The size and discretization of the dictionary are also examined from a purely mathematical point of view in [92, 111].

Here, we propose a numerical implementation method of matching pursuit specifically tailored for the decomposition of guided and diffuse ultrasonic signals. The method is described below in four parts: the discretization of the dictionary, the fast computation of the inner product, the interpolation of parameter space for higher decomposition resolution, and the evaluation of the method.

4.2.2.1 Discretization of the dictionary

To numerically implement the matching pursuit method, the first issue is to select a discrete subset in the continuous parameter space of $\gamma = (u, s, \xi)$; i.e., to define a finite dictionary of Gabor functions. Mallat and Zhang proposed a particular finite dictionary given in the discrete time domain [92],

$$g_{\gamma_d}(n) = \frac{1}{\sqrt{2\pi}s_d} e^{-\frac{(n-u_d)^2}{2s_d^2}} e^{i\xi_d t}, \tag{23}$$

and

$$\gamma_d = (s_d, u_d, \xi_d) = (a^j, pa^j\Delta u, ka^{-j}\Delta\xi), \tag{24}$$

with $a = 2$, $\Delta u = \frac{1}{2}$, $\Delta\xi = \pi$, $(j, p, k) \in Z^3$. In Eq. (24), $0 \leq j \leq \log_2 N$, where N is the length of the signal, so that s_d ranges from 1 to N. For each value of s_d, the time and frequency discretization intervals are $\frac{s}{2}$ and $\frac{\pi}{s}$, respectively. With the additional conditions $0 \leq p < N(2^{-j+1})$ and $0 \leq k < 2^{j+1}$, the ranges of time shift u_d and frequency ξ_d are $[0, N)$ and $[0, 2\pi)$, respectively.

The selection of this finite dictionary is closely related to the frame theory used in the wavelet transform [94]. The dictionary is succinct and complete from a mathematical point of view. However, it is generally unsuitable for decomposing ultrasonic signals comprised of time-localized echoes, mainly because of the unrealistic range of values for s and ξ and the large jumps in time shift u_d. For ultrasonic signal decomposition, time-localized Gabor functions better match time-localized echoes; i.e., small values for the scale s are preferred. Moreover, it is desirable that the frequency range of the Gabor functions in the dictionary be matched to the spectrum of the signal, and the discretization interval be independent of the scale s to achieve a uniformly high resolution. Finally, a small and constant discretization interval for the time shift is preferred to obtain the property of translation invariance for the decomposition. Therefore, we propose an alternative dictionary where the frequency ξ, scale s and time shift u are determined as follows to give meaningful decomposition results for an ultrasonic signal.

Frequency ξ The frequency ξ of a Gabor function is the center frequency of the spectrum of the Gabor function. The criterion of frequency selection is to obtain a match between a dictionary of Gabor functions and a signal in the frequency domain. If the ultrasonic transmission is narrow band, we can select the frequency ξ to be the excitation frequency [98]. For complex guided or diffuse ultrasonic waves resulting from a broadband excitation, the frequency content of the received signals depends upon the specimen and transducer geometries [112]. We thus choose the range of ξ

to be the bandwidth of the signal to be decomposed, where the bandwidth (ω_1, ω_2) is defined as,

$$\omega_1 = \arg\min_{\omega}\{|f(\omega)| \geq \alpha \cdot f_{max}\}, \tag{25}$$

$$\omega_2 = \arg\max_{\omega}\{|f(\omega)| \geq \alpha \cdot f_{max}\}, \tag{26}$$

where $f(\omega)$ is the spectrum of the signal, f_{max} is the peak magnitude, α is a fraction of the peak amplitude (set to 0.1 for the work presented here), and ω is the radian frequency. The set of ξ_n would then consist of discrete values that evenly span this frequency range. A coarse grid is preferred to reduce the computational burden; dividing the range into four segments is a reasonable rule of thumb.

Scale s The scale s of a Gabor function determines the support of the function in both the time and frequency domains since s, the standard deviation of the Gaussian window in the time domain, also determines the width in the frequency domain. If we define the support S of the Gaussian window in the time domain to be $\pm 3s$ (six standard deviations), then $s = S/6$. To ensure that the Gabor functions in the dictionary are localized in time, we explicitly relate the support S to the center frequency ξ. Specifically, for each frequency ξ_n, we form a group of Gabor functions with $S_i = p_i(2\pi/\xi_n)$ where p_i is the number of cycles, and the values of p_i evenly span the range of $[p_a, p_b]$. The value of p_a determines the narrowest echo that will be matched to a signal, and the value of p_b is chosen to avoid Gabor functions with too big of a support. The set of scale s can be expressed as:

$$s_n^i = \frac{S_i}{6} = \frac{1}{6}\, p_i\, \frac{2\pi}{\xi_n}. \tag{27}$$

As an example, Fig. 17 shows one baseline diffuse ultrasonic signal measured from the first experiment (5 °C, first $1000\mu s$) along with its spectrum. Fig. 18 illustrates a possible set of parameters s and ξ for this signal. The frequency range is 0.06 MHz

to 0.48 MHz, as determined by Eqs. (25) and (26), and is divided into 4 segments. For each frequency, the values of s are selected so that the Gabor functions cover 3, 6.5 and 10 cycles of that frequency.

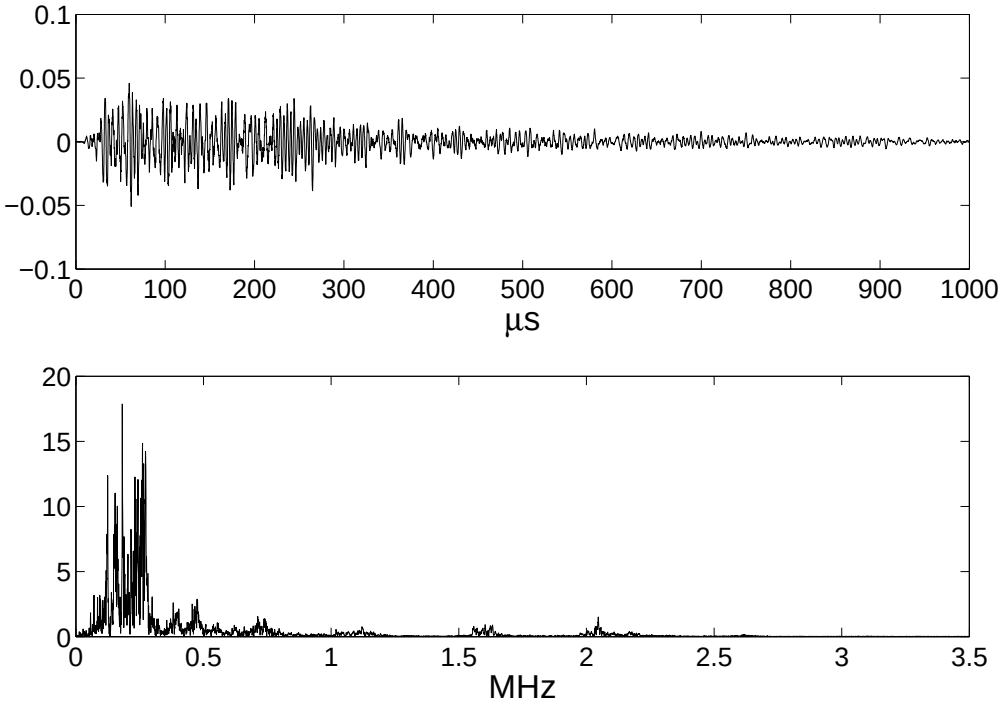

Figure 17: A diffuse ultrasonic signal recorded from experiment #1 and its spectrum

Time shift u To achieve the maximum resolution in time shift, the set of u is selected independently of ξ and s:

$$u_k = kT_s, \qquad k = 0, 1, 2, \cdots, N-1, \tag{28}$$

where T_s is the sampling interval.

4.2.2.2 Fast computation of the inner product and translation invariance

The second issue of the numerical implementation of matching pursuit is to compute the inner product defined in Eq. (21). Mallat and Zhang simplify this computation by pre-calculating the mutual inner products for all of the Gabor functions in the

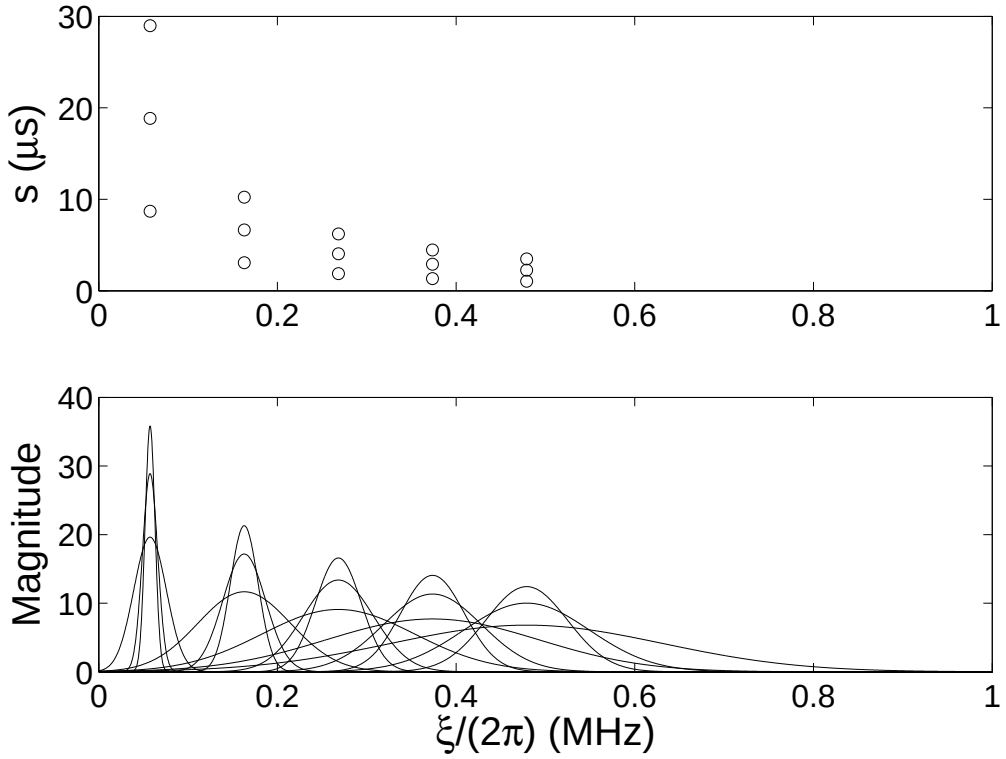

Figure 18: A scale-frequency (s, ξ) parameter set (upper plot) and the Fourier transform of the corresponding Gabor functions (lower plot)

dictionary [92]. As an alternative, it is desirable to calculate the inner product of Eq. (21) directly in each iteration if the composition of the dictionary needs to change. It is well known that for the continuous wavelet transform, the inner product between a signal and a wavelet with a fixed scale can be efficiently calculated in the frequency domain for all translations [94]. This same method can be readily used here if the phase term of the Gabor functions is modified. In fact, the Gabor function can also be written as [95, 105]:

$$g'_\gamma(t) = \frac{1}{\sqrt{2\pi}s} e^{-\frac{(t-u)^2}{2s^2}} e^{i\xi(t-u)}. \tag{29}$$

The difference between Eq. (20) and Eq. (29) is in the phase term. With the above form, the complex sinusoid shifts along with the Gaussian window. It is easy to prove that if the result of a decomposition using $g_\gamma(t)$ is $(A_m, \phi_m, u_m, s_m, \xi_m)_{m \in M}$, then

the result of decomposition using $g'_\gamma(t)$ is $(A_m, \phi'_m, u_m, s_m, \xi_m)_{m\in M}$. In other words, $g_\gamma(t)$ and $g'_\gamma(t)$ essentially represent the same dictionary within a phase term. In addition, the representation of Eq. (29) has the added advantage of the phase being independent of the time shift so that if a signal shifts in time, ϕ is unchanged and u changes by the time shift. This property is necessary for the decomposition to be translation invariant; *i.e.*, for A_m, ϕ_m, s_m, and ξ_m to all remain unchanged if the signal shifts by an integral multiple of samples. With the representation of Eq. (29), the inner product of Eq. (21) can be written as:

$$\begin{aligned} < f, g'_{(u,s,\xi)} > &= \int_{-\infty}^{+\infty} f(t) \frac{1}{\sqrt{2\pi}s} e^{-\frac{(t-u)^2}{2s^2}} e^{-i\xi(t-u)} dt \\ &= \int_{-\infty}^{+\infty} f(t) \frac{1}{\sqrt{2\pi}s} e^{-\frac{(u-t)^2}{2s^2}} e^{i\xi(u-t)} dt \\ &= f(u) * \{ \frac{1}{\sqrt{2\pi}s} e^{-\frac{u^2}{2s^2}} e^{i\xi u} \} \\ &= f(u) * g'_{(0,s,\xi)}(u), \end{aligned} \tag{30}$$

where the asterisk denotes convolution. By using Eq. (30), the inner product is converted into a convolution with respect to u, for fixed s and ξ. The Fourier transform of $g'_{(0,s,\xi)}(t)$ can be expressed analytically as,

$$\hat{g}'_{(0,s,\xi)}(\omega) = e^{-\frac{(\omega-\xi)^2 s^2}{2}}, \tag{31}$$

thus enabling efficient computation of the convolution by multiplication in the frequency domain. To summarize, the proposed dictionary has small sets of s and ξ to limit the dictionary size, and a large set of u consisting of all samples in time. The Gabor functions with the appropriate phase term allow the inner products to be calculated as multiplications in the frequency domain, and the decomposition is translation invariant with respect to translations which are integral multiples of the sampling interval.

4.2.2.3 Improving decomposition performance via interpolation

For given ranges of u, s, and ξ, smaller discretization intervals generate a larger number of Gabor functions, which usually means a better decomposition in terms of both matching the signal and achieving good resolution in the three parameters. However, the computational effort increases as the size of the dictionary increases. Therefore, the third issue regarding the numerical implementation is to improve the decomposition performance without increasing the size of the dictionary.

In [92], Mallat and Zhang propose a double search strategy. Specifically, if g_{γ_0} is the best matching Gabor function in a dictionary during an iteration, then an even better Gabor function $g_{\bar{\gamma}_0}$ could be found by searching the neighborhood of γ_0 with the Newton method. Such a gradient based search is also used in [99] where the Gauss-Newton algorithm is implemented for fast parameter estimation. Here, based on the characteristics of the previously defined dictionary, we propose a strategy to find $g_{\bar{\gamma}_0}$ in the neighborhood of γ_0 by first interpolating the parameters s and ξ together, and then interpolating the parameter u.

Interpolation of s and ξ The initial sets of s and ξ consist of discrete values where, for a given ξ, values of s evenly span a designated range. Although the discretization intervals can be arbitrarily determined, a coarse grid is preferred to limit the size of the dictionary. In Fig. 18, the frequency ξ consists of five values, and for each ξ, three values are selected for the scale s, yielding a total of 15 Gabor functions for which all possible values of the time shift u are considered. To improve the decomposition performance based on such a coarse grid, a method of interpolation is used. Specifically, if $\gamma_0 = (u_0, s_0, \xi_0)$ yields the best matching Gabor function on the coarse grid during an iteration, then in the scale-frequency plane, we can insert a rectangular fine grid (s_i, ξ_i) centered at (s_0, ξ_0) and calculate the corresponding inner products $< f, g_{(u,s_i,\xi_i)} >$. For each (s_i, ξ_i), the maximum value of $< f, g_{(u,s_i,\xi_i)} >$ with

respect to u is found. These maxima are then interpolated over an even finer interpolation grid, and a better parameter set $(\bar{s}_0, \bar{\xi}_0)$ is at the peak of this interpolation grid. Finally, the time shift u_0 is updated, where the new value $\bar{u}_0$ is at the maximum of the updated inner product $< f, g_{(u,\bar{s}_0,\bar{\xi}_0)} >$.

Fig. 19 shows the interpolation method applied to the signal of Fig. 17 during the first iterative step, where the circles are the coarse grid of Fig. 18, the dots are the fine grid points, and the plus sign is the better matching parameter set $(\bar{s}_0, \bar{\xi}_0)$. To ensure coverage in s and ξ, the fine grid area covers one full coarse grid interval in both the s and ξ directions. The optimum density of the fine grid depends upon how quickly the surface is changing in the (s, ξ) plane, and was empirically set to a 5×5 grid for the work presented here. This fine grid was then interpolated via cubic splines on a 40×40 grid to further improve the resolution by a factor of eight. Fig. 20 shows plots of the inner product magnitudes $< f, g_{(u,\bar{s}_0,\bar{\xi}_0)} >$ and $< f, g_{(u,s_0,\xi_0)} >$ versus u; only the first 350 μs are shown for a clearer illustration. It is clear from the figure that a significantly bigger peak value of the inner product, i.e., a better matching, is obtained by interpolation. The time shift corresponding to the bigger peak is the new time shift $\bar{u}_0$, which is different than u_0.

Interpolation of u Although the discretization interval for u is small since it is defined to be the sampling interval, an even better value of u can be found to form a better matching Gabor function if the interpolation method is also applied with respect to u. The inner product curve $< f, g_{(u,\bar{s}_0,\bar{\xi}_0)} >$ shown in Fig. 20 is expanded in Fig. 21 around $\bar{u}_0$. One can see that the resolution in u is limited by the sampling interval. In Fig. 21, the five point neighborhood of $\bar{u}_0$ is interpolated using 100 equally spaced points, leading to an even better value, $\bar{u}_0'$.

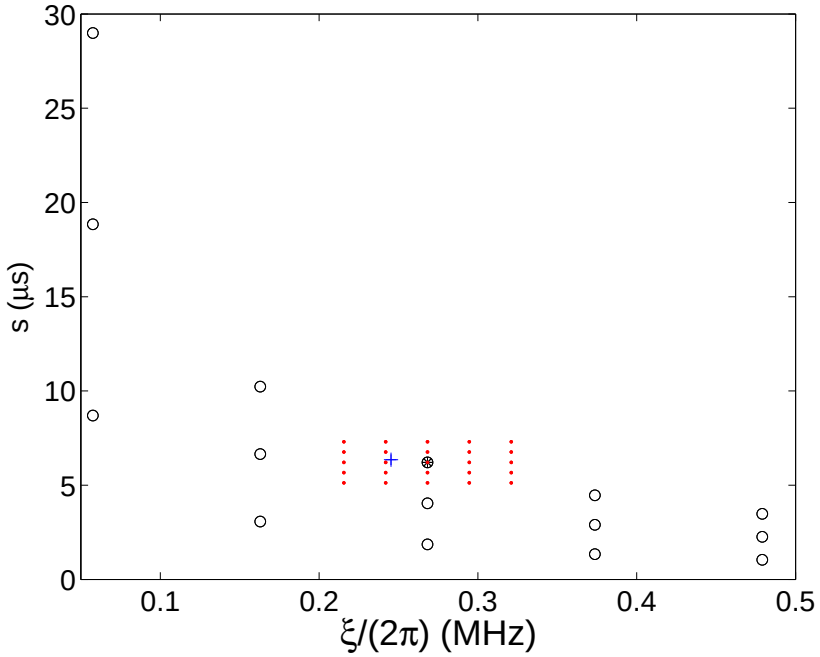

Figure 19: Illustration of the coarse grid (open cycles) and fine grid (dots) in the (s, ξ) plane. The peak for the coarse grid (asterisk) is at $(s_0, \xi_0/(2\pi)) = (6.21, 0.27)$, and the interpolated peak for the fine grid (plus sign) is at $(\bar{s}_0, \bar{\xi}_0/(2\pi)) = (6.35, 0.25)$

4.2.2.4 Efficiency of the proposed implementation

The performance of decomposing a signal via matching pursuit can be evaluated from three different aspects: the rate of decomposition, the resolution of decomposition, and the computational time. To show the efficiency of the proposed implementation method, the signal of Fig. 17 (12500 points in length) is decomposed in two ways. First, the signal is decomposed using the coarse grid shown in Fig. 18; parameter interpolation is not applied. Second, the interpolation method demonstrated in Figs. 19, 20, and 21 is used. In both cases, the signal is decomposed with 300 iterations.

The rate of decomposition is represented by the curve of residual energy versus number of iterations. Fig. 22 plots the curves for the above two cases. As expected, the rate of decomposition is substantially increased by the method of interpolation.

The resolution of decomposition is determined by the discretization intervals of the dictionary. For the coarse grid shown in Fig. 18, the discretization intervals of ξ

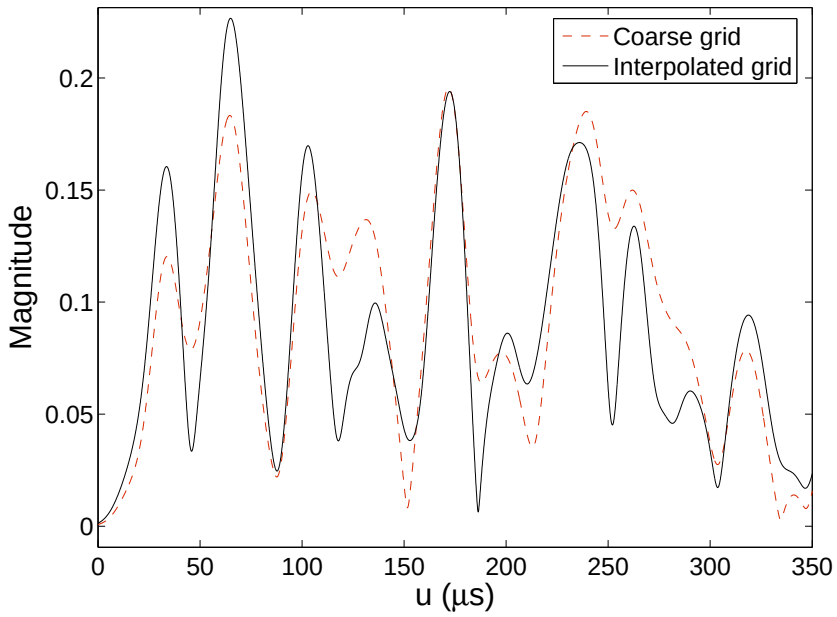

Figure 20: Magnitude of the inner product $< f, g_{(u,s_0,\xi_0)} >$ for the coarse grid and $< f, g_{(u,\bar{s}_0,\bar{\xi}_0)} >$ for the interpolated fine grid; the respective peaks are located at $u_0 = 171.84$ μs and $\bar{u}_0 = 64.96$ μs

and s are 1/4 and 1/3 of their ranges, respectively. By the method of interpolation (40×40 interpolation over 5×5 fine grids around a given coarse grid point), the intervals are decreased to 1/160 and 1/120, respectively. The discretization interval of u is also decreased from the sampling interval T_s to $T_s/25$, as shown in Fig. 21.

The computational time for each iterative step is dominated by the calculation of the inner product $< f, g_{(u,s,\xi)} >$, which is the convolution $f(u) * g'_{(0,s,\xi)}(u)$ for the method implemented here. For one matching pursuit iteration, if the number of combinations of s and ξ is M (total number of coarse and fine grid points), then the calculation of the inner products consists of one forward FFT of the signal (or residual signal) and M inverse FFTs to convert the convolutions back to the time domain. If the signal length is N, where N is a power of 2, then the computational complexity for the inner products is $O(MNlog_2N)$. Therefore, the total number of combinations of s and ξ in the coarse and fine dictionaries determines the computational time.

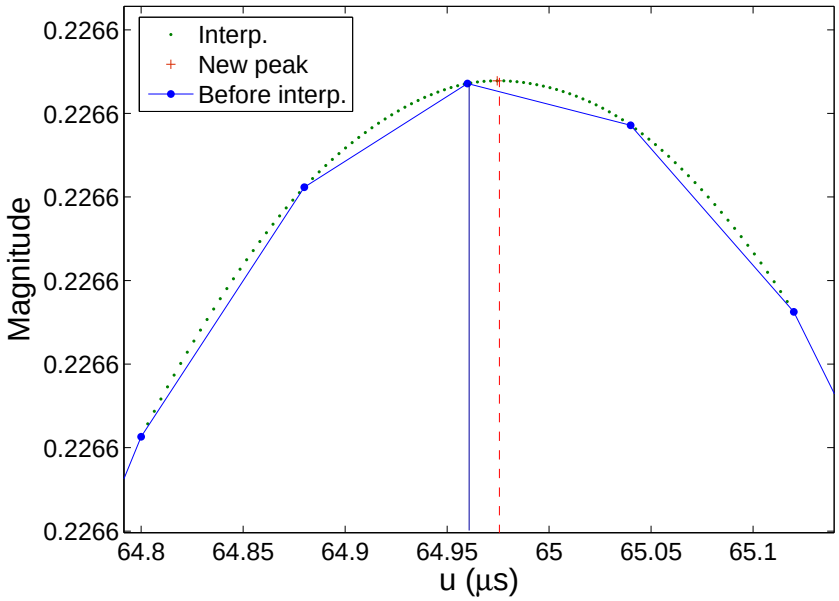

Figure 21: Interpolation of $< f, g_{(u,\bar{s}_0,\bar{\xi}_0)} >$ in the neighborhood of $\bar{u}_0 = 64.96$ μs. The interpolated peak is at $\bar{u}_0' = 64.97$ μs.

For the coarse grid in the above example, 15 combinations are used in each iteration, while for the method of interpolation, the number is 40 (15 coarse plus 25 fine). The computational time for one iteration is approximately 0.6 s for the coarse grid (15 combinations) using a typical personal computer (1.8 GHz CPU speed and 1 Gbytes of memory). For the method of interpolation, the time is approximately 1.5 s per iteration (40 combinations). Although the computational time is longer when interpolation is applied, the rate and resolution of decomposition are significantly improved. Moreover, the improvement in resolution cannot be achieved by simply using a bigger dictionary with finer discretization intervals. For example, obtaining a 4 times resolution improvement for s and ξ, as obtained from the adaptive insertion of 25 fine grid points around a given coarse grid point, requires 325 combinations of s and ξ and the computational time for one iteration increases to approximately 21.0 s.

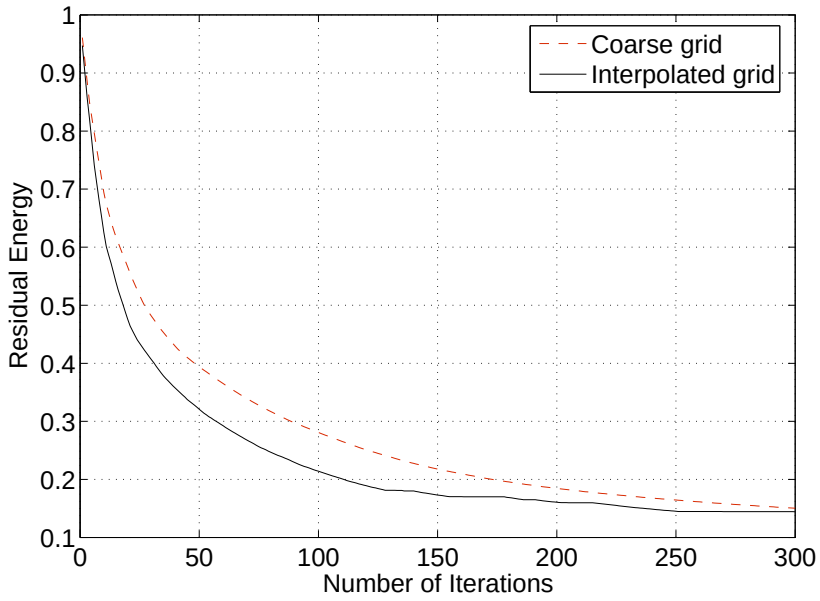

Figure 22: Energy of the residual signal versus number of iterations

4.2.3 Distributed and Constrained Matching Pursuit

A straightforward application of matching pursuit is to locate and estimate echoes in ultrasonic signals because the family of Gabor functions, or other redundant basis functions, are qualitatively and quantitatively very similar to ultrasonic echoes; published research on this topic is summarized in Sec. 4.2.1. These approaches become limited when signals have a high degree of complexity. For diffuse ultrasonic signals measured from structures with many reflectors and scatterers, identifying echoes becomes at best ambiguous and at worst impossible. However, we still can use matching pursuit to find portions of waveforms where energy is concentrated because these portions are automatically captured by the matching basis functions during signal decomposition. In terms of the dictionary of Gabor functions, the parameters (A, ϕ, u, s, ξ) of the real waveform associated with a matching Gabor function characterize the amplitude, phase, time, scale, and frequency of such a waveform portion. We refer to these real waveforms associated with the matching Gabor functions as characteristic wavelets. If we use the characteristic wavelets to represent the signal,

then features can be extract from the parameters of these wavelets. Here, we propose two types of decompositions for the baseline signal and the monitored signal, respectively, to enable signal changes to be quantified for comparison.

4.2.3.1 Distributed decomposition on the baseline

The purpose of decomposing the baseline signal using matching pursuit is to represent this signal with characteristic wavelets quantified by $(A_m, \phi_m, u_m, s_m, \xi_m)_{m \in M}$, where M is the number of iterations. Because the Gabor functions defined in Eq. (29) have unit energy in the time domain, the value of A_m, which is monotonically decreasing with m, is a measure of the energy of each characteristic wavelet. Therefore, a direct decomposition will eventually capture the energy of the baseline with increasing numbers of iterations. However, such a free (free in the sense that the parameters are unrestricted) decomposition results in heavily overlapped wavelets. In Fig. 23, a free decomposition of the signal of Fig. 17 is plotted in the upper plot (30 iterations); a short interval from 180 μs to 280 μs is plotted in the lower plot. It can be seen that the decomposition result consists of many overlapped characteristic wavelets rather than wavelets distributed on the time axis. This is because the residual waveform at the earlier part of the signal still has bigger energy than the original waveform in the later part due to its decaying nature. When representing a diffuse ultrasonic signal with a small number of characteristic wavelets, it is desired that the decomposition covers the whole length of the signal before overlapped wavelets occur because the later part of the signal is expected to contain valuable information as well. Therefore, a method of distributed decomposition is proposed.

The basic idea is to flag locations in time where characteristic wavelets are already located. One possibility is to mark the time interval that corresponds to the time span of the best matching wavelet after each iteration, so that in the next iteration, only wavelets with center time u outside of the marked interval are considered. However,

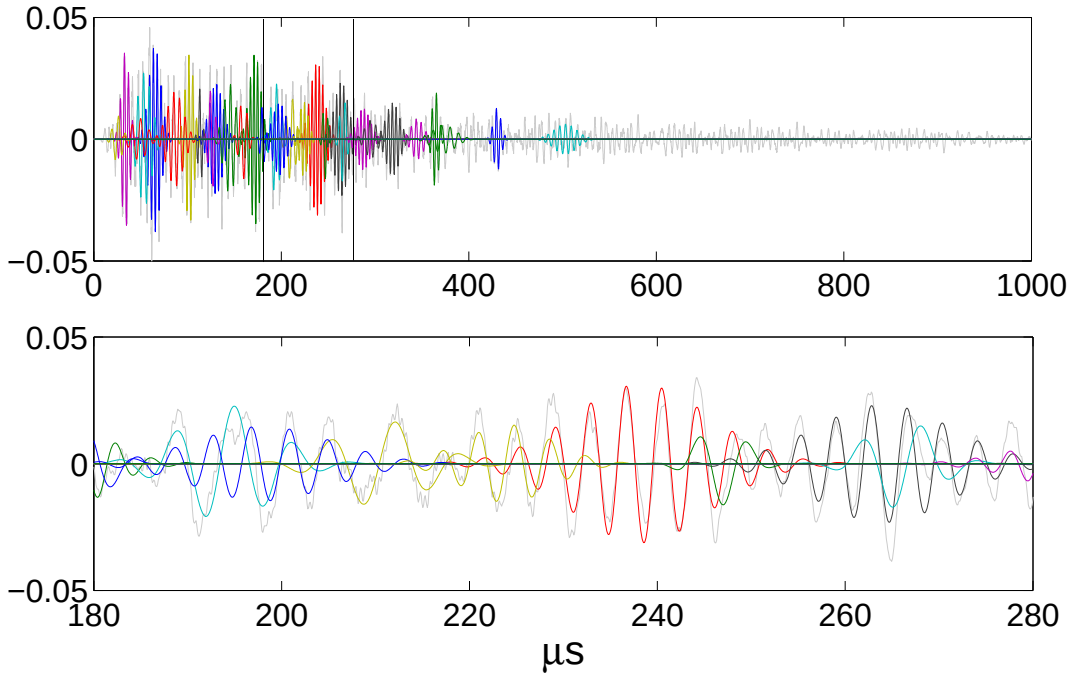

Figure 23: Free decomposition of the baseline signal in Fig. 17 with 30 iterations (the electronic version of the figure is in color).

this strategy only guarantees that a later wavelet is centered outside of the span of the previous wavelets, and does not preclude the situation where a later wavelet with a large span may in turn overlap a previous wavelet. Therefore, a somewhat different method is introduced for the distributed decomposition which eliminates this problem. Specifically, if we have n best matching wavelets obtained from the first n iterations; summarized as

$$\{A_i, \phi_i, u_i, s_i, \xi_i\}_{(i=1,n)}, \tag{32}$$

then, in the $(n+1)^{st}$ step, for each s_j in the dictionary ($j = 1 - 15$ for the example dictionary), we mark the time axis with n intervals. Each interval is centered at u_i and its span is $\pm\beta \cdot \max(s_i, s_j)$ where β determines the span of a given s ($\pm 3s$ is previously used for the support of a wavelet with scale s).

Figure 24 shows the distributed decomposition of signal of Fig. 17, where $\beta = 2.8$

is used to allow slight overlap. It can be seen that for the same number of iterations, the new decomposition consists of characteristic wavelets more evenly distributed on the time axis. Heavily overlapped wavelets are excluded, as shown in the lower zoomed plot of Fig. 24.

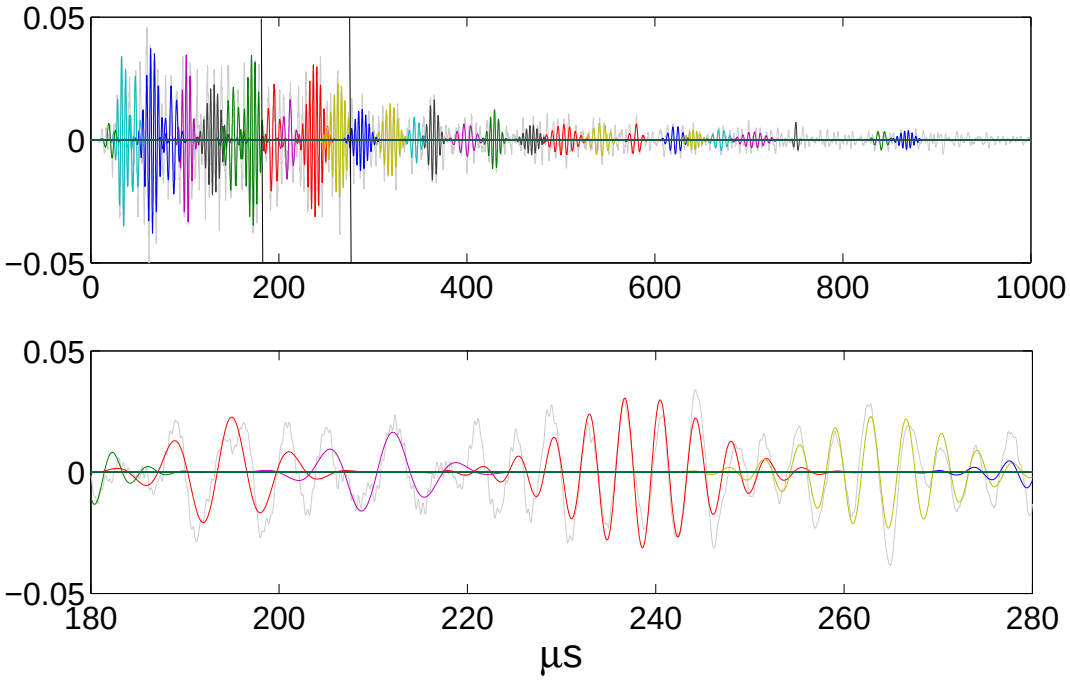

Figure 24: Distributed decomposition of the baseline signal in Fig. 17 with 30 iterations (the electronic version of the figure is in color).

Using the distributed matching pursuit decomposition, the whole time axis will eventually become marked as the number of iterations increases, precluding the addition of any more wavelets. At this point, all marks could be removed so that the decomposition could continue on the residual signal with new wavelets overlapping the original ones but not each other. The distributed method may decrease the rate of decomposition but the advantage is that we obtain matching wavelets which are evenly distributed in time. Moreover, by removing all marks when the time axis is fully marked, this decomposition method is analogous to the idea of a multi-resolution decomposition. For the work here, the decomposition is terminated shortly before this

point after the signal has been decomposed into a predetermined number of wavelets.

4.2.3.2 Constrained decomposition on monitored signals

For structural health monitoring, a monitored signal is typically compared to a baseline signal to determine the structural status. Since information in the baseline signal is represented by its characteristic wavelets $(A_m, \phi_m, u_m, s_m, \xi_m)_{m \in M}$, we also decompose the monitored signal to obtain corresponding wavelets $(A'_m, \phi'_m, u'_m, s'_m, \xi'_m)_{m \in M}$. However, a free or distributed decomposition on the monitored signal is not desirable because for complex ultrasonic signals, small signal changes may lead to significant differences in the decomposition results. Therefore, we decompose the monitored signal using matching pursuit with constraints. The idea is to force the shape of each characteristic wavelet to be the same as was determined for the baseline, but allow the magnitude and time to change as is typical for ultrasonic signals when structural and environmental conditions change. For example, temperature changes cause local time shifts, and scattering by damage can cause amplitude variations of specific echoes as energy is redistributed in the structure [11, 86].

Specifically, the parameters (ϕ, s, ξ) define the shape of the characteristic wavelet and (A, u) define the magnitude and time of that wavelet. We apply the constraint $(\phi'_m = \phi_m, s'_m = s_m, \xi'_m = \xi_m)_{m \in M}$ to the decomposition of monitored signals so that the shapes of the characteristic wavelets of the baseline signal are kept the same for the decomposition of the monitored signal. With this constraint, the decomposition leads to the set of characteristic wavelets quantified by $(A'_m, u'_m, \phi_m, s_m, \xi_m)_{m \in M}$, where the differences between characteristic wavelets of the baseline and the monitored signal are restricted to changes in magnitude and time only. By keeping a one-to-one correspondence between the characteristic wavelets of the monitored signal and the baseline, we are able to track changes in magnitude and time of a specific characteristic wavelet.

In practice, an additional constraint, $|u'_m - u_m| < \delta_m$, is placed on the time shift u'_m of each matching Gabor function. The value of δ_m is set to ensure that a matching Gabor function does not jump to another portion of the monitored signal but stays in the vicinity of the original matching Gabor function. In this paper, we set $\delta_m = \pi/2\xi_m$ so that $|u'_m - u_m|$ is limited to 25% of the corresponding period. Finally, it should be noted that since only selected Gabor functions are used for the constrained decomposition, the inner product can be computed directly in either the time or frequency domain without the need for interpolating s or ξ, while for the baseline decomposition, the proposed interpolation method is used to obtain high resolution in u, s and ξ.

The idea of distributed and constrained decompositions of baselines and monitored signals is illustrated in Fig. 25. In the figure, the upper plot shows a baseline signal (25.0 °C of the experiment #1) and its distributed decomposition with 30 iterations. The bottom plot in the figure shows one signal after a structural change (25.0 °C, 5.08 mm notch; from experiment #1) and its constrained decomposition. Fig. 26 shows the decomposition results in the time interval of 280 μs to 450 μs. The waveform changes of the original signals are now transformed to the amplitude and time changes of the characteristic wavelets. We can quantify differences between a monitored signal and a baseline by comparing sequences $(A'_m, u'_m)_{m\in[1,30]}$ and $(A_m, u_m)_{m\in[1,30]}$, which provides a basis for differential feature extraction.

4.3 Embedding Theory and Simulated Chaotic Excitation

In this thesis, a phase space differential feature extraction method is implemented to compare diffuse ultrasonic signals. The method is derived from the phase space feature extraction technique used in vibration-based SHM [113, 114]. The idea of the original technique is to excite structural vibrations using chaotic excitations, convert the response signal of the vibration into phase space by the method of embedding,

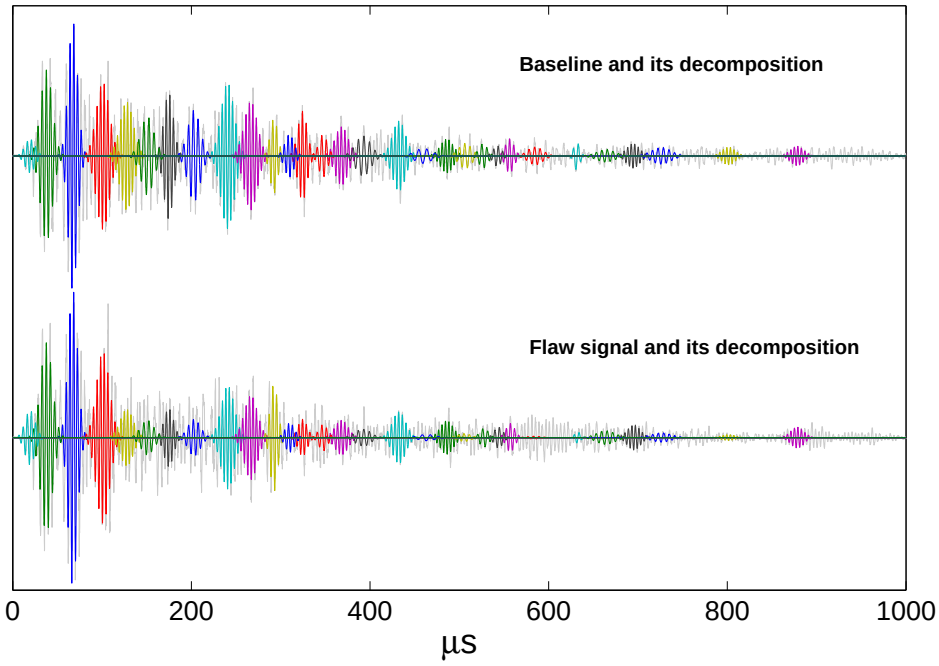

Figure 25: Decomposition of a baseline signal (25.0 °C, experiment #1) and a monitored signal (25.0 °C, 5.08 mm notch, experiment #1) with 30 iterations.

and then extract features from phase space. In this section, the theory of embedding and the simulation of chaotic excitations are introduced. A feature extraction method based on applying both of these methods to diffuse ultrasonic signals is described in Sec. 5.4.

4.3.1 Theory of Embedding

Embedding, also known as state space reconstruction, is widely used for nonlinear time series analysis. The basic idea is that the multi-dimensional phase portrait in the phase space of a multi-dimensional dynamic system can be reconstructed from a scalar time series that is measured from one state variable of the system. Consider a dynamic system described by

$$\dot{X} = F(X), \tag{33}$$

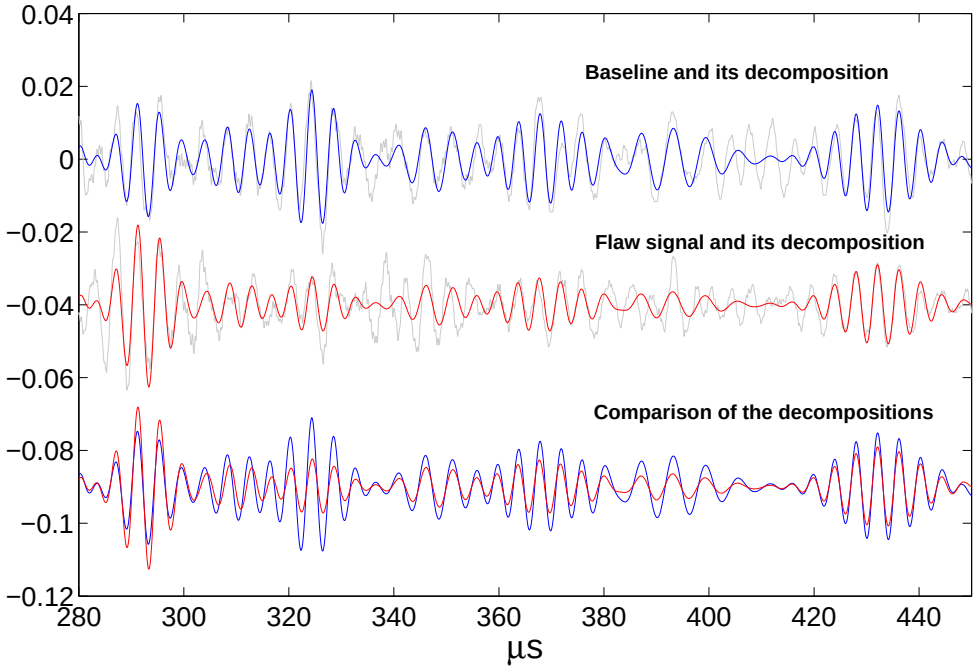

Figure 26: Decomposition results of Fig. 25 shown in the interval from 380 μs to 565 μs.

where X is the state variable vector of dimension d. Suppose we can only measure one state variable through a measurement function

$$s_n = S(X_n), \tag{34}$$

where $n = 1, ..., N$ is the time index, and s_n is the measured scalar time series. The embedding theorem [115, 116] proves that the phase portrait X_n can be reconstructed from s_n by the method of delayed coordinate embedding:

$$\hat{X}_n = (s_{n-(m-1)\tau}, s_{n-(m-2)\tau}, ..., s_{n-\tau}, s_n), \tag{35}$$

where $\hat{X}_n$ is an estimate of the state variable X_n, m is the embedding dimension, and τ is the time delay measured in samples.

As explained in the mathematical proof of the embedding theorem, proper values of m and τ are critical for the embedding to be valid. For the time delay τ, the

criterion is to find the minimal time delay value for which the original and the time delayed time series become least correlated to each other. This goal can be achieved in two ways. The first method is to calculate the mutual information of the time series; the time lag corresponding to the first minimum of the mutual information is the best time delay [117]. The second method is to calculate the auto-correlation function; the time lag corresponding to the first zero crossing is chosen to be the time delay [118].

The embedding dimension m must satisfy the necessary condition $m > 2d$. In practice, one straightforward method of determining m is to post-calculate the box dimension [115]. The box dimension is an approximation of the dimension of a phase portrait, which is especially useful for fractal dimensions. It is defined as

$$D = \lim_{\varepsilon \to 0} \frac{lnN(\varepsilon)}{ln(1/\varepsilon)}, \tag{36}$$

where $N(\varepsilon)$ is the minimal number of l-dimensional boxes with side length ε that enclose the phase portrait existing in an l-dimensional state space. If the same time series is embedded into multiple state spaces with increasing dimension l, its box dimension will reach a plateau, which means that the phase portrait is fully reconstructed. Consequently, the minimal embedding dimension m is the integer rounded up from the plateau value. A higher embedding dimension is not necessary and is undesirable because of the extra computational effort required.

4.3.2 Simulated Chaotic Excitation

In the vibration-based SHM using phase space feature extraction, the structure is excited by a continuous chaotic signal. The vibration response is recorded as a time series after the vibration reaches steady state. Then, the recorded signal is converted into state space for feature extraction.

There are three major reasons to use a chaotic excitation. First, it is broad-band and thus excites a range of frequencies. Second, it can be generated from low-dimension dynamic systems so that low-dimension embedding is applicable [119]. Third, a chaotic signal is extremely sensitive to the initial conditions of the dynamic system. In the framework of SHM, this sensitivity to initial conditions suggests that the measured response to the chaotic excitation may be sensitive to structural changes.

The premise of embedding the recorded signal into state space is that the monitored structure is a multi-dimensional system. Consequently, the vibration of the system cannot be completely captured by the one-dimensional recorded signal. Therefore, state space reconstruction is used to obtain more information about the structure.

The Lorenz system is the first proposed and one of the most widely used chaotic systems for generating chaotic excitations [114]. It is given by a set of ordinary differential equations:

$$\dot{x_1}/k = \sigma(x_1 - x_1), \tag{37}$$

$$\dot{x_2}/k = rx_1 - x_2 - x_1x_2, \tag{38}$$

$$\dot{x_3}/k = x_1x_2 - bx_3, \tag{39}$$

where σ, r, and b are typically 10, 28 and 8/3, respectively. The parameter k controls the oscillation frequency of the system. Figure 27 shows the evolution of the system starting from the initial position $(0, 1, 0)$. It can be seen that the trajectory falls into a confined space. Furthermore, it can be proven that the trajectory never repeats itself. These two properties lead to the name *strange attractors* for the solutions of this kind of system.

With the Lorenz system, the sensitivity of the chaotic system to its initial conditions can be clearly demonstrated. In Fig. 28, 100 initial phase points close to each other are plotted in the top left plot. These points are around the position $(0, 1, 0)$,

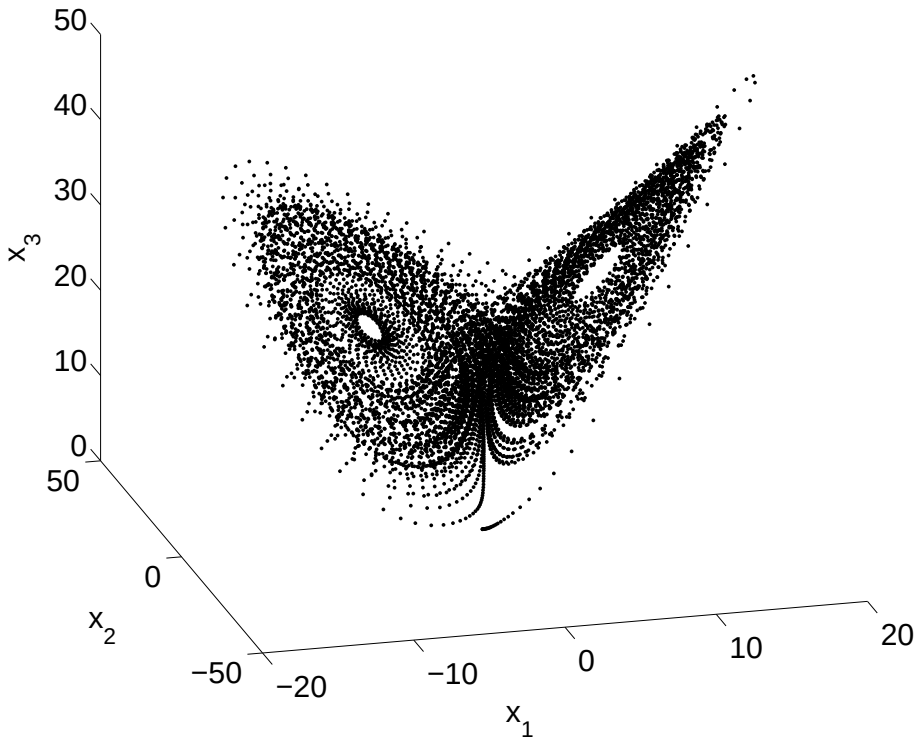

Figure 27: Lorenz attractor

and the distances between them are too small to distinguish. After 0.18 ms evolution, these points start to diverge (top right plot). At 1 ms, these points are almost everywhere in the phase space (bottom right plot).

The method of embedding can also be illustrated using the Lorenz attractor. For example, if state variable x_1 of the attractor is the only signal available, then the original attractor can be reconstructed using x_1 and its time delayed versions. In this case, the original dimension d is known to be 3. According to the theory introduced in Sec. 4.3.1, the embedding dimension for a valid embedding should be 7. However, for the purpose of illustration, here the embedding dimension is chosen to be 3. The time delay is chosen to be 7 sample intervals. The three state variables of the original attractor are reconstructed as

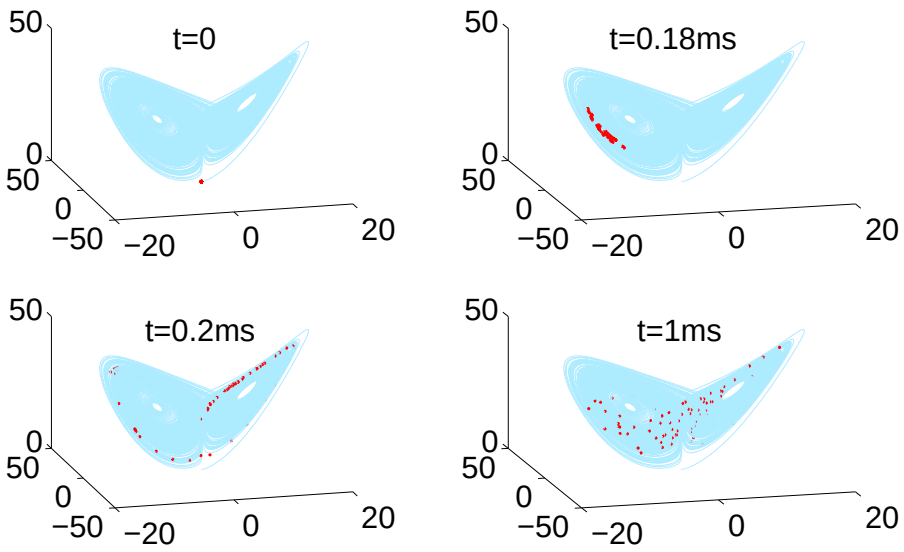

Figure 28: Sensitivity of the Lorenz system to initial conditions

$$\hat{x}_1(i) = x_1(i), \tag{40}$$

$$\hat{x}_2(i) = x_1(i+7), \tag{41}$$

$$\hat{x}_3(i) = x_1(i+14), \tag{42}$$

where $i = 1, ..., N - 14$, and N is the length of x_1 in samples. The reconstructed Lorenz attractor is plotted in Fig. 29. It is an under-embedded phase portrait and *not* geometrically equivalent to the original one, but it illustrates the idea of embedding, as the similarity between Fig. 27 and Fig. 29 is observed (two topological holes).

However, for the diffuse ultrasonic signals excited by an impulse, the method of embedding cannot be directly applied because these signals are transient. The signal decays to zero as the energy dissipates inside the structure, as shown in Fig. 6. A direct application of the method of embedding to the transient diffuse ultrasonic signal results in an embedded phase portrait whose trajectory always falls into the origin. This causes undesired similarity between embedded phase portraits and thus

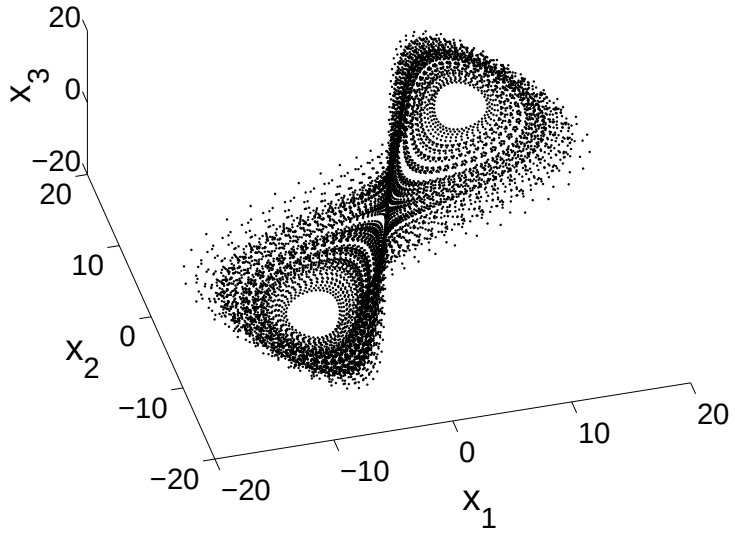

Figure 29: Pseudo-reconstructed Lorenz attractor

is a disadvantage for comparing phase portraits. To avoid such a situation, the transient diffuse ultrasonic signal is first convolved with a computer-generated continuous chaotic signal, and this convolved signal is then used for embedding. The effect of the ultrasonic signal decay is then removed because the trajectories no longer fall into the origin. Furthermore, if the transient diffuse ultrasonic signal is viewed as the impulse response of the structure and the chaotic signal is viewed as the system input, then the convolved signal is the simulated response to the chaotic excitation.

In the vibration-based approach, the state variable x_1 of the Lorenz system is usually used as the chaotic excitation signal. To simulate this excitation, the Lorenz system is solved numerically. Then, each recorded diffuse ultrasonic signal is convolved with the state variable x_1. Finally, the convolved signal is embedded into phase space. Figure 30 shows a typical diffuse ultrasonic signal recorded in experiment #1 (first 500 μs), the computer-generated signal x_1, and the corresponding convolved signal in the time domain. Figure 31 plots the phase portrait reconstructed from the convolved signal, where the embedding dimension m is calculated to be 3, using the

plateau method, and the time delay is eight samples, using the auto-correlation function. The simulation of a chaotic excitation using convolution and its phase portrait reconstruction using embedding provide the foundation for the application of phase space feature extraction to diffuse ultrasonic signals.

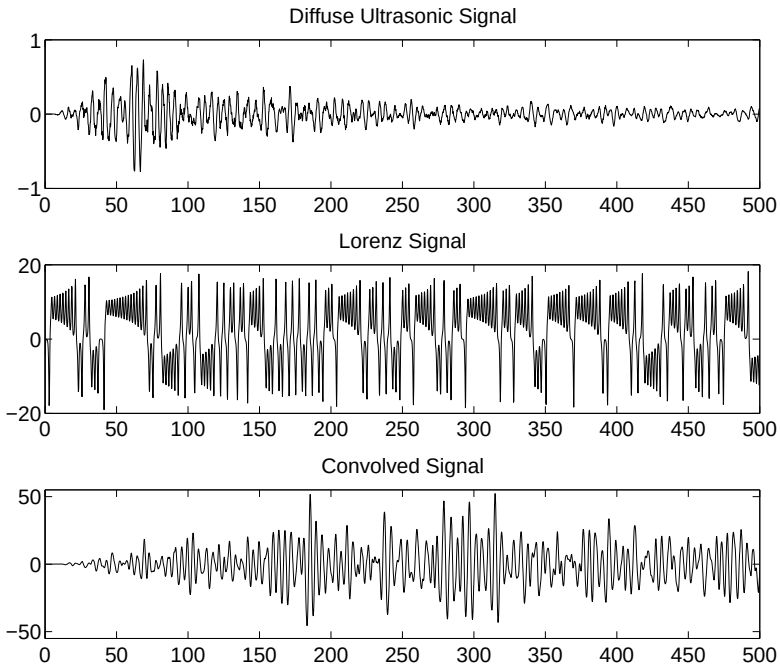

Figure 30: Signals of the convolution simulating the chaotic excitation

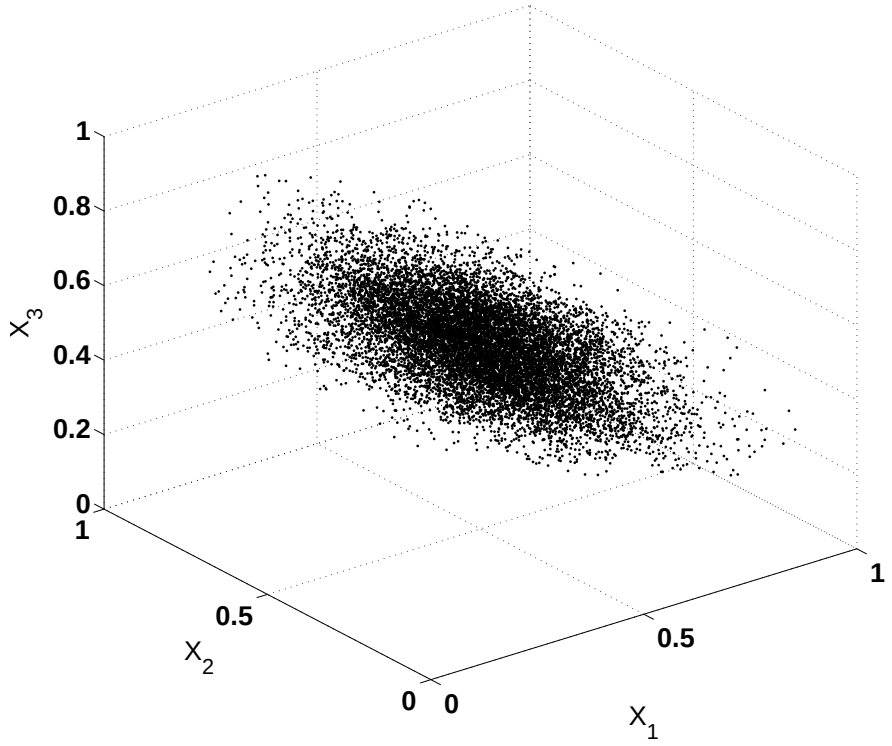

Figure 31: Phase portrait reconstructed from the convolved signal

CHAPTER V

METHODOLOGY

In this chapter, an integrated procedure for damage detection is proposed, based on the theories and mathematical methods introduced in the previous chapter. The procedure is shown in the form of a flowchart in Fig. 32. In this procedure, baseline signals are recorded at different temperatures which span the expected operating range. The temperature effects on diffuse ultrasonic waves are compensated by selecting and processing baselines to best match the monitored signal. Then, various differential features are extracted from the baseline and the signal. Finally, a statistical threshold selection method combined with a data fusion strategy are applied together for decision-making. Details are provided in the following sections with examples from the experimental data.

In the last section of this chapter, the state space feature extraction method based on embedding is implemented separately. It is considered independently of the other features because only a preliminary study has been conducted on this topic with the purpose of presenting the idea and suggesting for future research efforts.

5.1 Temperature Compensation

During continuous structural health monitoring, the temperatures corresponding to the monitored signal and the baseline signal could be different. The temperature change would result in a waveform difference between the two signals, as discussed in Sec. 4.1. This waveform difference resulting from the temperature change must be compensated, so that differential features extracted from a signal-baseline combination reflect only structural changes. To do so, a set of baseline waveforms is acquired from the undamaged structure at a number of temperatures spanning the expected

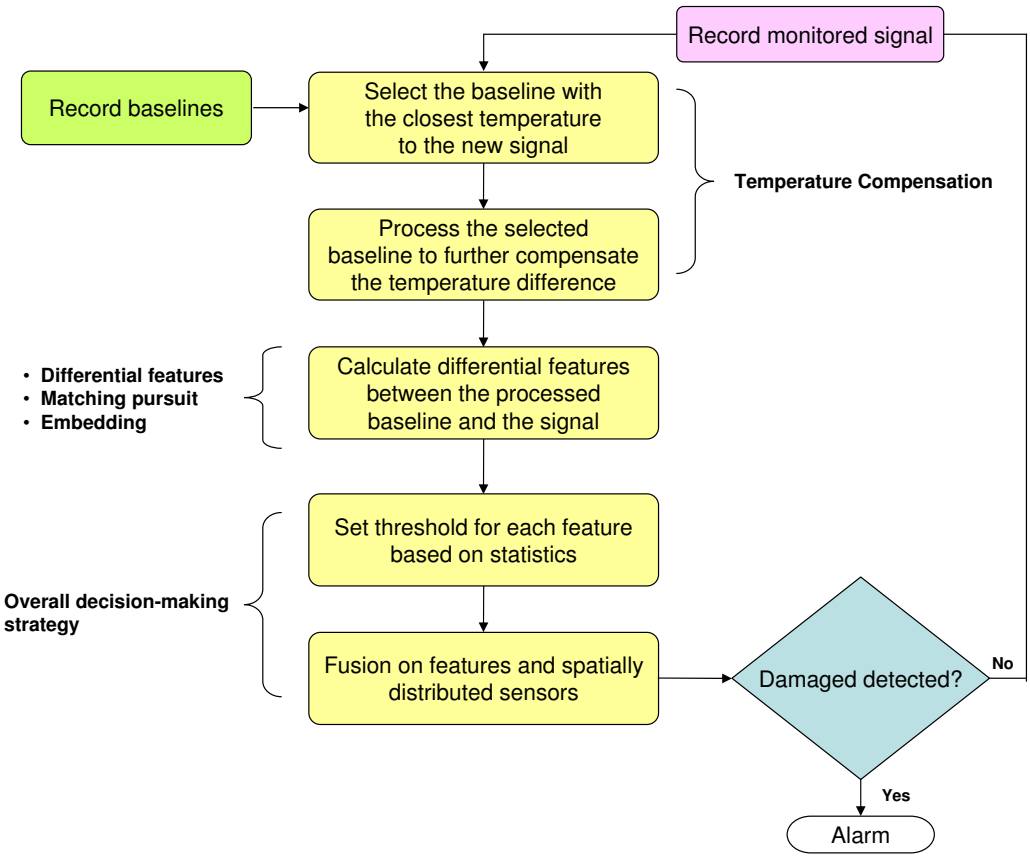

Figure 32: Integrated flowchart for damage detection.

service range. This baseline set is established by recording signals at roughly evenly spaced temperatures in the range of interest. Then, as originally reported by Lu and Michaels [83] and summarized here, each monitored signal is processed according to a two-step procedure: (1) selection of a waveform from the baseline set and (2) adjustment of this waveform to best match the monitored signal.

5.1.1 Baseline Selection

The goal of baseline selection is to identify a single waveform in the baseline set whose temperature is closest to that of the monitored signal. The presumption is that the baseline waveform whose shape most closely matches that of the monitored signal is the one whose temperature is also the closest match.

In [57], Michaels and Michaels proposed a direct subtraction method to quantify the match of diffuse ultrasonic waveforms. Consider a waveform $y(t)$ that is to be compared to a baseline waveform $x(t)$. Both waveforms are digitized at a sampling frequency F_s for a time window T to obtain sampled waveforms $x(n)$ and $y(n)$, both of length N. To eliminate the effects of amplitude differences, both waveforms are normalized in amplitude to obtain scaled waveforms $y'(n)$ and $x'(n)$. The monitored waveform $y(n)$ is normalized to unit energy:

$$y'(n) = \frac{y(n)}{\sqrt{\sum_{n=0}^{N-1} y^2(n)}}. \tag{43}$$

The baseline waveform $x(n)$ is scaled to minimize the mean squared error between it and the unity energy monitored signal $y'(n)$:

$$x'(n) = A \cdot x(n) \tag{44}$$

where

$$A = \frac{\sum_{n=0}^{N-1} x(n)y'(n)}{\sum_{n=0}^{N-1} x^2(n)}. \tag{45}$$

The normalized mean squared error MSE of the difference between the two scaled signals is calculated as

$$MSE = \sum_{n=0}^{N-1} [y'(n) - x'(n)]^2. \tag{46}$$

This mean square error measures how closely the shapes of the monitored signal and the baseline signal match. It is used here for the baseline selection.

As an illustration, a set of waveforms from the first experiment with temperatures ranging from 5 °C to 40 °C (1 °C increment, 36 waveforms total) is chosen as the baseline set. Two additional waveforms recorded from the undamaged specimen at

25 °C and 35 °C are taken to be the monitored signals. Mean square errors between the two signals and the baseline set are calculated. Figure 33 shows the results, where the abscissa is the temperature of the baseline waveform and the ordinate is the value of MSE calculated as per Eq. 46. It can be seen that the MSE achieves its minimum value for the baseline waveform whose temperature is closest to that of the monitored signal. Moreover, the MSE monotonically increases as the temperature difference increases, yielding a single global minimum that is essentially zero. The baseline waveform corresponding to the minimum error is selected as the best match to the monitored signal.

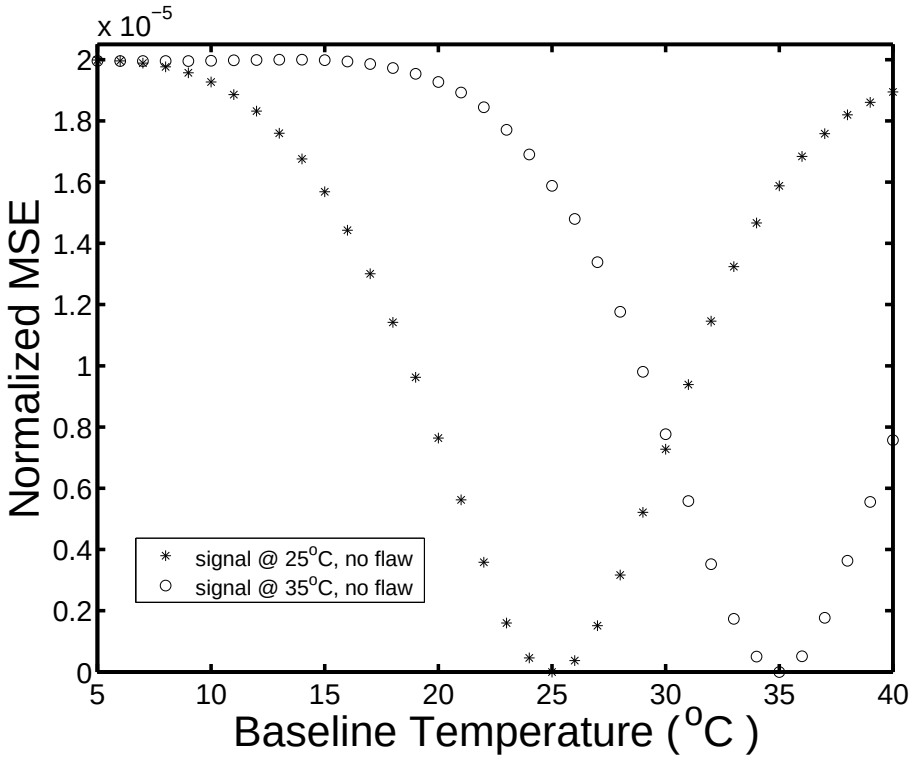

Figure 33: Normalized mean squared error as a function of the baseline temperature for waveforms from an undamaged specimen.

For the data shown in Fig. 33, the two monitored signals were recorded from an undamaged specimen. Next, the analysis is repeated using waveforms from the damaged specimen. Figure 34 shows the results of comparing two flaw waveforms to the same baseline set that was used in the previous example. The flaw is the

2.54 mm (0.10 in.) long notch introduced in the first experiment. For the signal at 25 °C, the MSE vs. baseline temperature curve has a unique minimum at the temperature closest to that of the monitored signal, although the minimum value does not drop to zero. For the signal at 35 °C, a unique minimum exists, but the corresponding baseline temperature is 36 °C, one degree away from that of the signal. This deviation is typical and can be attributed to the uncertainty of the temperature measurements.

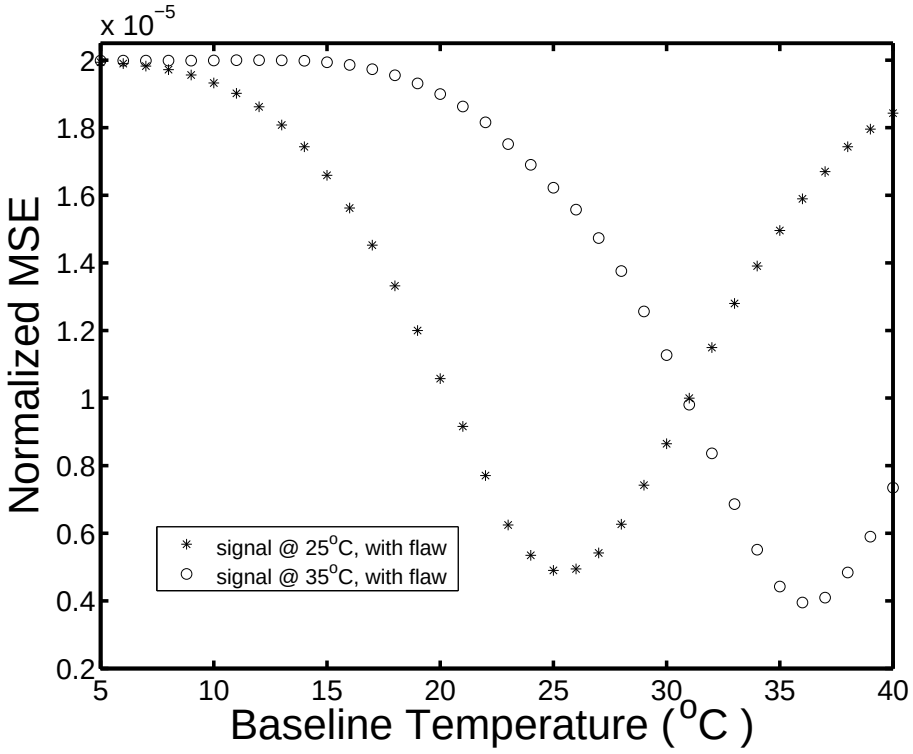

Figure 34: Normalized mean squared error as a function of the baseline temperature for waveforms from a damaged specimen (through-thickness notch, 2.54 mm in length).

These examples indicate that a monitored signal can be uniquely matched to a baseline waveform regardless of whether or not a flaw has been subsequently introduced. One can conclude that this behavior is reasonable and expected by considering the following points:

- After a flaw occurs, the ultrasonic field is still a diffuse wave field and thus the

theory of the temperature dependence of diffuse wave phase is still applicable.

- If the flaw is geometrically small compared to the structure, then its interaction with the diffuse ultrasonic wave field (and the recorded signal) should also be small, lending support to the idea that its effect on the shape of the MSE curve will be small.

- The waveform distortion resulting from the flaw is approximately the same for each error calculation and should contribute approximately the same amount to each value of MSE. Thus, the overall shape of the curve should not change significantly but will be offset from zero.

Based on the above points, we also expect the baseline selection method to be insensitive to the shape and location of a small flaw. The data recorded from the second experiment supports this expectation. In Fig. 35, two flaw waveforms from the specimen at 14.1 °C and 21.1 °C are compared to a set of non-flaw baseline waveforms. The flaw is a hole of diameter 4.76 mm (3/16 in.), and the temperatures of the non-flaw waveforms range from 8.9 °C to 37.8 °C with an increment of approximately 1.1 °C. In both cases, the MSE vs. temperature curve has a unique minimum corresponding to the baseline waveform recorded at the temperature closest to that of the flaw signal.

Since the purpose of baseline selection is to identify the baseline waveform closest in temperature to that of the monitored signal, neither the exact temperature of the selected baseline nor the accuracy of the temperature measurements of the baselines is critical. For example, in the first experiment, waveforms were recorded at temperatures from 5.0 °C to 40.0 °C at a 1.0 °C increment. All 36 waveforms could be used as the baseline set. Alternatively, a subset could be identified as the baseline set with temperatures that span the range of interest but with a larger spacing.

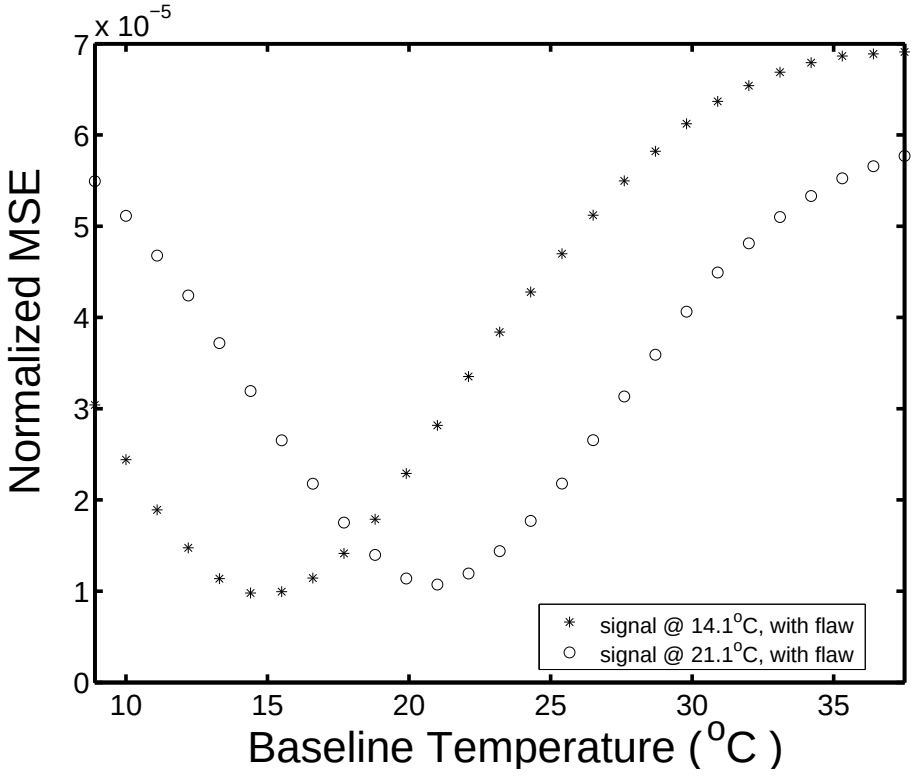

Figure 35: Normalized mean squared error as a function of the baseline temperature for waveforms from a damaged specimen (through-hole, 4.76 mm in diameter).

5.1.2 Baseline Correction

It is impractical for the baseline waveform set to continuously match every temperature within the expected range. The minimum temperature interval of the baseline waveforms is limited in practice by both waveform storage issues and the resolution of the temperature measurement; the preference is to use a small number of baseline waveforms covering the expected temperature range. Therefore, the temperature of the selected baseline waveform is, in many cases, different than the temperature of the monitored waveform, although the difference may be small if there are a large number of evenly spaced baseline waveforms. To adjust the selected baseline to best match the monitored signal; i.e., to best compensate for any temperature difference, the following three situations are considered: (1) temperature change and no flaw, (2) flaw and no temperature change, and (3) flaw and temperature change.

For the no-flaw situation, a temperature change mainly results in a linear waveform phase shift. Figure 36 shows the short time cross correlation results of comparing a baseline waveform at 25 °C to a non-flaw waveform at 30 °C. The top plot is time delay, $D_{xy}(t_c)$, vs. time window center as calculated by Eq. 3. The bottom plot is peak coherence vs. time window center, where the peak coherence $C_{xy}(t_c)$ is defined as [57]

$$C_{xy}(t_c) = \frac{\max_{\tau}\{|\hat{R}_{xy}(\tau, t_c)|\}}{\sqrt{\hat{R}_{xx}(0, t_c) \cdot \hat{R}_{yy}(0, t_c)}}. \tag{47}$$

Note that the peak coherence achieves its maximum value of unity only when the shapes of the two waveforms are identical; its minimum possible value is zero, which would be the case for completely uncorrelated signals.

From the time delay plot in Fig. 36, one can see that the waveform phase shifting pattern is linear with only slight deviations. In the peak coherence plot of Fig. 36, the peak coherence values are high (> 0.8) over the whole waveform interval, which implies that the difference between the two waveforms is mainly the phase shift.

The introduction of a flaw causes a change in the waveform that is reflected in both the phase shifting pattern and the waveform shape changes. Figure 37 shows the result of comparing a baseline waveform at 25 °C to a flaw waveform at 25 °C, where the flaw is the 1.27 mm (0.05 in.) long notch. In the top plot of Fig. 37, one can see that the phase shift is essentially zero for all times. In the bottom plot, peak coherence values are much smaller compared to the temperature-change-only case (Fig. 36). Clearly, changes in waveform shape result from the flaw and are dominant compared to the phase changes.

When both a flaw and a temperature change occur together, they will both affect the waveform. As already discussed (Figs. 36 and 37), the flaw will primarily affect the waveform shape and the temperature change will primarily affect the waveform phase. Figure 38 shows the results of comparing the baseline waveform at 25 °C

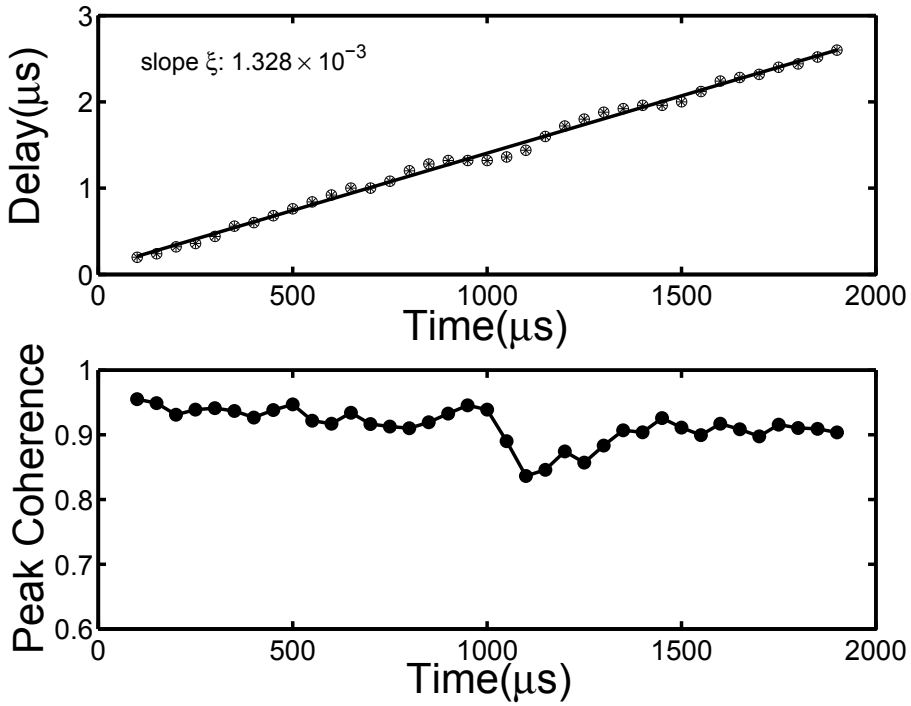

Figure 36: Time delay and peak coherence between waveforms recorded at 25 °C and 30 °C in an undamaged specimen.

to a flaw waveform at 30 °C, where the flaw is again the 1.27 mm (0.05 in.) long notch. In the time delay plot, although more deviation is observed compared to the temperature-change-only situation (Fig. 36), the linear phase shifting pattern resulting from the temperature change is clearly preserved. In the peak coherence plot, values are clearly reduced because of the flaw. The shape of the peak coherence curve is very similar to that of Fig. 37, indicating that the shape changes caused by the flaw are largely independent of temperature.

As predicted by theory and shown by example, a temperature change results in a linear phase shift and this phase shift is independent of the presence or absence of a flaw. Therefore, whether damaged or undamaged, the effect of a temperature difference on the mean squared error between the selected baseline and the monitored waveform can be minimized by stretching or compressing the baseline waveform according to its phase shift with respect to the monitored waveform. As discussed in

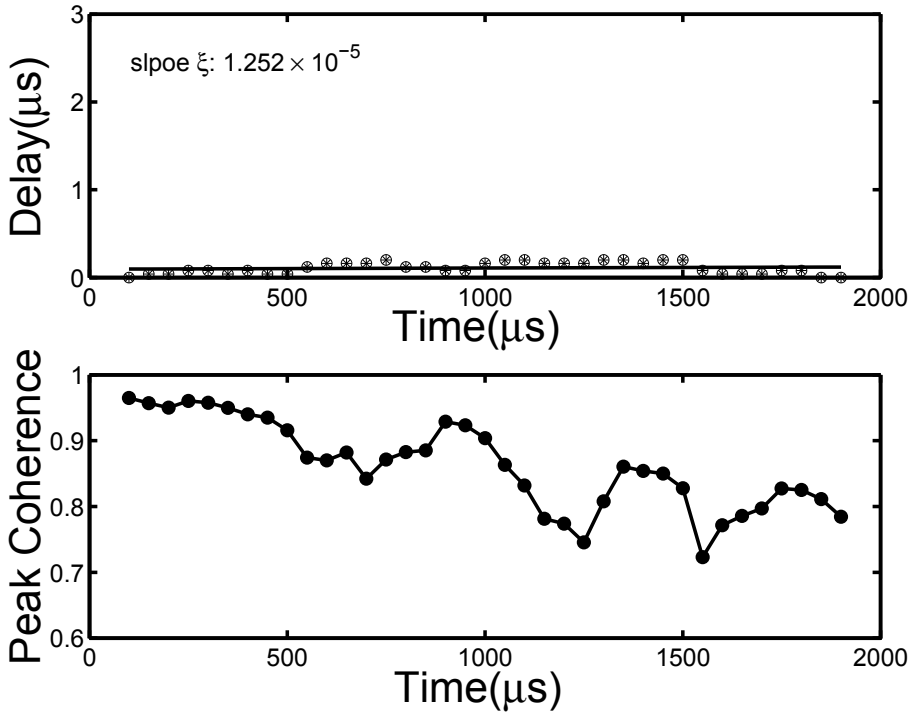

Figure 37: Time delay and peak coherence between waveforms recorded at 25 °C before and after introduced damage (notch, 1.27 mm in length).

Sec. 4.1, this phase shift is characterized by the slope ξ of the time delay as calculated from the short time cross correlation between the selected baseline and the monitored waveform. The baseline then can be stretched or compressed as per Eq. 4 so that the effect of the temperature difference is minimized.

If a flaw is present and if it is relatively large, outliers in the time delay curve may be observed which should be eliminated. In the top plot of Fig. 39, the time delay curve is shown for a flaw waveform at 30 °C with a 5.08 mm (0.20 in.) long notch compared to a baseline waveform at 25 °C. Outliers with large time delays exist, especially in the second half of the time window. At these later times, the corresponding ultrasonic path is longer and the wave is thus more likely to be affected by the flaw, resulting in more severe shape distortion. As the flaw becomes bigger, such distortion increases. When the shape is severely distorted, the time delay values obtained from the short time cross correlation do not give the correct phase shift

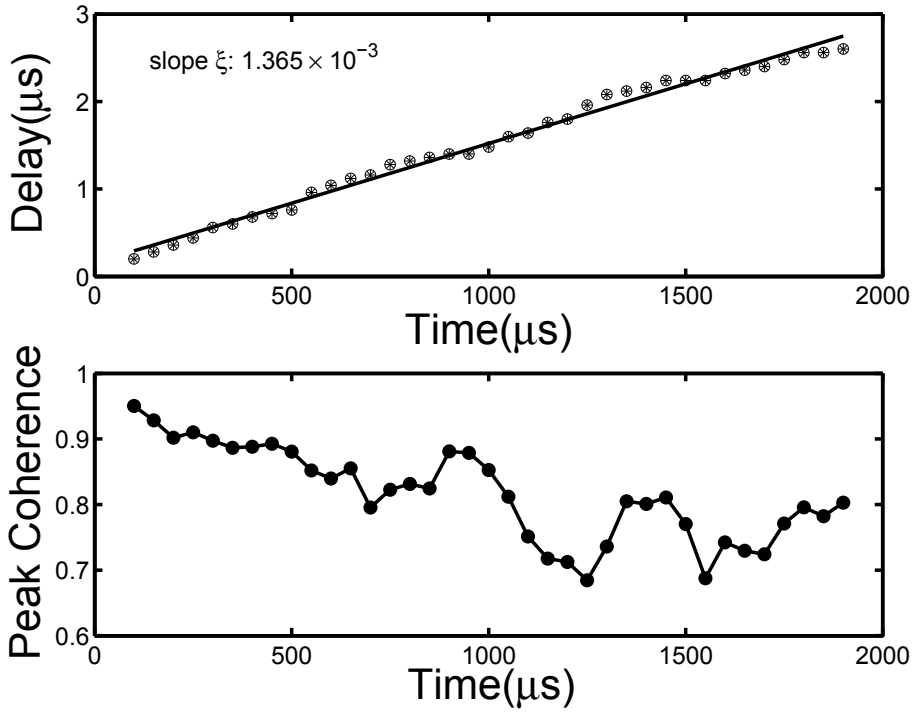

Figure 38: Time delay and peak coherence between waveforms recorded from an undamaged specimen at 25 °C and a damaged specimen at 30 °C (notch, 1.27 mm in length).

because, in these extreme cases, there is actually no phase relationship at all.

One way to compute the correct slope in the presence of outliers is to use time delay values from only the first half of the waveform where peak coherence values tend to be large. Another method is to set an upper limit for the time delay values that are used for calculating the slope. This limit can be obtained by cross correlating adjacent baseline waveforms to determine the largest possible time delay. For example, if the temperature interval of the baseline set is 5 °C, then the maximum time delay is approximately 3 μs (Fig. 36) and larger values should be rejected as outliers. In the proposed baseline correction method, these two methods are combined to eliminate outliers. In the bottom plot of Fig. 39, valid delay values are plotted, and the slope is calculated to be 1.890×10^{-3}.

The efficacy of this baseline correlation method is illustrated in Fig. 40 with the two signals shown in Fig. 12. The signal at 25 °C in Fig. 12 is used as a baseline, and

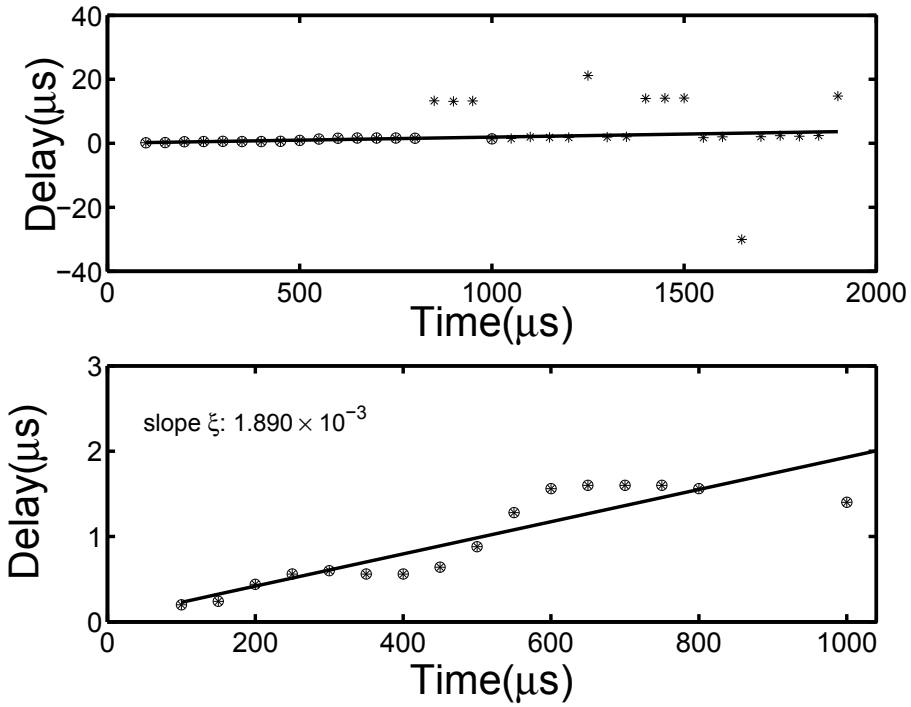

Figure 39: Example of outliers in the time delay curve calculated from the short time cross correlation.

the signal at 35 °C is viewed as a monitored signal. The direct MSE value between the baseline and the signal is 1.5877×10^{-5}. However, if using the baseline correlation method to adjust the baseline, the MSE value between the corrected baseline and the signal is reduced by a factor of about 2.5 to 0.6284×10^{-5}. In Fig. 40, the original baseline, the corrected baseline, and the monitored signal are plotted in two time intervals, and the waveform match between the baseline and the signal is much better after the baseline correction.

Based on a set of baselines spanning the temperature range of interest, the baseline selection method and the baseline correction method together provide a systematic compensation method for temperature variations.

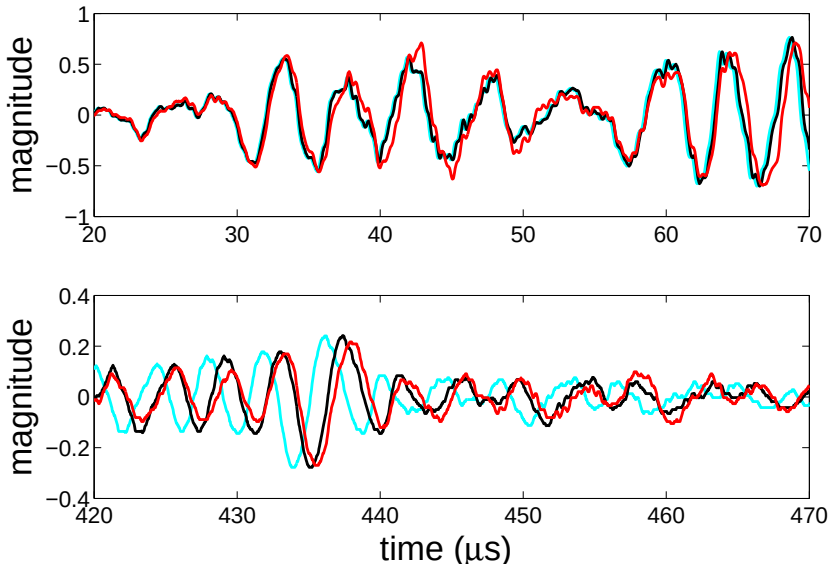

Figure 40: Example of the baseline correction method using signals of Fig. 12. The original baseline is at 25 °C. The monitored signal is at 35 °C. The upper plot shows the original baseline in cyan, the monitored signal in red, and the corrected baseline in black from 20 μs to 70 μs. The lower plot shows these waveforms from 420 μs to 470 μs.

5.2 Feature Extraction

For a monitored signal recorded at any temperature within the range of interest, a baseline is selected and corrected using the temperature compensation method introduced in the previous section so that the effect of the temperature difference between the signal and the baseline is minimized. Then, the next step is to extract features from comparing the baseline and the monitored signal. In this section, we select and compare several differential features with the consideration of discriminating benign surface condition changes and structural changes.

5.2.1 Basic Differential Features

Four basic differential features are selected which have been used in prior applications of ultrasonic damage detection [120, 73, 57]. They are called "basic" because they are relatively simple to calculate.

Normalized mean square error In Sec. 5.1.1, the normalized mean square error (MSE) is defined in Eqs. 44 to 46; it is a straightforward differential feature [73].

Loss of local coherence In Sec. 5.1.2, it is demonstrated that structural damage will cause changes in the shape of recorded diffuse ultrasonic waves. This distortion is quantified by the decrease of the peak coherence defined in Eq. 47. In [57], the authors propose a feature based on this observation. This feature is defined as the difference between the maximum and average values of the peak coherence, C_{xy},

$$P_{xy} = max[C_{xy}] - \bar{C}_{xy}. \tag{48}$$

An increase in P_{xy} means increased waveform shape changes compared to the baseline.

Loss of correlation The correlation coefficient indicates the overall match in waveform shape between two signals, and has been used as a basic differential feature for ultrasonic damage detection [121]. It can be expressed as,

$$\rho_{xy} = \frac{\int (x(t) - \mu_x) \cdot (y(t) - \mu_y) dt}{\sigma_x \sigma_y}, \tag{49}$$

where μ_x and μ_y are the mean values of the two signals, and σ_x and σ_y the standard deviations. To be consistent with other features in that a small feature value corresponds to a better waveform match, the feature used here is the loss of correlation [120],

$$LoC = 1 - \rho_{xy}. \tag{50}$$

Differential curve length Mathematically, curve length is used to measure the length of a smooth curve. If we consider a signal as a curve, then curve length is related to the complexity of the signal. Here, we calculate the differential curve length (DCL) of the residual signal $d(n)$ after subtracting the baseline from monitored signal. If two

sampled waveforms $x(n)$ and $y(n)$ are the baseline and monitored signals, respectively, and both are of length N, then, we have

$$d(n) = y(n) - x(n), \tag{51}$$

and

$$DCL = \sum_{1}^{N-1} \big|d(n) - d(n-1)\big|. \tag{52}$$

It should be noted that this definition is the not same as calculating the curve length of each signal and then subtracting the results.

5.2.2 Matching Pursuit Based Features

In Sec. 4.2, a numerical implementation method of matching pursuit decomposition is proposed and implemented for diffuse ultrasonic signals. Using the distributed and constrained matching pursuit decompositions, a baseline and a monitored signal are represented by their characteristic wavelets. In this section, several differential features are introduced based on the comparison of these wavelets.

5.2.2.1 Features for damage detection

To show the change of the characteristic wavelets due to damage, a baseline signal (25.0 °C of experiment #1) is decomposed using the distributed matching pursuit method with 30 iterations. Then, four monitored signals from experiment #1 are decomposed using the constrained method. The signals correspond to (1) 25.0 °C, no damage; (2) 30.0 °C, no damage; (3) 25.0 °C, 5.08 mm notch; (4) 30.0 °C, 5.08 mm notch.

Changes in the characteristic wavelets are shown graphically by plotting changes in times and amplitudes of the wavelets versus the times of the baseline wavelets $(u_m)_{m\in[1,30]}$, shown in Figs. 41 to 44. The change in time (in μs) is given by

$$\Delta u_m = (u'_m - u_m)_{m\in[1,30]}, \tag{53}$$

where u_m are the times of the baseline wavelets and u'_m are the times of the corresponding wavelets from the monitored signals (Sec. 4.2.3.2). The change in amplitude (in percent) is given by

$$\Delta A_m = ((A'_m - A_m)/A_m \times 100)_{m\in[1,30]}, \tag{54}$$

where A_m are the amplitudes of the baseline wavelets and A'_m are the amplitudes of the corresponding wavelets from the monitored signals (Sec. 4.2.3.2).

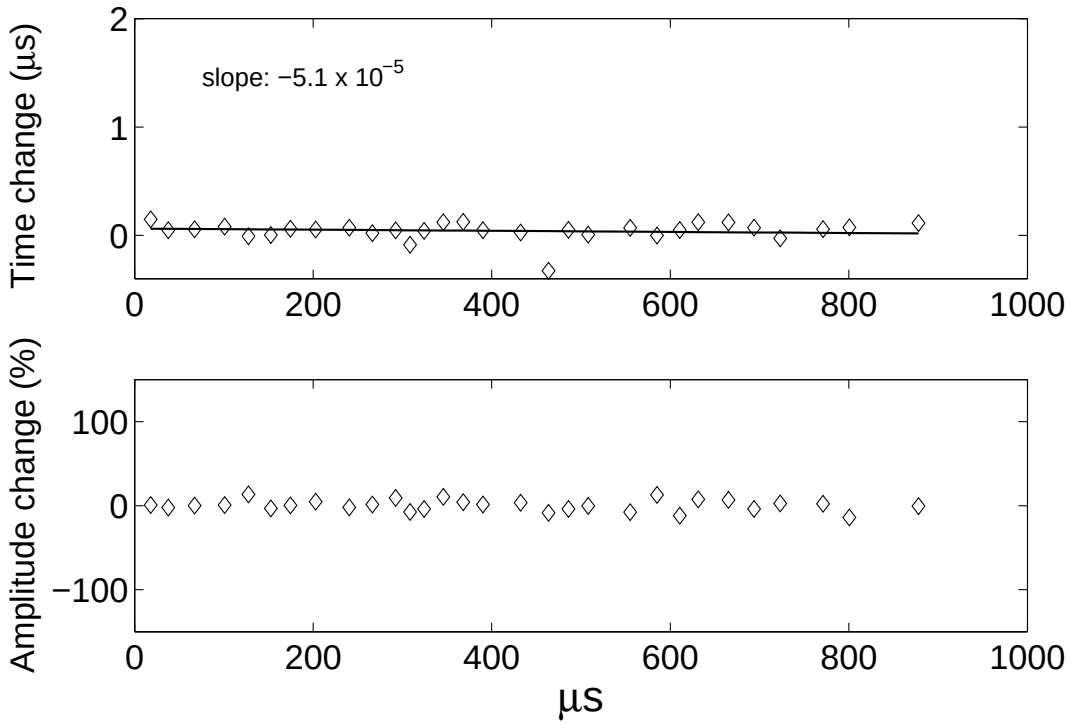

Figure 41: Time change and amplitude change of the characteristic wavelets between a baseline at 25.0 °C and an undamaged signal at 25.0 °C.

By comparing the upper plots of the four figures, one can see that the patterns of the time change of the characteristic wavelets are consistent with the results from the short time cross correlation (Figs. 36 to 39). These patterns capture the primary effect of temperature variations. The slope of the straight line fitting time changes as a function of time is analogous to the slope ξ, as shown in Figs. 36 to 39.

The effect of temperature variations is not strongly evident in the amplitude

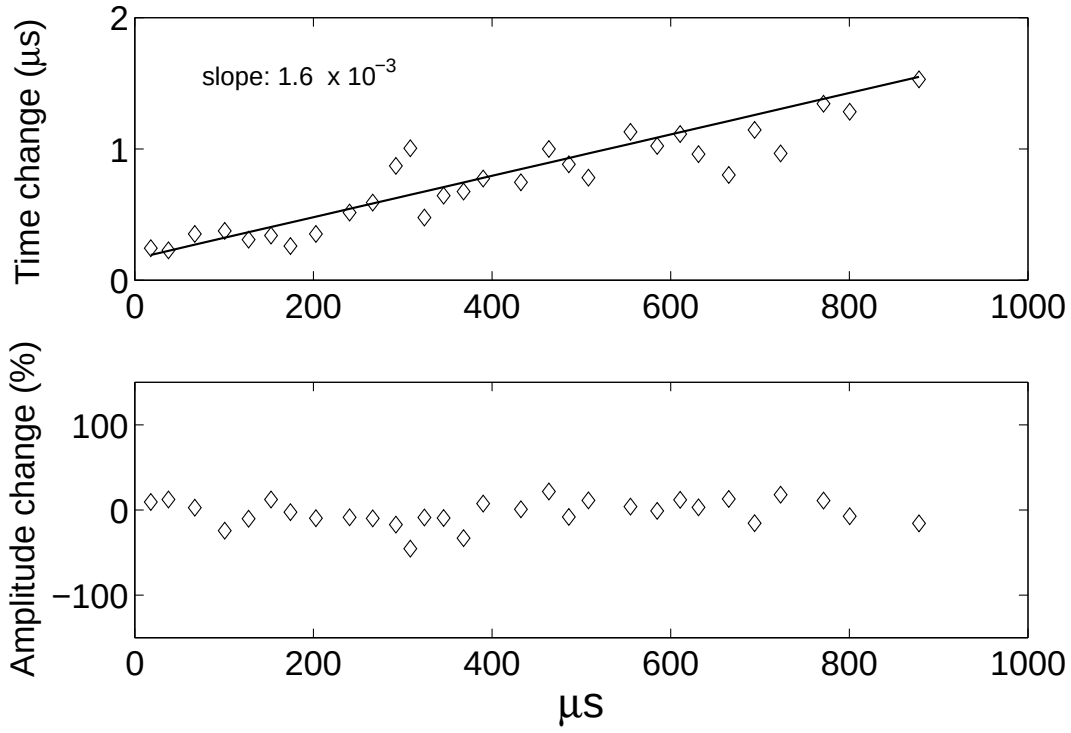

Figure 42: Time change and amplitude change of the characteristic wavelets between baseline at 25.0 °C and undamaged signal at 30.0 °C.

changes of the characteristic wavelets, as shown in the lower plots of Figs. 41 and 42. Instead, amplitude changes of the characteristic wavelets are more strongly correlated to damage. As seen in the lower plots of Figs. 43 and 44, introduction of a flaw causes increased amplitude changes. Based on this relationship between flaws and amplitude changes, two features are introduced.

Peak-to-Peak Amplitude Change

$$MP\_P2P = max(\Delta A_m) - min(\Delta A_m). \tag{55}$$

Standard Deviation of the Amplitude Change

$$MP\_STD = \frac{1}{M-1}\sum_{1}^{M}(\Delta A_m - \bar{\Delta} A_m)^2. \tag{56}$$

It should be noted that since the effect of temperature changes and the effect of

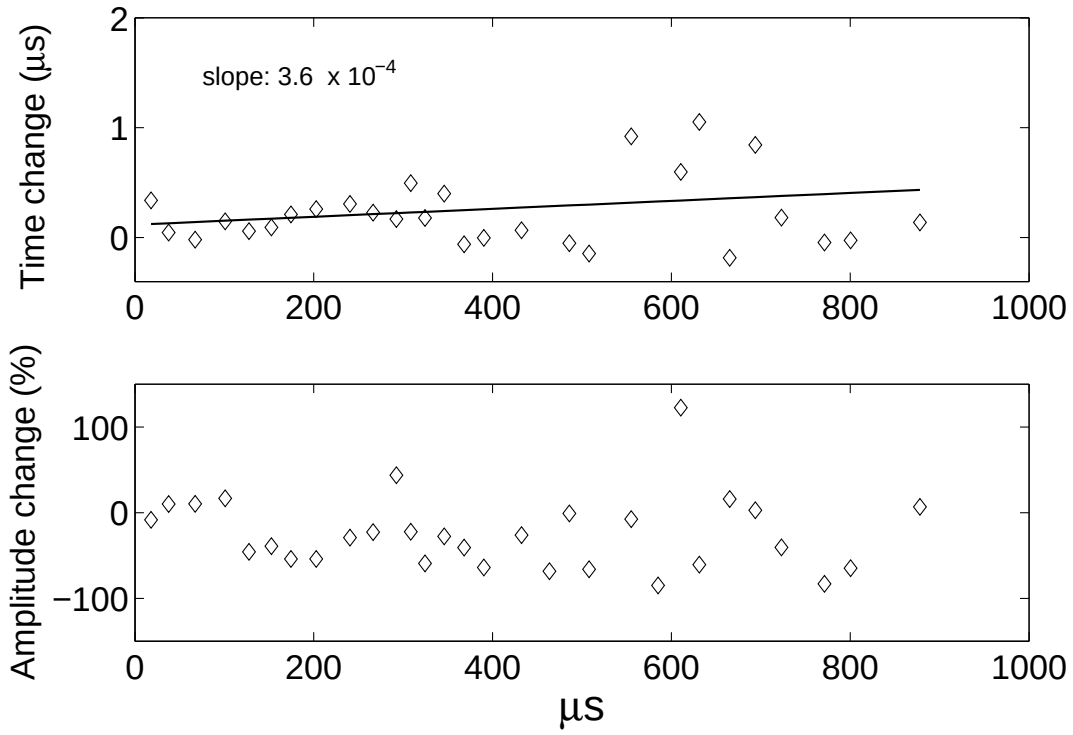

Figure 43: Time change and amplitude change of the characteristic wavelets between baseline at 25.0 °C and flaw signal at 25.0 °C (notch, 5.08 mm in length).

structural changes are captured separately by the time change and the amplitude change, features based on amplitude changes are inherently robust for temperature variations. This robustness is an additional advantage of the matching pursuit based features.

5.2.2.2 Feature sensitive to surface condition change

In experiment #3, controlled surface condition changes are applied to the specimen at each hole size. Based on the experimental data, a matching pursuit based feature is introduced which shows potential for discriminating the applied surface condition changes from damage.

Two recorded signals from experiment #3, one signal from surface wetting only and one flaw signal without wetting, are compared to the baseline using matching pursuit decomposition. The baseline is from the dry and undamaged specimen (signal

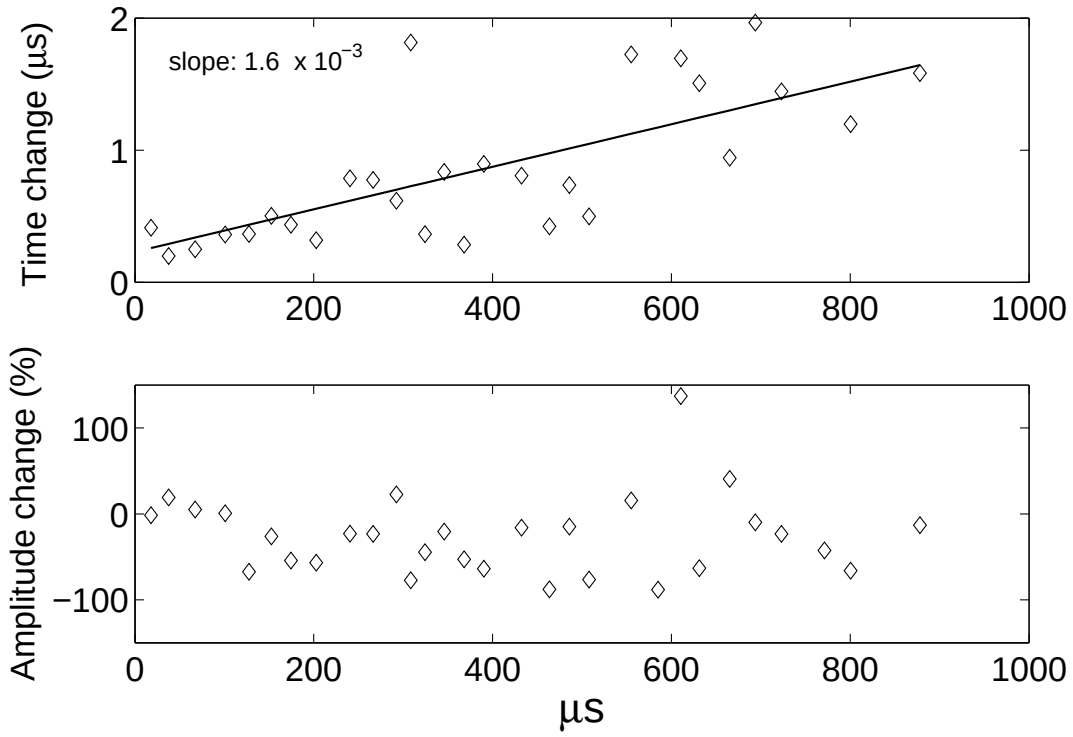

Figure 44: Time change and amplitude change of the characteristic wavelets between baseline at 25.0 °C and flaw signal at 30.0 °C (notch, 5.08 mm in length).

set $(0, 0)$ in Table 3), the signal from surface wetting is from the condition where the whole area determined by the O-ring is just covered by water (signal set $(13, 0)$ in Table 3), and the flaw signal is from the 6.0 mm diameter hole (signal set $(0, 11)$ in Table 3). All three signals are from transducer pair 1-2.

Fig. 45 shows the amplitude change ΔA_m versus the frequencies of the characteristic wavelets ($\xi'_m = \xi_m$) for the two signals (30 characteristic wavelets), where the upper plot is from the surface wetting signal and the lower from the flaw signal. The frequencies ($\xi'_m = \xi_m$) are sorted from low to high to investigate frequency dependence of the amplitude change.

The presumption here is that damage causes more changes in the higher frequency range than wetting. A simplistic justifying argument is that flaw dimensions are typically smaller than dimensions affected by wetting, resulting in higher frequencies (i.e.,

shorter wavelengths) being more sensitive to flaws than to wetting. This presumption is suggested by the results shown in Fig. 45, where the lower and higher frequency ranges are separated by a vertical line drawn between the 15th and the 16th frequency values; for each frequency range, the mean value of the amplitude changes is given and indicated by a horizontal line.

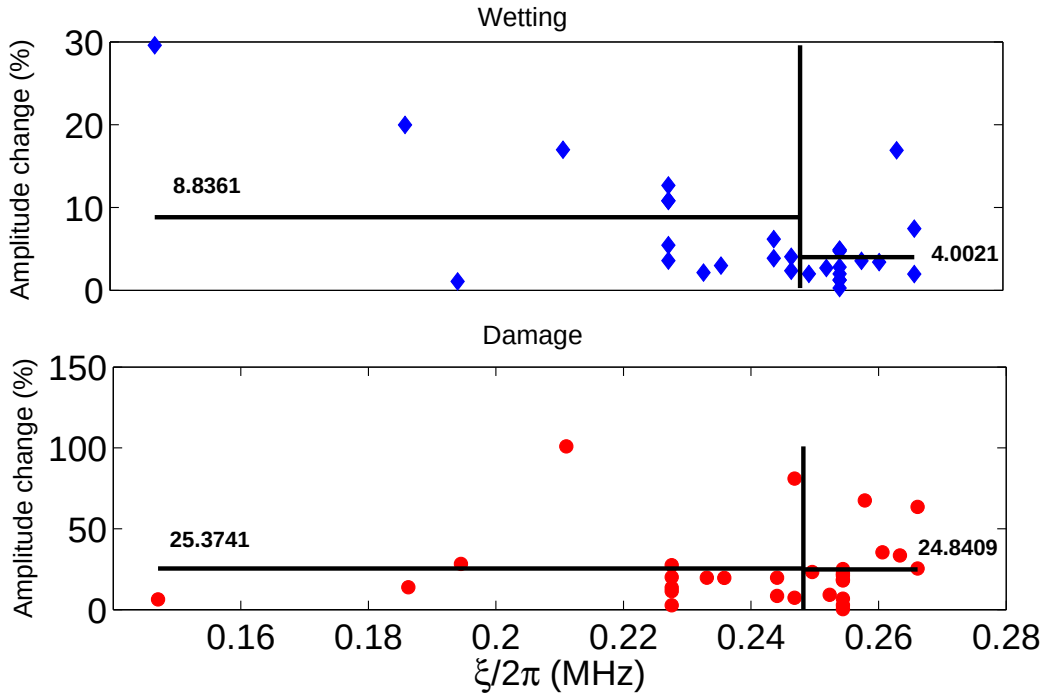

Figure 45: Amplitude change versus frequency. The upper plot is for the surface wetting signal recorded at the condition where the whole area of the O-ring is covered by water (signal set $(13, 0)$ in Table 3). The lower plot is for the flaw signal of 6.0 mm diameter hole (signal set $(0, 11)$ in Table 3). Both signals are from transducer pair 1-2. The vertical lines are located between the 15th and the 16th frequency values. The horizontal lines indicate the mean values of the amplitude changes.

Similar results are observed from signals of other transducer pairs. For example, Fig. 46 shows the decomposition results of signals recorded from transducer pair 1-4 at the same conditions as above. Based on these observations, a matching pursuit based feature is defined.

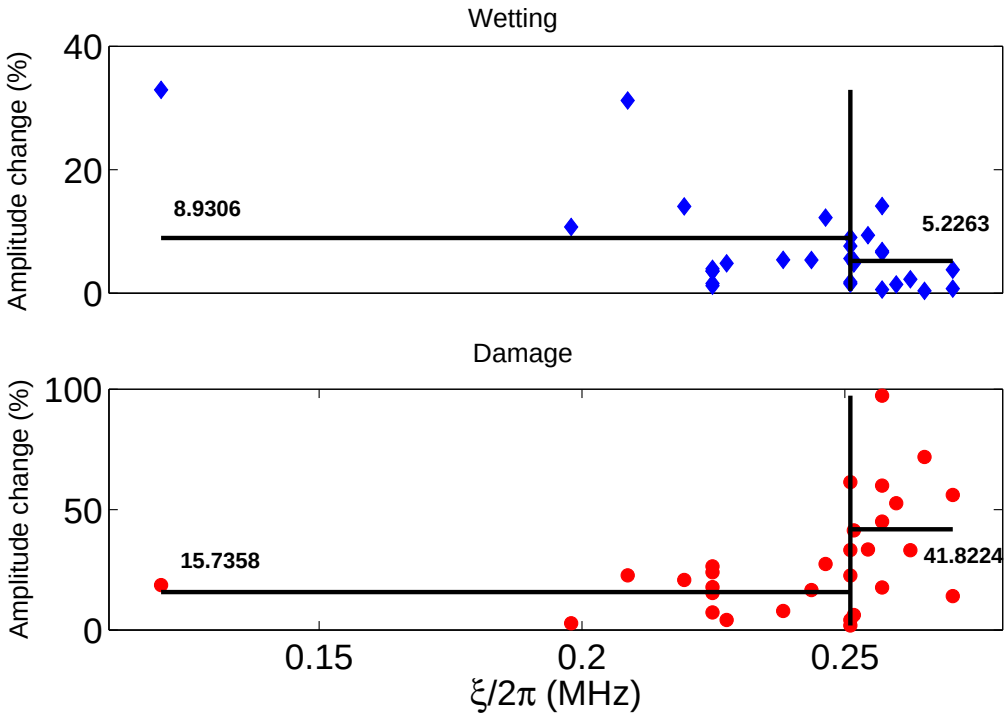

Figure 46: Amplitude change versus frequency. The upper plot is for the surface wetting signal recorded at the condition where the whole area of the O-ring is covered by water (signal set $(13, 0)$ in Table 3). The lower plot is for the flaw signal of 6.0 mm diameter hole (signal set $(0, 11)$ in Table 3). Both signals are from transducer pair 1-4. The vertical lines are located between the 15th and the 16th frequency values. The horizontal lines indicate the mean values of the amplitude changes.

Amplitude ratio (high frequency to low frequency)

$$MP\_Ratio = \frac{\sum_{k=M_c+1}^{M} |\Delta A_k|}{\sum_{k=1}^{M_c} |\Delta A_k|}, \tag{57}$$

where $\{\Delta A_k, k \in [1, M]\}$ is obtained by sorting the decomposition result $\{\Delta A_m, m \in [1, M]\}$ with respect to increasing frequencies ξ_m, and M_c is a parameter that can be adjusted to obtain different ratios.

In the work presented here, $M = 30$ and $M_c = 15$. The feature value is expected to be larger for structural damage than for surface wetting. Fig. 47 shows the feature values for a series of surface wetting and flaw signals, where all six transducer pairs are presented for a comparison. The flaw signals include all steps of the hole size with a clean surface condition (Table 3, sets $(0, 0)$ to $(0, 11)$, transducer pair 1-2). The surface

wetting signals include all steps of wetting without any structural changes (Table 3, sets $(0,0)$ to $(16,0)$, transducer pair 1-2). As shown in Fig. 47, the proposed feature is generally able to discriminate between surface wetting and structural change.

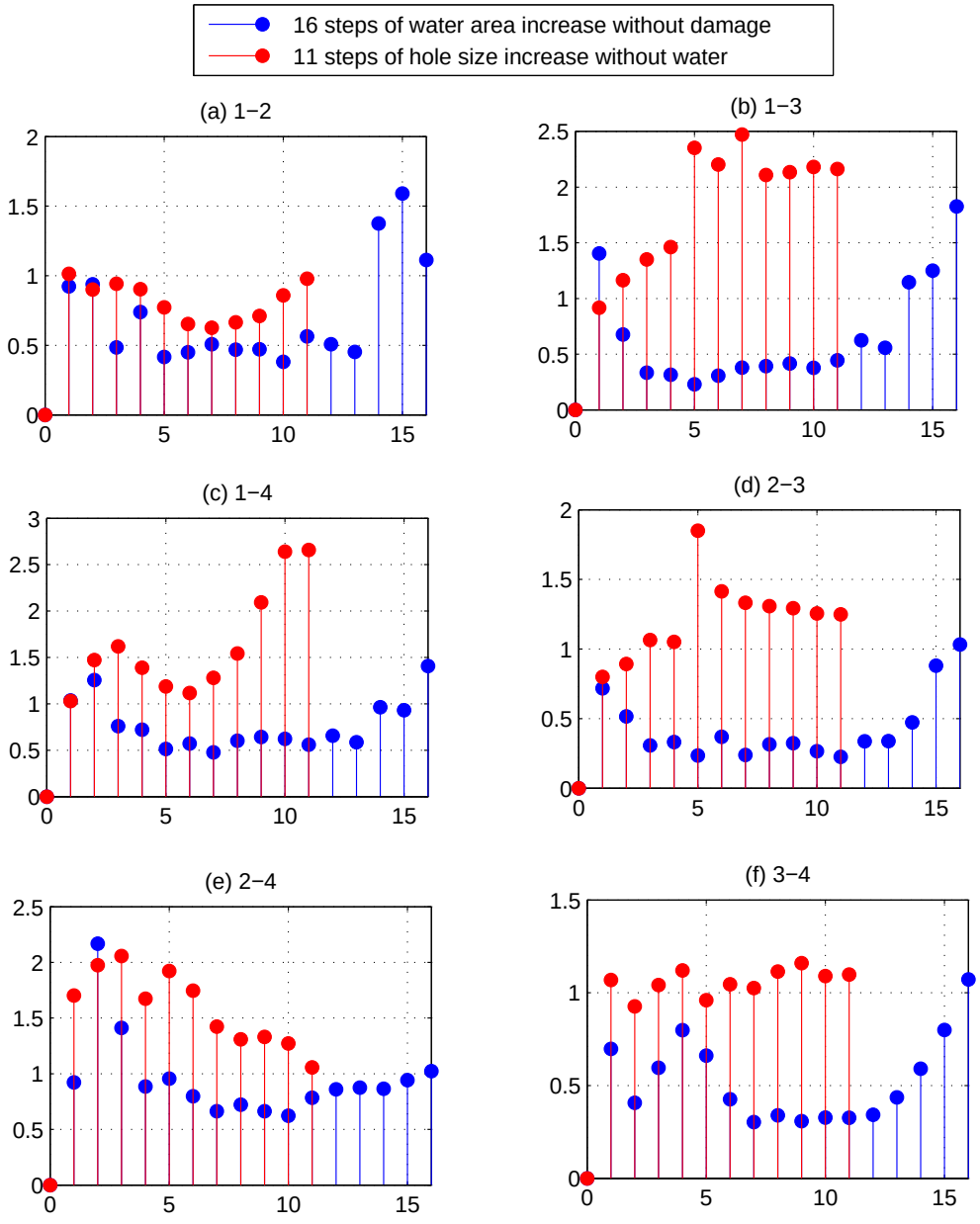

Figure 47: Feature *MP_Ratio* of signals from the experiment #3. For each transducer pair, surface wetting signals from sets $(0,0)$ to $(0,11)$ and structural change signals from sets $(0,0)$ to $(16,0)$ are compared.

5.2.3 Threshold Selection for Features

To determine the structural status based upon a single differential feature, a decision threshold for the feature is determined first. During the monitoring period, the new monitored signal is compared to the temperature compensated baseline, from which the differential feature is extracted. The feature value is then compared to the previously determined threshold. For the features defined in this thesis, large values are associated with increased damage, so if the value is above the threshold, the structure is classified as being damaged.

The threshold is selected based on the statistics of signals recorded under the undamaged condition. These signals include environmental changes and measurement variations, and represent the signals that would be recorded during an initial portion of the monitoring period prior to occurrence of damage. Comparing these signals to the baseline produces the statistical distribution of the value of the differential feature for the undamaged structural status. Based on the distribution, a threshold is determined by setting the probability of false alarm for the monitoring system.

Based on the threshold value, the probability of detection of a feature can be calculated. Similar to the procedure for determining the threshold, the statistical distribution of the value of the differential feature for the damaged structural status can be obtained by comparing all the flaw waveforms to the baseline. The probability of detection is then determined according to the distribution and the previously determined threshold. The relationship between the two distributions and the threshold is illustrated in Fig. 48, where f_0 is the distribution of the feature values for the undamaged condition, f_1 is the distribution for the damaged condition, and P_F and P_D stand for the probability of false alarm and the probability of detection, respectively.

As an example, for the signals of the surface wetting case in experiment #3, signal sets $(0, 0)$ to $(16, 0)$ in Table 3 can be used to determine the threshold; they are signals recorded at various surface wetting conditions before the introduction of damage.

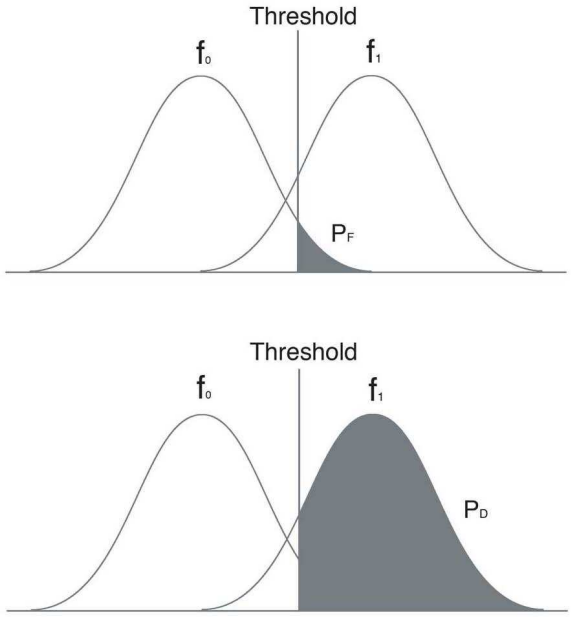

Figure 48: Threshold, probability of false alarm, and probability of detection

However, for this particular experiment, since the same surface wetting is repeatedly applied at every damage level, we can obtain more signals from the "undamaged" condition if for each damage level j ($j = 0 - 11$), signals corresponding to the clean surface condition (signal set $(0, j)$) are used as the baselines for the signals from damaged and wetting condition (signal sets $(i, j)_{i=0-16}$) to calculate features. This calculation is illustrated in Fig. 49, where the feature "Loss of Correlation" is used as an example. It can be seen from Fig. 49 that the wetting procedure is well controlled to have high repeatability. Feature values for wetting steps $14 - 16$ are much larger than others because in these steps, the whole area of the O-ring is covered by water and the water layer thickness has increased.

For the same data sets, if the signals from undamaged and clean surface condition (signal set $(0, 0)$) are used as the baselines, all of the other signals can be viewed as signals from monitoring. Using the feature "Loss of Correlation", Fig. 50 shows the results. In this case, the feature value increases as the hole size increases. Moreover,

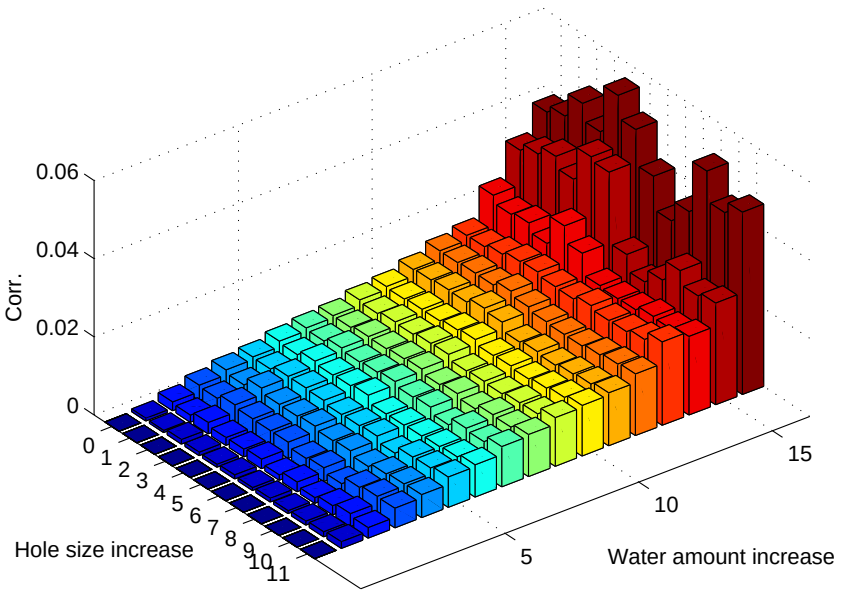

Figure 49: Values of the feature "Loss of Correlation" using signal sets $(0, i)_{i=0,11}$ as baselines. (Experiment #3, surface wetting, transducer pair 1-2). These values are used to determine the threshold based on a given false alarm.

the feature value only changes slightly according to the increase of surface wetting except in the last three steps where the water layer becomes thicker. This observation demonstrates the selectivity of the feature.

Using the above procedure, a threshold is selected based on a desired false alarm rate, and the corresponding probability of detection is then calculated. In Fig. 51, the data of Figs. 49 and 50 are represented by histograms. The vertical line shows a threshold as determined from the upper plot for a specific false alarm rate (percent of measurements to the right of the vertical line in the upper plot). The probability of detection is the percent of the measurements from the lower plot to the right of the vertical line.

The performance of a feature can be shown by the receiving operating characteristic (ROC) curve which is made by sweeping the threshold from high to low (which

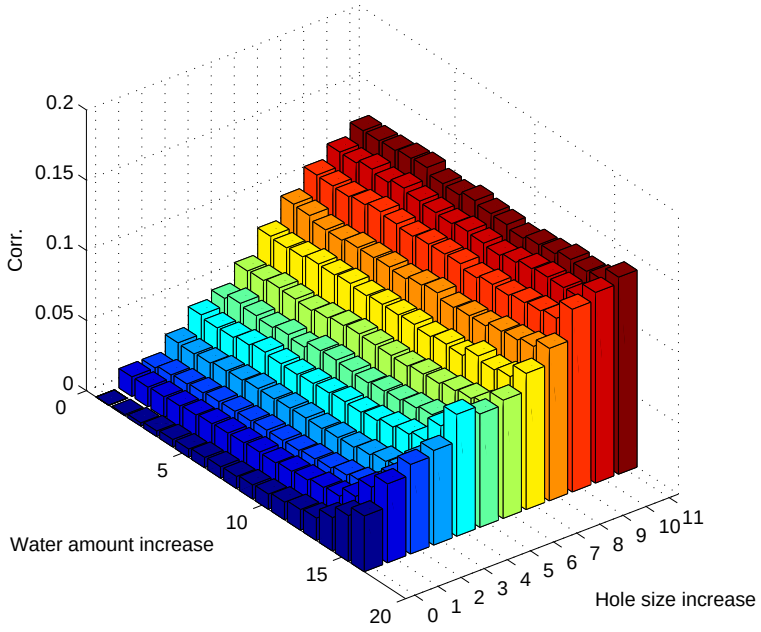

Figure 50: Values of the feature "Loss of Correlation" using signal set $(0, 0)$ as baselines. (Experiment #3, surface wetting, transducer pair 1-2). These values are used to calculate the probability of detection.

also sweeps the false alarm rate from 0 to 1) and calculating the corresponding probability of detection. The ROC curve for the feature "Loss of Correlation" is shown in Fig 52.

The ROC curve provides a statistical evaluation of the performance of a feature. For a specific working point on the curve, the size of flaw that is always detected is an important parameter, in addition to the false alarm rate and the probability of detection. For example, for the ROC curve of Fig 52, the probability of detection is 73.8% for a false alarm rate of 5%. At this point, the smallest hole size that is always detected is 3 mm, which means that the probability of detection is 100% for a 3 mm hole.

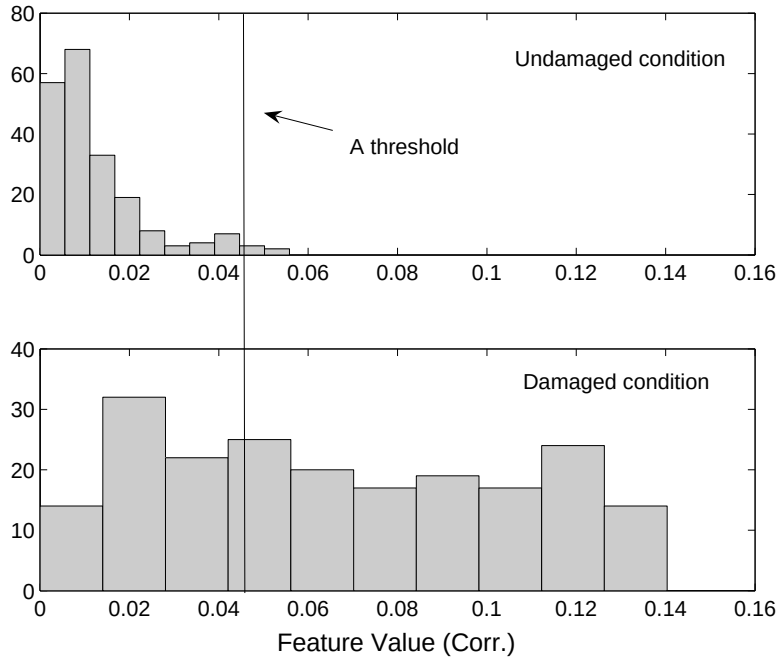

Figure 51: Histogram of the data shown in Figs. 49 and 50

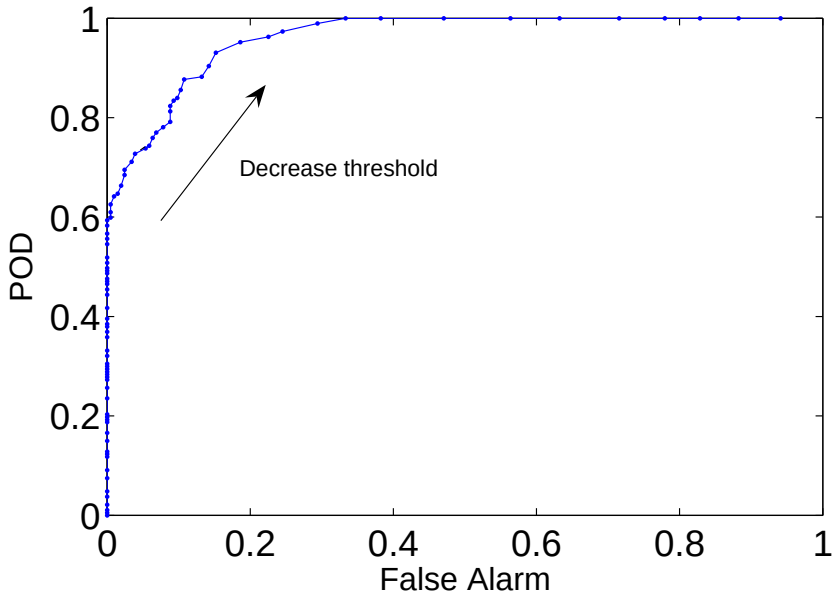

Figure 52: Receiving operating characteristic curve of feature "Loss of Correlation". (Experiment #3, surface wetting, transducer pair 1-2)

5.2.4 Comparison of the Features

In Secs. 5.2.1 and 5.2.2, seven features are proposed. Using the threshold selection method introduced in the previous section, the ROC curves of these features are

calculated for the data of experiment #3, from which the performances of the features for each transducer pair can be easily compared.

The ROC curves for the surface wetting case are shown in Fig. 53 for all six transducer pairs. As can be seen from the figure, features "MSE", "Loss of Correlation", and "Differential Curve Length" are the best three for all transducer pairs. The performance of the remaining four features varies for the different transducer pairs.

Figure 54 shows the ROC curves for the case of surface contact using brass bars, using the data sets listed in Table 4. Compared to the surface wetting case (Fig. 53), the first difference is that the performance for all features is not as good. This result is perhaps not surprising because the brass bar has a closer acoustic impedance to the aluminum specimen than water and the cross sectional dimensions are similar to those of the damage; thus, the ultrasonic response may be more similar to that caused by structural damage. The second difference is that although the basic features such as "MSE", "Loss of Correlation", and "Differential Curve Length" are generally the best, some matching pursuit based features are the best for some transducer pairs (i.e., "1-2", "2-3", and "3-4"). The third difference is that the feature "MP_Dratio" fails for transducer pair "1-2" and "2-3" (the ROC curve is below the diagonal). The feature "MP_Dratio" is defined based on the observations from the case of surface wetting, which are evidently not legitimate for surface contact with solids such as the brass bar.

From the comparison of these features, one can see that simple features such as "MSE" should always be considered first. Features extracted from advanced concepts can provide additional information, and the correlation of the feature to the physical meaning of the signal should be the basis for the extraction method.

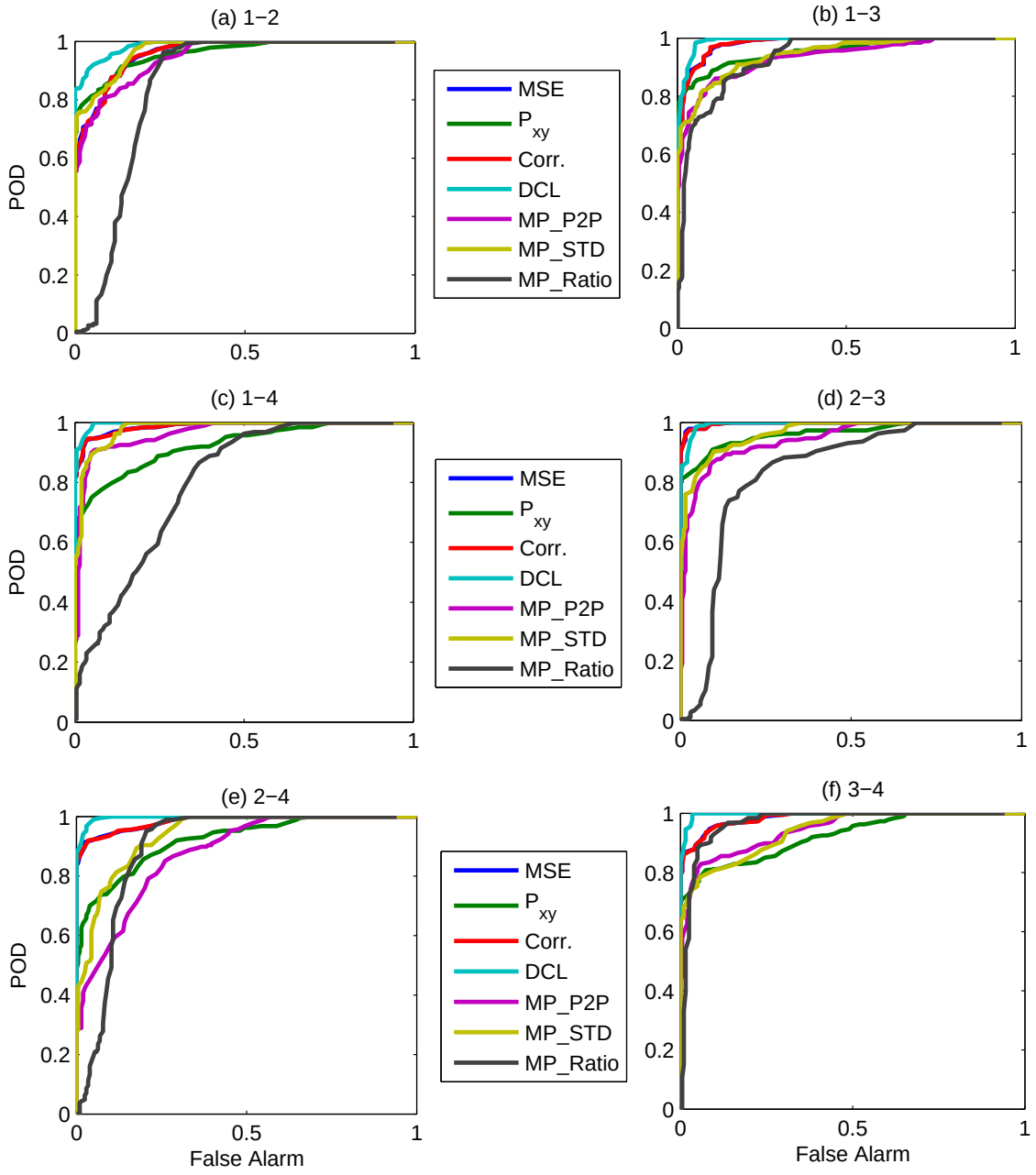

Figure 53: Receiving operating characteristic curves for all features and all transducer pairs. (Experiment #3, surface wetting case)

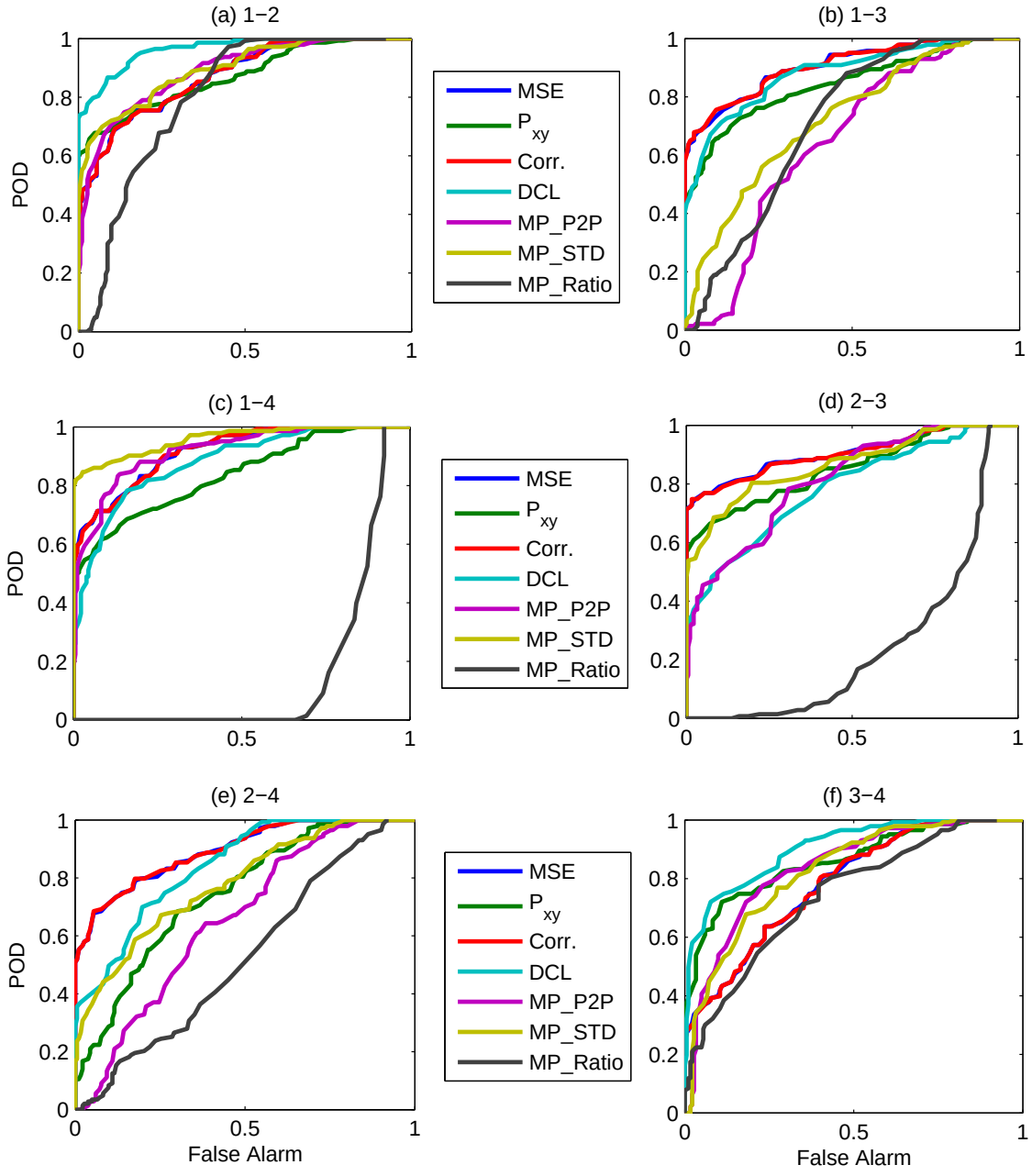

Figure 54: Receiving operating characteristic curves for all features and all transducer pairs. (Experiment #3, brass bar contact case)

5.3 Decision-Making Strategy

The last step in the procedure of the SHM system shown in Fig. 32 is the decision-making strategy; i.e., how to make a declaration of the structural status ("damaged"

vs. "undamaged") based upon multiple features extracted from a spatially distributed array of sensors (Experiment #3). The decision-making strategy falls into the general research area of data fusion [122, 123], and has been used in NDT&E to improve flaw detection [124, 125, 126].

The purpose of data fusion is to combine information from different sources to improve the classification performance. For a multi-sensor system, data fusion can be categorized into three levels [125]:

- Data-level fusion
- Feature-level fusion
- Decision-level fusion

Data-level fusion is also called low-level fusion. Raw data from commensurate sensors (i.e., the same type) are combined to produce new raw data that is expected to be more informative than that from a single sensor channel. Then, feature extraction and decision-making are conducted from the new raw data. However, it is usually difficult to fuse raw data measured in different forms or at different times, or from spatially distributed sensors [125].

Feature-level fusion is also known as intermediate level fusion. Features from different sensors or from the same sensor are fused to find the most relevant ones. Typical methods used in this level include principle component analysis, neural networks, and Bayesian methods.

Decision-level fusion is the highest level of data fusion. For a multi-sensor system, each sensor can provide an independent decision based on its own raw data and features. Then a fusion of these decisions can be processed through multiple methods, such as voting, Bayesian, or fuzzy logic.

In this thesis, a voting method at the decision-level is used for both feature and sensor fusion; data-level and feature-level fusion as defined in [125] are not used

here. The decision-making procedure is illustrated in Fig. 55, based on the sensor arrangement of experiment #3 and calculation of seven features.

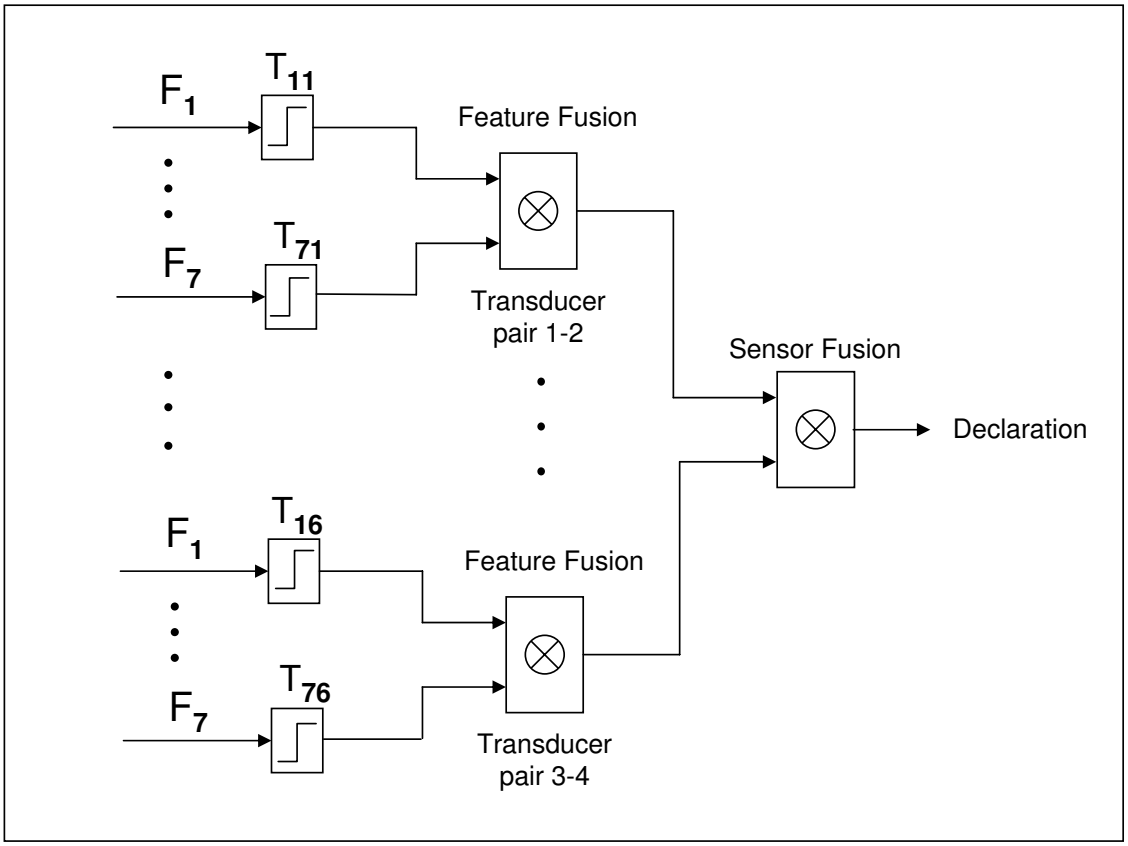

Figure 55: Feature and sensor fusion

The first step is to select a threshold for each feature from each transducer pair using a uniform false alarm rate. All seven features introduced in Secs. 5.2.1 and 5.2.2 are used. The resulting threshold values are different for different features and transducer pairs, and are labeled T_{ij} in Fig. 55. As new monitored signals become available from all transducer pairs, all the features are calculated and compared to their corresponding thresholds. This comparison leads to a binary declaration of each feature for each transducer pair in terms of "no damage" versus "damage". The false alarm rate used for threshold selection determines the credibility of each feature when

damage is declared; a low false alarm rate (a high threshold) means a high possibility that the damage declaration is correct and vice versa.

The next step is to fuse the feature declarations for each transducer pair using a voting scheme, which leads to a fused binary declaration for each transducer pair. A unanimous vote (7 of 7), a majority vote (4 of 7), an "OR" operation (1 of 7), or other numbers of votes can be used in this step. The voting method used in the feature-level fusion determines the credibility of each transducer pair declaration of damage, with a higher number of votes increasing the credibility.

The last step is to fuse the binary transducer pair declarations to reach an overall decision. In the same manner as for feature fusion, different voting schemes can be used.

Different false alarm rates for the threshold selection and different voting methods for the two fusion steps result in different outcomes. The rate and voting methods should be selected according to their interactive relationship. For example, one can use a very low false alarm rate to set the thresholds, so that the declaration for each feature has high credibility. Then one can use the 1 of 7 voting method in the following fusion steps to obtain a better probability of detection. The opposite extreme is to use a very high false alarm rate to maximize the probability of detection of each feature, and then limit the overall false alarm rate by using the unanimous voting method in the fusion steps. A compromise approach between these two extreme cases is to use a moderate false alarm rate combined with a majority voting method for data fusion. This approach is illustrated by the example below.

In Tables 5 and 6, the results of the decision-making strategy at each step are listed using the surface wetting data, where the preset false alarm is 5%, and the fusion method for both feature and sensor fusion is the majority voting method (4 of 7 votes for feature fusion; 4 of 6 votes for transducer pair fusion). The final probability of detection is 86.63% and the final false alarm rate is 2.94%. The smallest hole size

that is always detected is 2 mm after sensor fusion.

Table 5: Probability of detection with a preset false alarm rate of 5%.

Features	**Transducer Pairs**					
	1-2	1-3	1-4	2-3	2-4	3-4
MSE	0.733	0.888	0.947	0.979	0.920	0.893
P_{xy}	0.813	0.845	0.749	0.845	0.717	0.781
Corr.	0.738	0.893	0.947	0.979	0.925	0.893
DCL	0.920	0.941	0.979	0.984	0.989	1.000
MP_P2P	0.733	0.759	0.898	0.797	0.471	0.813
MP_STD	0.786	0.733	0.893	0.834	0.663	0.770
MP_Dratio	0.032	0.717	0.241	0.048	0.193	0.882

Table 6: Probability of detection, false alarm rate, and the size of the smallest hole always detected at the feature-level and sensor-level fusion using the majority voting method (4 of 7 votes for feature fusion; 4 of 6 votes for transducer pair fusion).

Feature	**Transducer Pairs**						**Sensor**
Fusion	1-2	1-3	1-4	2-3	2-4	3-4	**Fusion**
POD	0.759	0.877	0.893	0.877	0.856	0.898	0.866
FA	0.049	0.049	0.039	0.044	0.039	0.039	0.029
Min. hole diameter (mm)	2.5	3.5	2.0	2.5	3	2.5	2

To determine the best combination of the preset false alarm rate and the voting methods, a broad search is conducted. The preset false alarm rate for threshold setting is varied from 0% to 50% with a 1% step. For each false alarm rate, all seven voting methods for feature fusion (1 of 7 to 7 of 7) and all six voting methods for sensor fusion (1 of 6 to 6 of 6) are used. The total number of combinations of the preset false alarm rate and the voting methods is $51 \times 7 \times 6 = 2142$.

Fig. 56 shows the final probability of detection and false alarm rate for all combinations, where each point in the figure corresponds to one combination. Two points are circled in this figure, which are the two combinations whose outcomes fall in the region of POD > 0.95 and FA < 0.05. The details of these two combinations are listed in Table 7.

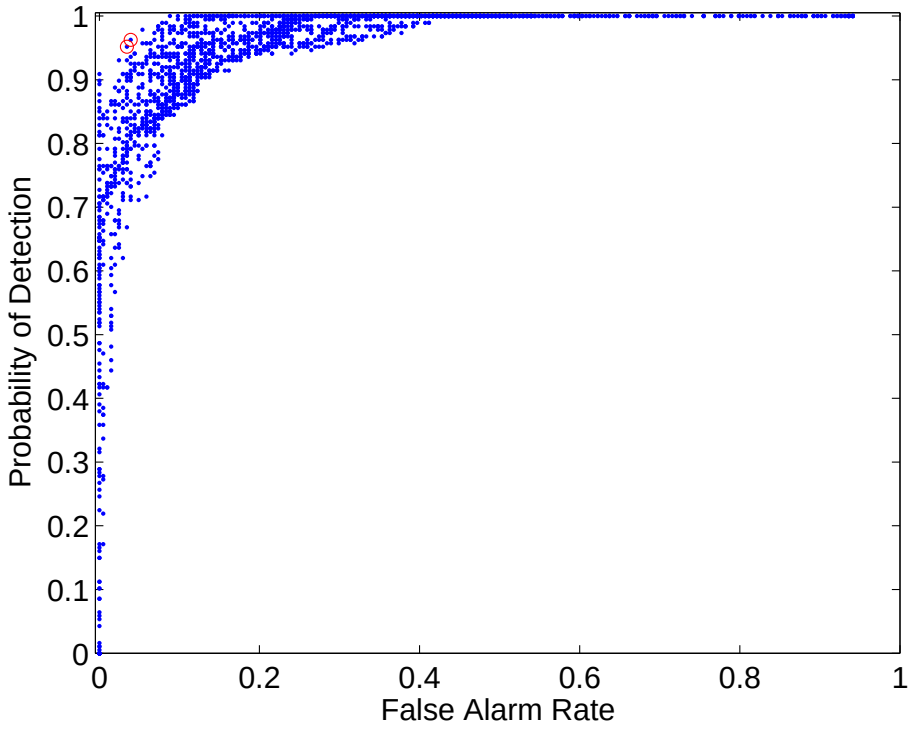

Figure 56: Final probability of detection and false alarm rate for various combinations of preset false alarm rate and voting methods. Two circled points correspond to two combinations whose outcomes fall in the region of POD > 0.95 and FA < 0.05.

The criterion for the best combination of the preset false alarm rate for threshold setting and the voting methods for feature and sensor fusion is balanced performance in terms of the final probability of detection, false alarm rate, and size of the smallest hole always detected. The two combinations shown in Table 7 are selected from all the others because their outcomes are the best in terms of the final probability of detection and false alarm rate. However, for the second combination in Table 7, the smallest hole that is always detected is 1.5 mm, which is one step better than 2.0 mm for the first combination. Therefore, in this work, a false alarm rate of 2% is preset for threshold setting, the 1 of 7 voting method is used for feature fusion, and the 3 of 6 voting method is used for transducer pair fusion.

Table 7: Detailed information of the two combinations whose overall outcomes fall in the region of POD > 0.95 and FA < 0.05.

Feature fusion	Sensor fusion	Preset FA	Overall POD	Overall FA	Min. Hole (mm)
1 of 7 votes	2 of 6 votes	1%	95.2%	3.4%	2
1 of 7 votes	3 of 6 votes	2%	96.3%	3.9%	1.5

5.4 Phase Space Feature Extraction

In Sec. 4.3, the theory of embedding and the simulation of chaotic excitation are introduced. A diffuse ultrasonic signal is convolved with a chaotic signal to simulate the response for a chaotic excitation, and the convolved signal is embedded into phase space to reconstruct the phase portrait.

In this section, a single differential feature for damage detection based on the phase portrait is described. The idea is to compare the phase portrait of a monitored signal to that of the baseline. The assumption is that more extensive damage results in a larger difference in the phase portrait.

Todd et al. [119] proposed a differential feature called nonlinear cross prediction error (NCPE). Nichols et al. [127] proposed another differential feature based on the cross recurrence plot of two phase portraits. Both features were applied to the data of experiments #1 and #2. The latter feature has much better performance and thus is introduced here. The same notation as in [127] is used here for consistency.

The recurrence plot of a given phase portrait X_n defined in Eq. 34 is the plot of its recurrence matrix, which is defined as

$$R_{ij} = \Theta(\epsilon - \|X_i - X_j\|), \tag{58}$$

where Θ is the Heaviside function and ϵ defines the threshold of the Euclidean distance between phase points X_i and X_j. If the distance between X_i and X_j is less than ϵ, the number 1 is assigned to R_{ij}; otherwise, 0 is assigned. Figure 57 shows the recurrence plot of a sine wave, the recurrence plot of the Lorenz attractor, and the recurrence

plot of the phase portrait reconstructed from a convolved diffuse ultrasonic signal.

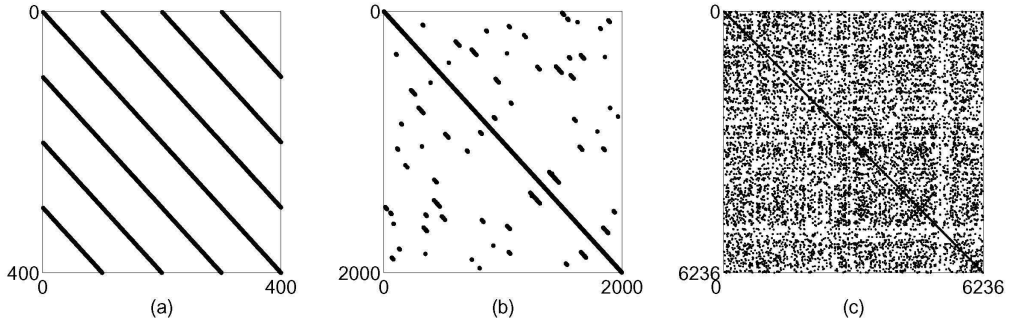

Figure 57: (a): Recurrence plot of a sine wave; (b): Recurrence plot of the Lorenz attractor; (c): Recurrence plot of the phase portrait reconstructed from a convolved diffuse ultrasonic signal.

In nonlinear time series analysis, the recurrence plot is used to unveil the deterministic property of a time series because the equation $R_{ij} = 1$ for $i \neq j$ indicates that two phase points of different time instances are neighbors in the state space, meaning that the signal repeats itself to some extent. The repetition of the signal is represented by the sub-diagonal lines in the recurrence plot. In Fig. 57, the recurrence plot of the sine wave has clear and long sub-diagonal lines because the sine wave is deterministic and periodic. The Lorenz attractor is also deterministic because it is the solution of a set of ordinary differential equations. However, its chaotic nature hides the deterministic property since the trajectory of the attractor never repeats itself but is only confined to a limited space. As a result, the recurrence plot of the Lorenz attractor consists of short sub-diagonal lines. The phase portrait reconstructed from the diffuse signal shows the weakest deterministic property among these examples. The reconstructed phase portrait is derived from the convolved signal that simulates the response to the Lorenz signal excitation. The response signal is expected to show more randomness than the excitation signal because it is formed after multiple reflections of the excitation signal from the boundaries of the specimen.

To compare two phase portraits using a recurrence plot, a modified recurrence

matrix is proposed in [127]. It is defined as

$$CR_{ij} = \Theta(\epsilon - \|X_i - Y_j\|), \tag{59}$$

where X and Y are the two phase portraits being compared. CR_{ij} is called the cross recurrence matrix. The diagonal and sub-diagonals in the corresponding cross recurrence plot reflect the similarity between two phase portraits, and this similarity can be roughly measured by the number of non-zeros in the cross recurrence plot; the less the similarity, the smaller the number of non-zeros and vice versa.

In Fig. 58, the left plot is the cross recurrence plot of a baseline signal and a flaw signal recorded in experiment #2; the right plot is the cross recurrence plot of the same baseline signal and another flaw signal from a larger flaw size. As per Eq. 59, a non-zero means that the i^{th} point of one phase portrait is close to the j^{th} point of the other, and is indicated by a dark dot in the cross recurrence plot. If two phase portraits are identical (or very close), the cross recurrence plot will thus have a dark diagonal, such as can be seen in Fig. 58. The number of non-zeros in the right plot is much less than that for the left plot, which means the shape of the phase portrait of the larger flaw size is less similar to that of the baseline compared to the smaller flaw size. Therefore, the growth of damage can be correlated to the shape change of the phase portrait as measured by the number of non-zeros in the cross recurrence plot. The number of non-zeros is typically normalized by the total number of elements in the recurrence plot [127]. It is defined as

$$\%recurrence = \frac{\sum\sum CR_{ij}}{N^2}, \tag{60}$$

where N is the number of the points of the phase portrait.

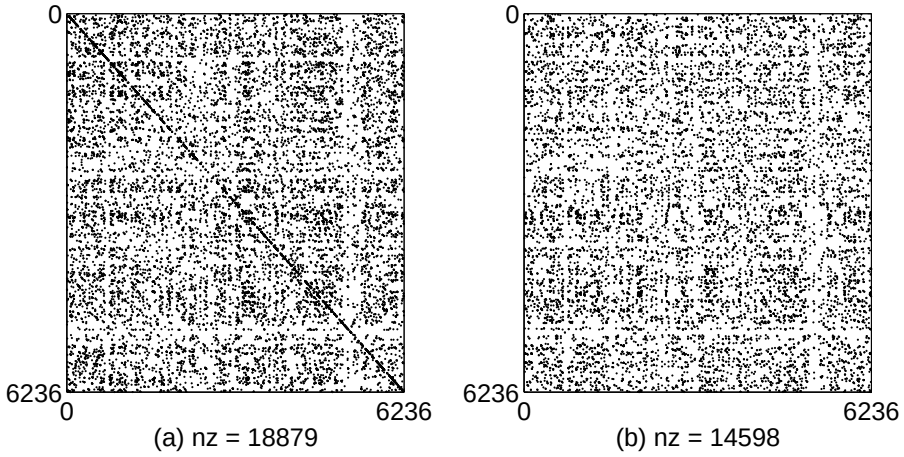

Figure 58: Cross recurrence plots: (a) Comparison of the flaw signal from the 5/64 in. diameter hole with the baseline; (b) Comparison of the flaw signal from the 1/4 in. diameter hole with the baseline

CHAPTER VI

EXPERIMENTAL RESULTS

In this chapter, the experimental results using the proposed methodology for damage detection introduced in Chapter V are reported. The first step of the methodology is a temperature compensation method which is based upon a set of baselines spanning the temperature range of interest. Here, the effectiveness of the size of the baseline set is evaluated using the temperature data from experiments #1 and #2.

Based upon the temperature compensated baselines, the next step of the methodology for damage detection is feature extraction and data fusion. In Chapter V, seven differential features are introduced, followed by the voting methods for feature and sensor fusion. In this chapter, the feature and sensor fusion methods are applied to the data of experiment #3, including the surface wetting case and the surface contact case. For experiments #1 and #2, because only one transducer pair is available, only feature fusion method is applied to the experimental data.

Finally, the phase space feature extraction method introduced in Chapter V is applied to the data of experiments #1 and #2, demonstrating the use of time series embedding for the analysis of diffuse ultrasonic waves.

6.1 Results of Temperature Compensation

The temperature compensation method proposed in Sec. 5.1 is based on a pre-recorded baseline set whose temperatures cover the expected range of service. In practice, a small number of baselines is generally preferred. Therefore, the effect of the size of the baseline set on the temperature compensation method is evaluated, as has been reported in [83].

This effect is evaluated by the concept of the probability of detection introduced

in Section 5.2.3, using the data from experiments #1 and #2. Signals from surface condition changes are excluded for this evaluation.

For experiment #1, 101 non-flaw waveforms were recorded (Table 1, excluding surface condition changes). The 36 waveforms recorded at each integer degree were chosen as the baseline set, and the remaining 65 non-flaw waveforms were used to determine the threshold of the differential feature for a desired probability of false alarm. For each of the 65 non-flaw waveforms, one baseline waveform was selected from the baseline set and then stretched or compressed, using the proposed baseline selection and correction methods. Then, a differential feature was extracted from the non-flaw waveform and the processed baseline waveform; the mean squared error (MSE) is used as an example. By comparing all the non-flaw waveforms to the baseline set, a set of values for MSE was obtained that was representative of the statistics of MSE for the undamaged structure. The distribution of those MSE values was then shown in a histogram, as plotted in Fig. 59. As is common, the probability of false alarm was set to be less than 5%, resulting in a threshold of 5.68×10^{-7} and yielding an actual probability of false alarm of 4.6% (3 false alarms out of 65 signals).

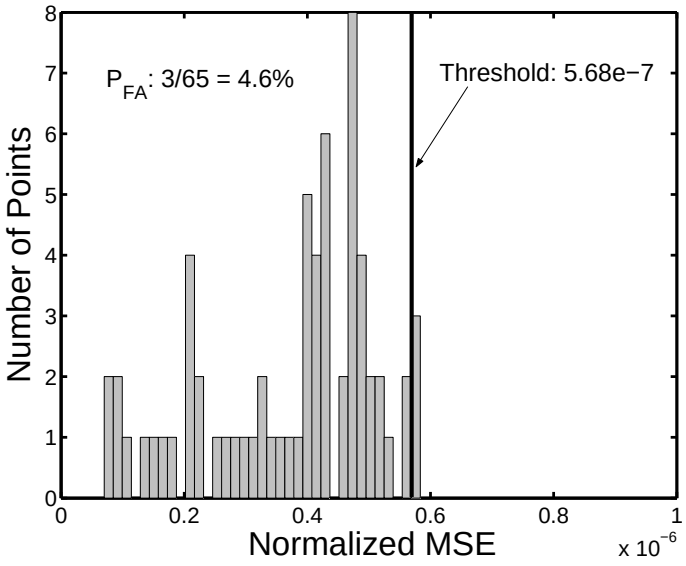

Figure 59: Histogram of the normalized mean squared error calculated from 65 waveforms recorded from the undamaged specimen (Experiment #1, 36 baselines).

To determine the probability of detection, the distribution for the damaged structure must be obtained. In experiment #1, 397 flaw waveforms were recorded at various temperatures. The histogram of their MSE values after comparison to the baseline set of 36 waveforms is shown in Fig. 60. By using the threshold value shown in Fig. 59, four flaw waveforms were classified as non-flaw, resulting in a probability of detection of 99%. The performance can also be measured in terms of the smallest flaw that was consistently detected; for this case, it was the notch of length 1.27 mm (0.05 in.); only the smallest notch (0.64 mm, 0.025 in.) was missed.

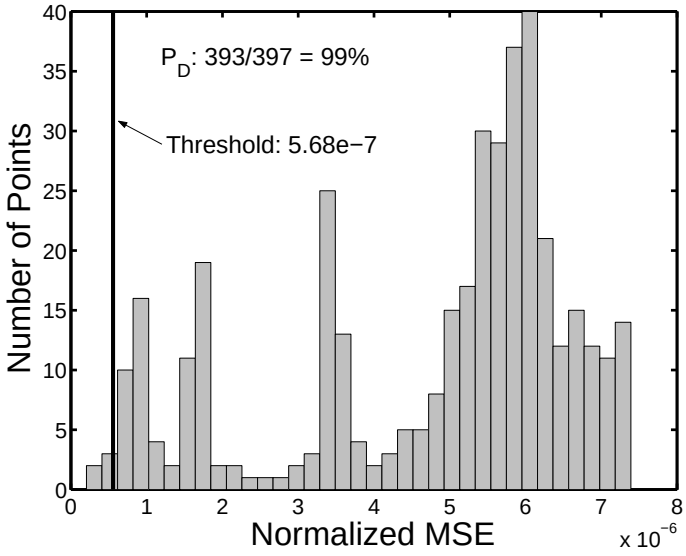

Figure 60: Histogram of the normalized mean squared error calculated from 397 waveforms recorded from the damaged specimen (Experiment #1, 36 baselines).

Besides the baseline set of 36 waveforms, four additional baseline sets with fewer baseline waveforms were used to evaluate performance with a sparse baseline set. The number of baseline waveforms considered were eight, six, four and three. The waveforms used in these sparse baseline sets were chosen from the above 36 baselines to cover the entire temperature range. In each case, after determining the threshold for a probability of false alarm no bigger than 5%, all 397 flaw waveforms were processed to determine the probability of detection.

Table 8 summarizes the results for all five cases. As shown in this table, the probability of detection decreased and the minimum size of the detected flaw increased as the number of the baseline waveform decreased. The probability of detection dropped to 62.2% when only three baselines were used. The decrease in the detection rate is attributed to the waveform distortion resulting from large temperature differences between the baseline and the non-flaw waveforms [79]. Fig. 61 compares the distortions of non-flaw waveforms with small and large temperature differences as measured by the peak coherence. One can see that with a large temperature difference, the severity of the distortion is comparable to that caused by a flaw (Fig. 37). Since for the sparse baseline case, temperature differences between the monitored signal and the baseline can be large, severe shape distortion can occur due to temperature alone and cannot be discriminated from distortion resulting from a flaw. As a result, the probability of detection decreases as the baseline set becomes more sparse. Therefore, waveform distortion due to temperature limits the probability of detection given a specific baseline waveform set.

Table 8: Damage detection performance for experiment #1.

No. of Baseline Waveforms	**Baseline Temperatures (°C)**	P_{FA}	P_D	**Min. Length Notch Detected (mm)**	**Threshold**
36	$5, 6, 7 \cdots 38, 39, 40$	4.6%	99.0%	1.27	5.68×10^{-7}
8	$5, 10, 15, 20, 25, 30, 35, 40$	4.6%	96.3%	1.27	9.30×10^{-7}
6	$5, 12, 19, 26, 33, 40$	4.6%	93.7%	1.27	1.45×10^{-6}
4	$5, 16, 28, 40$	4.6%	85.0%	1.90	3.23×10^{-6}
3	$5, 22, 40$	4.6%	62.2%	2.54	4.60×10^{-6}

For experiment #2, five different baseline sets were used for comparison. They consisted of 27, 4, 3, 2, and 1 baseline(s), respectively. Table 9 summaries the results. Perfect detection was achieved when using 27 and 4 baselines, and the probability of detection was bigger than 85% with only two baselines. The most likely explanation for the better performance in the second experiment compared to the first is that the smallest flaw size in the second experiment was larger than in the first.

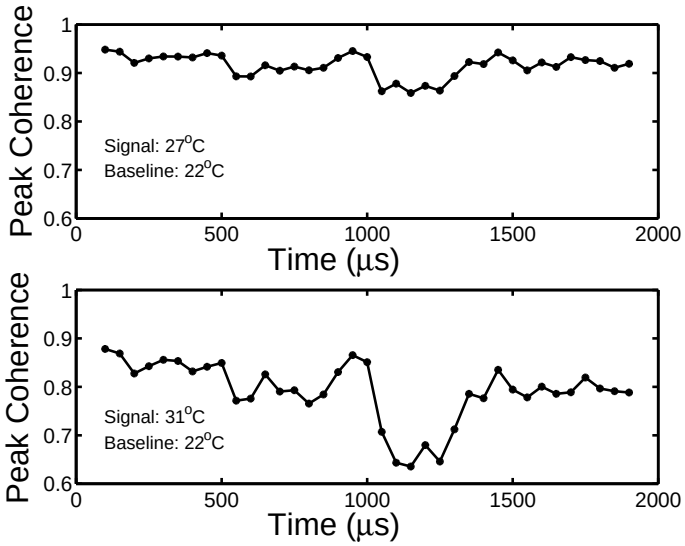

Figure 61: Illustration of waveform distortion caused by small (top) and large (bottom) temperature differences as measured by the peak coherence.

Table 9: Damage detection performance for experiment #2.

No. of Baseline Waveforms	Baseline Temperatures (°C)	P_{FA}	P_D	Min. Diameter Hole Detected (mm)	Threshold
27	$8.9, 10.0, 11.1 \cdots 37.8$	0%	100%	1.98	1.24×10^{-6}
4	$13.3, 20.0, 26.6, 33.3$	4.1%	100%	1.98	3.50×10^{-6}
3	$14.4, 23.3, 32.2$	5.0%	92.5%	3.18	4.18×10^{-6}
2	$16.7, 31.1$	5.0%	85.0%	3.57	7.50×10^{-6}
1	23.3	5.0%	52.5%	5.56	1.41×10^{-5}

The major advantage of the proposed methodology is that it provides a generic SHM method that systematically addresses the effect of temperature changes on diffuse ultrasonic waves. Furthermore, temperature measurements during monitoring are not required. For the establishment of a set of baselines, two methods are possible. One method is to record a set of baselines evenly spanning the temperature range of interest using temperature measurements. With the known temperatures of the baselines, the temperature compensation method is able to estimate the temperature of a monitored signal within the accuracy determined by the baseline set. The other method is to record a group of baselines without temperature measurement during the early service period of a structure where the environmental temperature

is assumed to vary and the structure is assumed to be damage free. By comparing the recorded baselines using short time cross correlation, a set of baselines with temperatures evenly spanning the whole temperature range can be selected according to the slope of the time delay vs. time curve (Eq. 19 and Fig. 16).

6.2 Results of Data Fusion

The decision-making strategy introduced in Sec. 5.3 shows that data fusion of different features and sensors can improve the overall performance of an SHM system. Here, this decision-making strategy is applied to the data from the three experiments. For experiment #3, the best combination of the preset false alarm rate and the voting methods for feature and sensor fusion chosen in Sec. 5.3 is applied. For experiments #1 and #2, sensor fusion is not available because there is only one transducer pair for these two experiments. Consequently, four representative decision-making strategies consisting of different preset false alarm rates for threshold selection and different voting methods for feature fusion are applied and compared.

6.2.1 Feature and Sensor Fusion for Experiment #3

For experiment #3 (surface condition change), both feature and sensor fusion can be applied since there are four transducers on the specimen (six transducer pairs). By the comparison of various fusion methods in Sec. 5.3, a 2% preset false alarm rate for each feature, combined with the 1 of 7 voting method for feature fusion and 3 of 6 voting method for sensor fusion is chosen. Using this decision-making strategy, the data fusion results for the surface wetting case and the case of surface contact using brass bars are calculated. Tables 10 and 11 list the results for the surface wetting case.

As shown in the tables, all seven features defined in Sec. 5.2 are used. Although some features have better individual performances than the others (Figs. 53 and 54), all of them are used since the purpose here is to demonstrate the efficacy of data

Table 10: POD for each feature and transducer pair with the preset false alarm rate of 2% (Experiment #3, surface wetting case).

Features	**Transducer Pairs**					
	1-2	1-3	1-4	2-3	2-4	3-4
MSE	0.679	0.818	0.872	0.979	0.914	0.866
P_{xy}	0.781	0.808	0.701	0.818	0.642	0.717
Corr.	0.663	0.818	0.877	0.973	0.893	0.861
DCL	0.850	0.850	0.947	0.888	0.941	0.952
MP_P2P	0.647	0.663	0.754	0.679	0.406	0.668
MP_STD	0.759	0.706	0.818	0.759	0.476	0.706
MP_Dratio	0.011	0.497	0.182	0.011	0.064	0.727

Table 11: POD and FA after feature-level fusion and sensor-level fusion (1 of 7 votes for feature fusion; 3 of 6 votes for transducer pair fusion. Experiment #3, surface wetting case).

Feature	**Transducer Pairs**						**Sensor**
Fusion	1-2	1-3	1-4	2-3	2-4	3-4	**Fusion**
POD	0.856	0.877	0.947	0.979	0.963	0.984	0.963
FA	0.059	0.049	0.064	0.069	0.064	0.059	0.039
Min. hole diameter (mm)	2.0	2.0	1.5	2.0	1.5	1.5	1.5

fusion rather than search for the best features for the particular experiment. In fact, by including all features with different individual performances, the advantage of data fusion is clearer. For example, in Tables 10 and 11, for transducer pair 1-2, the probability of detection after feature fusion is better than for any individual feature. For transducer pair 1-4, the probability of detection after feature fusion is the same as that of the best individual feature "DCL". The improvement due to feature fusion using the 1 of 7 voting method is clearly shown by these results.

Table 11 also lists the results of sensor fusion. In addition to the probability of detection and false alarm rate, the smallest hole size that is always detected is calculated after feature fusion and sensor fusion. At this fusion level, the 3 of 6 voting method preserves a high probability of detection, reduces the false alarm rate and achieves 100% detection of the next to the smallest hole.

The data fusion results for the case of surface contact using brass bars are listed in Tables 12 and 13. As expected, the overall performance is not quite as good as the surface wetting case because the brass bar contact is inherently more difficult to discriminate from damage than surface wetting.

Table 12: POD for each feature and transducer pair with the preset false alarm rate of 2% (Experiment #3, surface contact case).

Features	**Transducer Pairs**					
	1-2	1-3	1-4	2-3	2-4	3-4
MSE	0.497	0.664	0.643	0.734	0.566	0.308
P_{xy}	0.636	0.476	0.525	0.608	0.168	0.441
Corr.	0.483	0.650	0.608	0.748	0.566	0.294
DCL	0.748	0.490	0.434	0.371	0.371	0.580
MP_P2P	0.434	0.014	0.566	0.357	0.007	0.063
MP_STD	0.559	0.077	0.832	0.546	0.308	0.210
MP_Dratio	0	0	0	0	0.014	0.210

Table 13: POD and FA after feature-level fusion and sensor-level fusion (1 of 7 votes for feature fusion; 3 of 6 votes for transducer pair fusion. Experiment #3, surface contact case).

Feature	**Transducer Pairs**						**Sensor**
Fusion	1-2	1-3	1-4	2-3	2-4	3-4	**Fusion**
POD	0.790	0.678	0.846	0.762	0.587	0.706	0.762
FA	0.104	0.082	0.077	0.099	0.066	0.077	0.039
Min. hole diameter (mm)	3.5	5.5	4.0	4.5	4.5	5.0	4.5

6.2.2 Feature Fusion for Experiments #1 and #2

For experiments #1 and #2, various surface condition changes are applied in addition to the temperature changes. As described in Chapter III, these surface condition changes include an oil-coupled aluminum block on the surface, oil drops on the surface, water on the surface, and partial immersion of the specimen into water.

The overall experimental data of these two experiments, including temperature variations and surface condition changes, can be analyzed according to the flow chart

of Fig. 32 proposed in Chapter V. First, a set of baselines covering the expected temperature range is recorded. Then, the procedure of baseline selection and correction is applied to obtain the best baseline matching the temperature of the monitored signal. Based on the best baseline and the monitored signal, the seven differential features introduced in Sec. 5.2 are extracted. Finally, a feature fusion method of voting is applied to reach the final declaration of the structural status; sensor fusion is not available since there is only one transducer pair for these experiments.

For experiment #1, 36 baselines covering temperatures from 5 °C to 40 °C are used, which provides the best temperature compensation result, as was shown in Sec. 6.1. A threshold is determined for each calculated feature using the data before damage occurs, and features are fused using a voting method. Four combinations of the preset false alarm rate and voting method are applied. They are (1) 0% preset false alarm rate followed by an "OR" operation (1 of 7 votes), (2) 2% preset false alarm rate followed by an "OR" operation (1 of 7 votes), (3) 10% preset false alarm rate followed by a majority vote (4 of 7 votes), and (4) 50% preset false alarm rate followed by a unanimous vote (7 of 7 votes). Table 14 lists the resulting probability of detection and false alarm rate for each feature fusion method.

As seen in Table 14, the performance of the first combination (0% FA, 1 of 7 votes) is poor. This is because for experiment #1, extreme surface condition changes are applied by partially immersing the specimen into water. When setting a 0% preset false alarm rate for each feature, these extreme conditions result in a very high threshold and thus a very low probability of detection for each feature, and the overall probability of detection cannot be significantly improved using feature fusion, even with the 1 of 7 voting method. The second combination is the same as the one chosen in Sec. 5.3 (the same preset false alarm rate for threshold selection and voting method for feature fusion). Because of the higher preset false alarm rate of 2%, the final probability of detection for this combination is much better than the first one.

Table 14: Experiment #1. Overall analysis

0% **Preset FA**	**Features**							**Feature**
1 of 7 votes	MSE	P_{xy}	Corr.	DCL	MP_P2P	MP_STD	MP_Dratio	**Fusion**
Threshold	0.65	0.96	0.59	0.89	0.86	0.78	0.72	POD = 0.010
POD	0.012	0.006	0.010	0.016	0.008	0.082	0.008	FA = 0
Min. notch (in.)	None	None	None	None	None	None	None	None
2% **Preset FA**								
1 of 7 votes	MSE	P_{xy}	Corr.	DCL	MP_P2P	MP_STD	MP_Dratio	
Threshold	0.47	0.84	0.41	0.81	0.62	0.74	0.55	POD = 0.502
POD	0.217	0.187	0.205	0.078	0.259	0.175	0.050	FA = 0.085
Min. notch (in.)	None	None	None	None	None	None	None	None
10% **Preset FA**								
4 of 7 votes	MSE	P_{xy}	Corr.	DCL	MP_P2P	MP_STD	MP_Dratio	
Threshold	0.29	0.73	0.24	0.74	0.50	0.58	0.41	POD = 0.675
POD	0.707	0.620	0.707	0.253	0.651	0.679	0.259	FA = 0.070
Min. notch (in.)	0.150	None	0.150	None	None	None	None	0.200
50% **Preset FA**								
7 of 7 votes	MSE	P_{xy}	Corr.	DCL	MP_P2P	MP_STD	MP_Dratio	
Threshold	0.04	0.08	0.03	0.56	0.18	0.17	0.25	POD = 0.803
POD	0.990	0.992	0.990	0.908	0.988	0.992	0.892	FA = 0.186
Min. notch (in.)	0.050	0.050	0.050	None	0.050	0.050	None	None

On the other hand, the final false alarm rate is increased to 8.5% because of the higher preset false alarm rate and the same 1 of 7 voting method. For both of these two combinations, there is no notch of any length which is always detected (i.e., even the largest notch is sometimes missed).

The third combination (10% FA, 4 of 7 votes) balances the preset false alarm rate and the voting method, which provides better fusion results. The final probability of detection is further improved compared to that of the second case, and the final false alarm rate is decreased because of the majority voting method. Moreover, a notch of length 0.200 in. or larger is always detected. For the last combination (50% FA, 7 of 7 votes), because the preset false alarm rate is too high, feature fusion even with unanimous voting can only reduce the overall false alarm to 18.6%, although

the overall probability of detection of 80.3% is the highest for the four cases. As the result of the unanimous voting, there is no notch length which is always detected.

The results here are not as good as those of experiment #3, which are listed in Tables 11 and 13. There are two factors contributing to the difference. First, results are skewed because of the two instances of partial immersion, which result in large defects always being missed. Second, multiple sensor fusion is not available for experiment #1, resulting in less information available than for experiment #3.

Table 15 lists the fusion results for experiment #2, where 27 baselines covering the full temperature range are used as the baseline set. The four combinations of preset false alarm rate and voting method used for experiment #1 are also compared here. In contrast to experiment #1, the first three combinations yield similar results for experiment #2. The first combination works for experiment #2 because no severe surface condition changes such as immersion were applied as was the case for experiment #1, so each feature has a much higher probability of detection even with a 0% preset false alarm rate. For the last combination (50% FA, 7 of 7 votes), because the feature "MP_Dratio" has a low probability of detection (0.4%) even with a preset false alarm rate of 50%, the final probability of detection is restricted to the same value due to the unanimous voting method.

For experiments #1 and #2, the probabilities of detection are 67.5% and 74%, respectively, using the third combination (10% FA, 4 of 7 votes). These values are comparable to the results of experiment #3 after only feature fusion. For example, for the brass bar contact case, transducer pair 1-2 provides a probability of detection of 79.0% and transducer pair 1-3 provides a probability of detection of 67.8% after feature fusion (Table 13). However, the overall performance of experiment #3 is better because of the additional sensor fusion, which demonstrates the advantage of data fusion from multiple sensors.

Table 15: Experiment #2. Overall analysis

0% **Preset FA**	**Features**							**Feature**
1 of 7 votes	MSE	P_{xy}	Corr.	DCL	MP_P2P	MP_STD	MP_Dratio	**Fusion**
Threshold	0.56	0.36	0.54	0.95	0.82	0.70	1.00	POD = 0.74
POD	0.48	0.74	0.48	0.14	0.24	0.48	0	FA = 0
Min. hole (in.)	0.219	0.141	0.219	None	None	None	None	0.141
2% **Preset FA**								
1 of 7 votes	MSE	P_{xy}	Corr.	DCL	MP_P2P	MP_STD	MP_Dratio	
Threshold	0.48	0.34	0.46	0.92	0.66	0.58	0.99	POD = 0.76
POD	0.68	0.74	0.68	0.22	0.60	0.64	0	FA = 0.10
Min. hole (in.)	0.172	0.141	0.156	None	None	0.219	None	0.141
10% **Preset FA**								
4 of 7 votes	MSE	P_{xy}	Corr.	DCL	MP_P2P	MP_STD	MP_Dratio	
Threshold	0.32	0.12	0.30	0.77	0.43	0.50	0.97	POD = 0.74
POD	0.74	0.98	0.74	0.80	0.94	0.74	0	FA = 0.10
Min. hole (in.)	0.141	0.109	0.141	0.141	0.125	0.156	None	0.141
50% **Preset FA**								
7 of 7 votes	MSE	P_{xy}	Corr.	DCL	MP_P2P	MP_STD	MP_Dratio	
Threshold	0.04	0.02	0.04	0.52	0.13	0.11	0.66	POD = 0.04
POD	1.00	1.00	1.00	1.00	1.00	1.00	0.04	FA = 0.15
Min. hole (in.)	0.078	0.078	0.078	0.078	0.078	0.078	None	None

6.3 Results of Phase Space Feature Extraction

In Sec. 5.4, the method of phase space feature extraction is introduced. It is based on the cross recurrence plot of the phase portraits reconstructed from a baseline and a monitored signal, and the feature is defined in Eq. 60. In this section, this feature extraction method is applied to experiments #1 and #2.

For the simplicity of computing, all signals recorded in the two experiments are down-sampled to 6.25 MHz and truncated to 500 μs, resulting in a total of 3125 points per waveform.

The Lorenz system is solved using the Runge-Kutta method, and the interval of integration is fixed at 0.16 μs to match the down-sampled sampling frequency of the diffuse ultrasonic signal. The parameter k of the system (Eq. 37) is chosen to

be 3×10^{-6}, which controls the oscillation of the Lorenz system so that the spectrum of the chaotic signal spans a similar range to that of ultrasonic signal. Figure 62 shows spectra of the ultrasonic signal, the chaotic signal, and the convolved signal. The chaotic signal is of length 250000 points, and the convolution is computed in the frequency domain. Each convolved signal has a length of 253124 points.

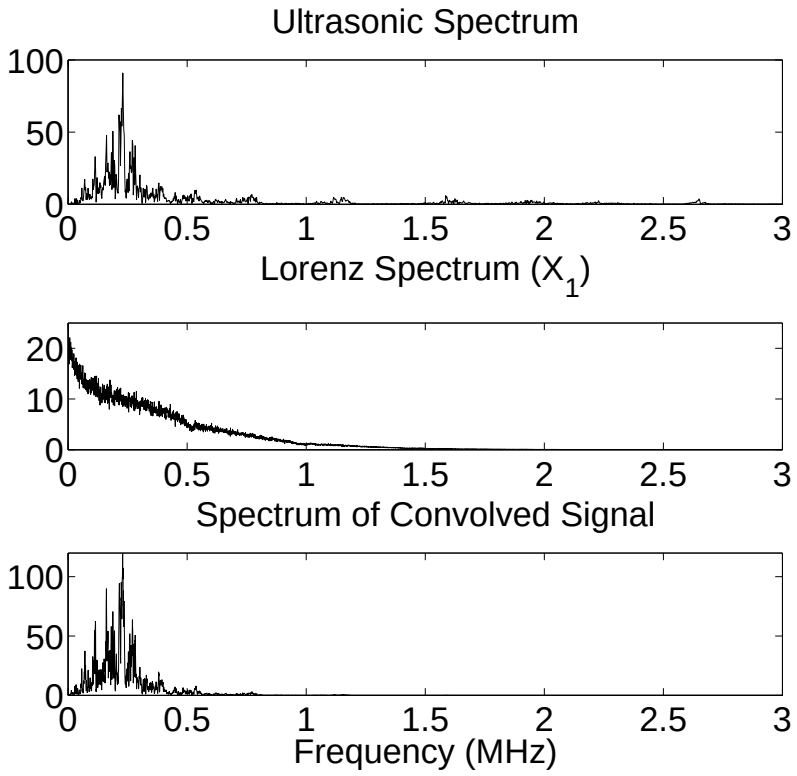

Figure 62: Spectra of signals of the convolution simulating the chaotic excitation.

To extract the differential feature "%*recurrence*" in phase space, a segment of 6250 points in the middle of the convolved signal is extracted for embedding. The extracted signal is embedded into two-, three-, four-, and five-dimensional spaces. Typical values of the box dimension were 1.87, 2.30, 2.86, and 2.88, respectively. According to the proposed method of determining the box dimension, $m = 3$ is used for embedding. The auto-correlation function is used to determine the time delay τ, and its optimal value is found to be eight sample intervals for all signals.

The efficacy of the feature is examined without the temperature and surface condition changes. For experiment #1, the baseline is the signal recorded at 25 °C from the undamaged specimen, and signals recorded at 25 °C for different notch sizes are compared to this baseline. For experiment #2, the same temperature is chosen, and signals from different hole sizes are compared to the baseline in phase space. Figures 63 and 64 plot the results of the phase space feature extraction for the two experiments. It can be seen that this feature is well correlated to the growth of damage for both experiments.

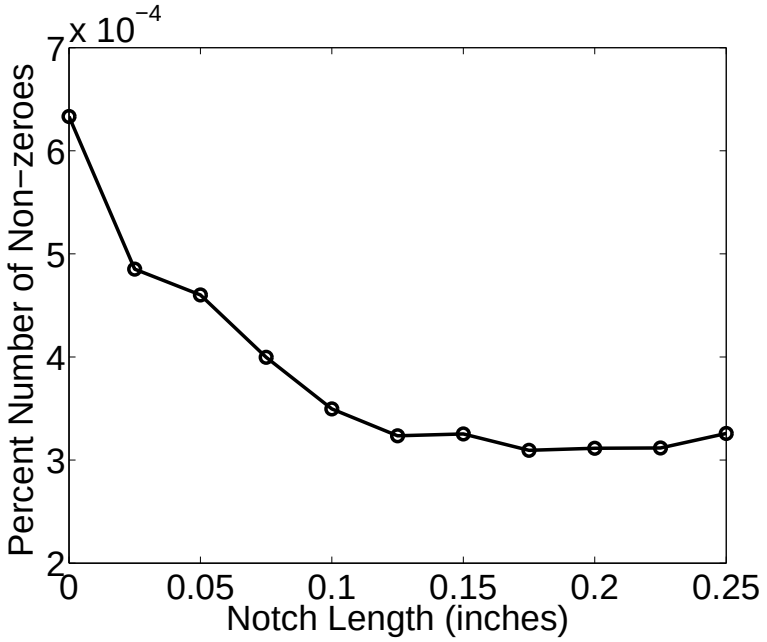

Figure 63: Percentage of non-zeros in the cross recurrence plot vs. flaw size: Experiment #1.

The results shown in this section are preliminary. The purpose of the introduction of the embedding theory and chaotic excitation, the simulation of the chaotic excitation, and the phase space feature extraction is to demonstrate the use of such control-related theories on the analysis of diffuse ultrasonic waves. A main concern with using such abstract feature extraction methods is how to relate the features to the underlying physical properties of the propagating waves and recorded signals.

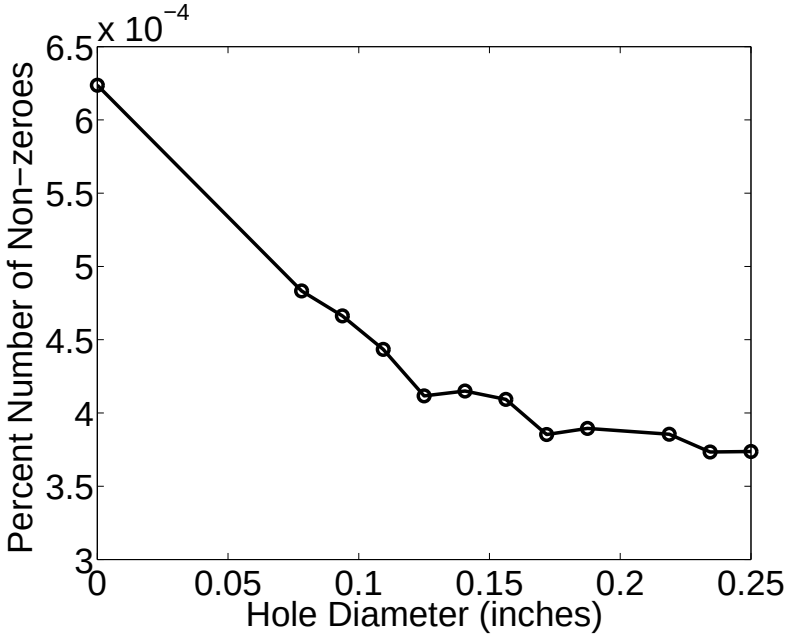

Figure 64: Percentage of non-zeros in the cross recurrence plot vs. flaw size: Experiment #2.

However, the results here demonstrate that the time series embedding theory and chaos theory can be valuable for diffuse ultrasonic signal analysis and suggest that more comprehensive future research is worthwhile.

CHAPTER VII

CONCLUSIONS AND RECOMMENDATIONS

7.1 Conclusions

This research provides several significant contributions to the analysis and modeling of diffuse ultrasonic waves, which lays the foundation for using diffuse ultrasonic waves for structural health monitoring.

First, this research studies the effect of temperature changes on diffuse ultrasonic waves. For a given temperature variation, the first order effect is a linear time shift of the waveform with respect to time of flight. The second effect is a waveform distortion which is proportional to the amount of the temperature change. These phenomena are illustrated and explained in Chapter IV using experimental data.

Based on these temperature effects, a systematic temperature compensation method is proposed for structural health monitoring systems using diffuse ultrasonic waves. The compensation method consists of pre-recording a set of baseline signals covering the expected temperature range followed by baseline selection and correction for each monitored signal. This compensation method provides a temperature matched baseline for a monitored signal recorded at an unknown temperature. The temperature compensation method is introduced in Chapter V.

Second, this research proposes the use of matching pursuit decomposition to analyze diffuse ultrasonic signals. A new implementation of the matching pursuit method is designed for ultrasonic signal decomposition, which can be used to identify discrete and overlapped ultrasonic echoes. To analyze diffuse ultrasonic signals, the concepts of distributed and constrained matching pursuit are proposed. According to these concepts, diffuse ultrasonic signals are represented by a sum of characteristic wavelets

obtained from matching pursuit decomposition. For structural health monitoring, differential features are extracted based on changes of the characteristic wavelets. The implementation method and the concepts of distributed and constrained matching pursuit are introduced in Chapter IV.

Third, in this research, various features of diffuse ultrasonic signals, including features based on the matching pursuit decomposition, are proposed and evaluated for their use in structural health monitoring. These features are selected with the consideration of their capabilities in discriminating benign surface condition changes, including surface wetting and contact, from actual structural changes. These features and their evaluation are presented in Chapter V.

Fourth, this research demonstrates the use of feature and sensor fusion to improve the overall performance of decision-making. Different voting methods are implemented for fusion and their effectiveness compared. The proposed data fusion methods are described in Chapter V.

Fifth, in this research, a phase space feature extraction method based on the theory of embedding and theory of chaos is implemented for diffuse ultrasonic waves, which is a novel application. The basic idea is to embed the diffuse ultrasonic signals into phase space and then extract features from the phase space with the methods used for chaotic signal analysis. The theories of embedding and chaos are introduced in Chapter IV and the phase space feature extraction method in Chapter V. Experimental results show potential for using such abstract mathematical theories in the analysis of diffuse ultrasonic signals.

7.2 Recommendations for Future Work

The scope of this thesis is damage detection for structural health monitoring using diffuse ultrasonic waves. Further research is necessary to provide the capability of damage localization and characterization.

Environmental changes are a major concern for a structural health monitoring system in a real environment. Compared to global temperature variations, thermal gradients and benign surface condition changes are more difficult to discriminate from structural changes. Although significant progress has been made here, particularly for homogeneous temperature changes and modest surface variations, additional research is necessary to extend the methodology to more extreme environmental changes.

Diffuse ultrasonic waves are inherently chaotic because they are formed after multiple reflections and scattering from specimen surfaces and microstructure. In addition to feature extraction, coupling the underlying chaotic characteristics of the diffuse ultrasonic signals with models based on chaos theory is a potentially promising approach requiring more research.

Finally, future research efforts must work towards providing a bridge to actual structures with realistic damage and operating conditions.

REFERENCES

[1] Ihn, J.-B. and Chang, F.-K., "Ultrasonic nondestructive evaluation for structural health monitoring: Built-in diagnostics for hot-spot monitoring in metallic and composite structures," in *Ultrasonic Nondestructive Evaluation* (Kundu, T., ed.), pp. 541–580, CRC Press, 2003.

[2] Doebling, S. W., "Damage identification and health monitoring of structural and mechanical system from changes in their vibration characteristics: A literature review," tech. rep., Los Alamos National Laboratory, LA-13070-MS, 1996.

[3] Liang, C., Sun, F. P., and Rogers, C. A., "Coupled electro-mechanical analysis of adaptive material systems - determination of the actuator power consumption and system energy transfer," *Journal of Intelligent Material Systems and Structures*, vol. 8, pp. 335–343, 1997.

[4] Park, G., "Overview of piezoelectric impedance-based health monitoring and path forward," *The Shock and Vibration Digest*, vol. 35, pp. 451–463, 2003.

[5] Zagrai, A. N. and Giurgiutiu, V., "Electro-mechanical impedance method for crack detection in thin plates," *Journal of Intelligent Material Systems and Structures*, vol. 12, no. 10, pp. 709–718, 2002.

[6] Farrar, C. R. and Doebling, S. W., "Structural health monitoring at Los Alamos National Laboratory," *Institute of Electrical Engineers Colloquium on Condition Monitoring: Machinery, External Structures and Health, Birmingham, UK*, 1999, LA-UR-1582.

[7] Ensminger, D., *Ultrasonics: Fundamentals, Technology, Applications*. Marcel Dekker, Inc., 1988.

[8] Giurgiutiu, V., Bao, J., and Zhao, W., "Piezoelectric wafer active sensor embedded ultrasonics in beams and plates," *Experimental Mechanics*, vol. 43, no. 4, pp. 428–449, 2003.

[9] Lin, M., Qing, X., Kumar, A., and Beard, S. J., "Smart layer and smart suitcase for structural health monitoring applications," in *Proceedings of the SPIE Conference on Smart Structures and Materials 2001-Industrial and Commercial Applications of Smart Structures Technologies*, vol. 4332, pp. 98–106, SPIE, 2001.

[10] Egle, D. M., "Diffuse wave fields in solid media," *Journal of the Acoustical Society of America*, vol. 70, no. 2, pp. 476–480, 1981.

[11] Weaver, R. L. and Lobkis, O. I., "Temperature dependence of diffuse field phase," *Ultrasonics*, vol. 38, no. 1-8, pp. 491–494, 2000.

[12] Achenbach, J. D., *Wave Propagation in Elastic Solids*. Elsevier Science Publishers B.V., 1993.

[13] Silk, M. G., "The determination of crack penetration using ultrasonic surface waves," *NDT International*, vol. 9, no. 6, pp. 290–297, 1976.

[14] Resch, M. T., London, B. D., Ramusat, G. F., Yuce, H. H., Nelson, D. V., and Shyne, J. C., "SAW NDE techniques for monitoring the growth behavior of small fatigue cracks," in *Review of Progress in Quantitative Nondestructive Evaluation*, vol. 3A, pp. 217–227, 1984.

[15] Resch, M. T., Shyne, J. C., Kino, G. S., and Nelson, D. V., "Long wavelength Rayleigh wave scattering from microscope surface fatigue cracks," in *Review of Progress in Quantitative Nondestructive Evaluation*, vol. 1, pp. 573–578, 1982.

[16] Khuri-Yakub, B. T., Kino, G. S., and Evans, A. G., "Acoustic surface wave measurement of surface cracks in ceramics," *Journal of American Ceramic Society*, vol. 63, no. 1-2, pp. 65–71, 1980.

[17] Cook, D. A. and Berthelot, Y. H., "Detection of small surface-breaking fatigue cracks in steel using scattering of Rayleigh waves," *NDT&E International*, vol. 34, pp. 483–492, 2001.

[18] Kim, J. K. and Rokhlin, S. I., "Surface acoustic wave measurements of small fatigue crack initiated from a surface cavity," *International Journal of Solids and Structures*, vol. 39, pp. 1487–1504, 2002.

[19] Kim, J. K., Yakovlev, V. A., and Rokhlin, S. I., "Surface acoustic wave modulation on a partially closed fatigue crack," *Journal of the Acoustical Society of America*, vol. 115, no. 5, pp. 1961–1972, 2004.

[20] Angel, Y. C., "Scattering of Love waves by a surface-breaking crack," *Journal of Applied Mechanics*, vol. 53, no. 3, pp. 587–592, 1986.

[21] Claus, R. O., "Electro-optical system for the detection of acoustic boundary waves," *Journal of Nuclear Materials*, pp. II.A.36–II.A.41, 1978.

[22] Rose, J. L., *Ultrasonic Waves in Solid Media*. Cambridge University Press, 1999.

[23] Smith, P. H., "Practical application of creeping waves," *British Journal of Non-Destructive Testing*, vol. 29, no. 5, pp. 318–321, 1987.

[24] Baby, S., Balasubramanian, T., and Pardikar, R. J., "Ultrasonic study for detection of inner diameter cracking in pipeline girth welds using creeping waves," *International Journal of Pressure Vessels and Piping*, vol. 80, no. 2, pp. 139–146, 2003.

[25] Giurgiutiu, V. and Cuc, A., "Embedded non-destructive evaluation for structural health monitoring, damage detection, and failure prevention," *The Shock and Vibration Digest*, vol. 37, no. 2, pp. 83–105, 2005.

[26] Rose, J. L., "Ultrasonic guided waves in structural health monitoring," *Key Engineering Materials*, vol. 270-273, no. 1, pp. 14–21, 2004.

[27] Rose, J. L., "A baseline and vision of ultrasonic guided wave inspection potential," *Journal of Pressure Vessel Technology*, vol. 124, no. 3, pp. 273–282, 2002.

[28] Rose, J. L., "Standing on the shoulders of giants: An example of guided wave inspection," *Materials Evaluation*, vol. 60, no. 1, pp. 53–59, 2002.

[29] Pilarski, A., Ditri, J. J., and Rose, J. L., "Remarks on symmetric Lamb waves with dominant longitudinal displacements," *Journal of the Acoustical Society of America*, vol. 93, no. 4, pp. 2228–2230, 1993.

[30] Hay, T. R. and Rose, J. L., "Guided wave testing optimization," *Materials Evaluation*, vol. 60, no. 10, pp. 1239–1244, 2002.

[31] Song, W.-J., Rose, J. L., and Whitesel, H., "An ultrasonic guided wave technique for damage testing in a ship hull," *Materials Evaluation*, vol. 61, no. 1, pp. 94–98, 2003.

[32] Murayama, R., "Non-destructive evaluation of formability in cold rolled steel sheets using the SH_0 mode plate wave by electromagnetic acoustic transducer," *Ultrasonics*, vol. 39, no. 5, pp. 335–343, 2001.

[33] Viktorov, I. A., *Rayleigh and Lamb Waves: Physical Theory and Applications*. Plenum Press, New York, 1967.

[34] Lemon, D. K. and Posakony, G. J., "Linear array technology in NDE applications," *Materials Evaluation*, vol. 38, no. 7, pp. 34–37, 1980.

[35] Joshi, S. P., "Feasibility study on phased array of interdigital mesoscale transducers for health monitoring of smart structures," in *Proceedings of the SPIE Conference on Smart Structures and Materials 1995: Smart Structures and Integrated Systems*, vol. 2443, pp. 248–257, SPIE, 1995.

[36] Joshi, S. G. and Jin, Y., "Excitation of ultrasonic Lamb waves in piezoelectric plates," *Journal of Applied Physics*, vol. 69, no. 12, pp. 8018–8024, 1991.

[37] Monkhouse, R. S. C., Wilcox, P. D., Lowe, M. J. S., Dalton, R. P., and Cawley, P., "The rapid monitoring of structures using interdigital Lamb wave transducers," *Smart Materials and Structures*, vol. 9, pp. 304–309, 2000.

[38] Rose, J. L., Pelts, S. P., and Quarry, M. J., "A comb transducer model for guided wave NDE," *Ultrasonics*, vol. 36, no. 1-5, pp. 163–169, 1998.

[39] Elyoubi, F., Grondel, S., and Assaad, J., "Signal processing for damage detection using two different array transducers," *Ultrasonics*, vol. 42, no. 1-9, pp. 803–806, 2004.

[40] Wooh, S.-C. and Shi, Y., "Synthetic phase tuning of guided waves," *IEEE Transactions on Ultrasonics, Ferroelectrics, and Frequency Control*, vol. 48, no. 1, pp. 209–223, 2001.

[41] Wilcox, P. D., "Omni-directional guided wave transducer arrays for the rapid inspection of large areas of plate structures," *IEEE Transactions on Ultrasonics, Ferroelectrics, and Frequency Control*, vol. 50, no. 6, pp. 699–709, 2003.

[42] Wilcox, P., Lowe, M., and Cawley, P., "Omnidirectional guided wave inspection of large metallic plate structures using EMAT array," *IEEE Transactions on Ultrasonics, Ferroelectrics, and Frequency Control*, vol. 52, no. 6, pp. 653–665, 2005.

[43] Giurgiutiu, V., Yu, L., and Thomas, D., "Embedded ultrasonic structural radar with piezoelectric wafer active sensors for damage detection in cylindrical shell structures," *Collection of Technical Papers - 45th AIAA/ASME/ASCE/AHS/ASC Struct., Struct. Dyn. and Mater. Conf.*, vol. 7, pp. 4984–4997, 2004.

[44] Yu, L., Bao, J., and Giurgiutiu, V., "Signal processing techniques for damage detection with piezoelectric wafer active sensors and embedded ultrasonic structural radar," in *Proceedings of the SPIE Conference on Smart Structures and Materials 2004 - Sensors and Smart Structures Technologies for Civil, Mechanical, and Aerospace Systems*, vol. 5391, pp. 492–503, SPIE, 2004.

[45] Tourin, A., Fink, M., and Derode, A., "Multiple scattering of sound," *Waves in Random Media*, vol. 10, pp. R31–R60, 2000.

[46] Weaver, R. L., "Diffusion of ultrasound in a glass bead slurry," *Journal of the Acoustical Society of America*, vol. 97, no. 4, pp. 2094–2102, 1995.

[47] Weaver, R. L., "Laboratory studies of diffuse waves in plates," *Journal of the Acoustical Society of America*, vol. 79, no. 4, pp. 919–923, 1986.

[48] Weaver, R. L., "On diffuse waves in solid media," *Journal of the Acoustical Society of America*, vol. 71, no. 6, pp. 1608–1609, 1982.

[49] Weaver, R. L., "Diffuse waves in finite plates," *Journal of Sound and Vibration*, vol. 94, no. 3, pp. 319–335, 1984.

[50] Page, J. H., Schriemer, H. P., Bailey, A. E., and Weitz, D. A., "Experimantal test of the diffusion approximation for multiply scattered sound," *Physical Review E*, vol. 52, no. 3, pp. 3106–3114, 1995.

[51] Schriemer, H. P., Cowan, M. L., Page, J. H., Sheng, P., Liu, Z., and Weitz, D. A., "Energy velocity of diffuse waves in strongly scattering media," *Physical Review Letters*, vol. 79, no. 17, pp. 3166–3169, 1997.

[52] Weaver, R., "Ultrasonics in an aluminum foam," *Ultrasonics*, vol. 36, no. 1-5, pp. 435–442, 1998.

[53] Anugonda, P., Wiehn, J. S., and Turner, J. A., "Diffusion of ultrasound in concretre," *Ultrasonics*, vol. 39, pp. 429–435, 2001.

[54] Becker, J., Jacobs, L. J., and Qu, J., "Characterization of cement-based materials using diffuse ultrasound," *Journal of Engineering Mechanics*, vol. 129, no. 12, pp. 1478–1484, 2003.

[55] Punurai, W., Jarzynski, J., Qu, J., Kurtis, K. E., and Jacobs, L. J., "Characterization of dissipation losses in cement paste with diffuse ultrasound," *Mechanics Research Communications*, vol. 34, pp. 289–294, 2007.

[56] Lobkis, O. I. and Weaver, R. L., "On the emergence of the Green's function in the correlations of a diffuse field," *Journal of the Acoustical Society of America*, vol. 110, no. 6, pp. 3011–3017, 2001.

[57] Michaels, J. E. and Michaels, T. E., "Detection of structural damage from the local temporal coherence of diffuse ultrasonic signals," *IEEE Transactions on Ultrasonics, Ferroelectrics, and Frequency Control*, vol. 52, no. 10, 2005.

[58] Egle, D. M., "A stochastic model for transient acoustic emission signals," *Journal of the Acoustical Society of America*, vol. 65, no. 5, pp. 1198–1203, 1979.

[59] Egle, D. M. and Brown, A. E., "A note on pseudo-acoustic emission sources," *Journal of Testing & Evaluation*, vol. 4, no. 3, pp. 196–199, 1976.

[60] Vary, A., "Acousto-ultrasonic characterization of fiber reinforced composites," *Materials Evaluation*, vol. 40, no. 6, pp. 650–654, 1982.

[61] Vary, A., "Acousto-ultrasonics: An update," in *Acoustic Emission: Current Practice and Future Directions* (Sachse, W., Roget, J., and Yamaguchi, K., eds.), pp. 95–104, 1989.

[62] Kiernan, M. T. and Duke, J. C., "Theoretical basis of the Acousto-Ultrasonic method," in *Acoustic Emission: Current Practice and Future Directions* (Sachse, W., Roget, J., and Yamaguchi, K., eds.), pp. 105–119, ASTM, 1989.

[63] Kautz, H. E., "Acousto-ultrasonics to assess material and structural properties," tech. rep., NASA/CR-2002-211881, 2002,.

[64] Kwon, O.-Y. and Lee, S.-H., "Acousto-ultrasonic evaluation of adhensively bonded CFRP-aluminum joints," *NDT&E International*, vol. 32, pp. 153–160, 1999.

[65] Shiloh, K., Bartors, A., Frain, A., and Lindgren, E., "Ultrasonic detection of corrosion between riveted plates," in *Proceedings of the SPIE Conference on Nondestructive Evaluation of Aging Aircrafts, Airports, and Aerospace Hardware IV*, vol. 3994, pp. 70–79, SPIE, 2000.

[66] Cosgriff, L. M., Martin, R. E., and Baaklini, G. Y., "Acousto-Ultrasonic characterization of C/SiC composite under different loading configurations," in *Proceedings of the SPIE Conference on Nondestructive Evaluation and Health Monitoring of Aerospace Materials and Composites II*, vol. 5046, pp. 71–78, SPIE, 2003.

[67] Liu, T., Kitipornchai, S., and Veidt, M., "Analysis of acousto-ultrasonic characteristics of contact-type transducers coupled to composite laminated plates," *International Journal of Mechanical Sciences*, vol. 43, pp. 1441–1456, 2001.

[68] Dugmore, K., Jonson, D., and Walker, M., "A comparison of signal consistency of common ultrasonic couplants used in the inspection of composite structures," *Journal of Testing & Evaluation*, vol. 58, pp. 601–603, 2002.

[69] Gyekenyesi, A. L., Harmon, L. M., and Kautz, H. E., "The effect of experimental conditions on acousto-ultrasonic reproducibility," in *Proceedings of the SPIE Conference on NDE and Health Monitoring of Aerospace Materials and Civil Infrastructures* (Gyekenyesi, A. L., Shepard, S. M., Huston, D. R., Aktan, A. E., and Shull, P. J., eds.), vol. 4704, pp. 177–186, SPIE, 2002.

[70] Lee, J.-R. and Tsuda, H., "Acousto-ultrasonic sensing using capsular fibre Bragg gratings for temperature compensation," *Measurement Science and Technology*, vol. 17, pp. 2920–2926, 2006.

[71] Barbezat, M., Brunner, A. J., Huber, C., and Flueler, P., "Integrated active fiber composite elements: Characterization for acoustic emission and acousto-ultrasonics," *International Journal of Material Systems and Structures*, vol. 18, pp. 515–525, 2007.

[72] Biemans, C., Staszewski, W. J., Boller, C., and Tomlinson, G., "Crack detection in metallic structures using broadband excitation of acousto-ultrasonics," *Journal of Intelligent Material Systems and Structures*, vol. 12, no. 8, pp. 589–597, 2001.

[73] Michaels, J. E., Cobb, A. C., and Michaels, T. E., "A comparison of feature-based classifiers for ultrasonic structural health monitoring," in *Proceedings of the SPIE Conference on Health Monitoring and Smart Nondestructive Evaluation of Structural and Biological Systems III* (Kundu, T., ed.), vol. 5394, pp. 363–374, SPIE, 2004.

[74] Wahab, A. M. and Roeck, G. D., "Effect of temperature on dynamic system parameters of a highway bridge," *Structural Engineering International*, vol. 7, pp. 266–279, 1997.

[75] Alampalli, S., "Influence of in-service environment on modal parameters," in *Proceedings of the 16th International Modal Analysis Conference*, vol. 1, pp. 111–116, SEM, Bethel, CT, USA, 1998.

[76] Rohrmann, R. G., Baessler, M., Said, S., Schmid, W., and Ruecker, W. F., "Structural causes of temperature affected modal data of civil structures obtained by long time monitoring," in *Proceedings of the SPIE Conference on Structural Dynamics, Computational Challenges in Structural Dynamics*, vol. 4062, pp. 1–7, SPIE, 2000.

[77] Yan, A. M., Kerschen, G., Boe, P. D., and Golinval, J. C., "Structural damage diagnosis under varying environmental conditions-Part I: A linear analysis," *Mechanical Systems and Signal Processing*, vol. 19, pp. 847–864, 2005.

[78] Kim, J.-T., Na, W.-B., Park, J.-H., and Lee, J.-S., "Structural health monitoring and risk alarming in plate-girder bridges under uncertain temperature condition," in *Proceedings of the SPIE Conference on Smart Structures and Materials, Sensors and Smart Structures, Technologies for Civil, Mechanical, and Aerospace systems*, vol. 5765, pp. 1002–1011, SPIE, 2005.

[79] Lobkis, O. I. and Weaver, R. L., "Coda-wave interferometry in finite solids: Recovery of P-to-S conversion rates in an elastodynamic billiard," *Physical Review Letters*, vol. 90, no. 254302, pp. 1–4, 2003.

[80] Snieder, R., Grêt, A., Douma, H., and Scales, J., "Coda wave interferometry for estimating nonlinear behavior in seismic velocity," *Science*, vol. 295, no. 5563, pp. 2253–2255, 2002.

[81] Mazzeranghi, A. and Vangi, D., "Methodology for minimizing effects of temperature in monitoring with the acousto-ultrasonic technique," *Experimental Mechanics*, vol. 39, no. 2, pp. 86–91, 1999.

[82] Rajic, N., Galea, S. C., and Chiu, W. K., "Autonomous detection of crack initiation using surface-mounted piezotransducers," *Smart Materials and Structures*, vol. 11, pp. 107–114, 2002.

[83] Lu, Y. and Michaels, J., "A methodology for strucutral health monitoring with diffuse ultrasonic waves in the presence of temperature variations," *Ultrasonics*, vol. 43, no. 9, pp. 717–731, 2005.

[84] Betz, D. C., Staszewski, W. J., Thursby, G., and Culshaw, B., "Structural damage identification using multifunctional Bragg grating sensors: II. damage detection results and analysis," *Smart Materials and Structures*, vol. 15, no. 5, pp. 1313–1322, 2006.

[85] Thursby, G. J., Maclean, A., Hogg, H., and Culshaw, B., "Ultrasound detection of damage in complex carbon fibre/metal structures," in *Proceedings of the SPIE Conference on Health Monitoring and Smart Nondestructive Evaluation of Structural and Biological Systems V*, vol. 6177, pp. 1–11, SPIE, 2006.

[86] Konstantinidis, G., Drinkwater, B. W., and Wilcox, P. D., "The temperature stability of guided wave structural health monitoring systems," *Smart Materials and Structures*, vol. 15, pp. 967–976, 2006.

[87] Croxford, A. J., Wilcox, P. D., Konstantinidis, G., and Drinkwater, B. W., "Strategies for overcoming the effects of temperature on guided wave structural health monitoring," in *Proceedings of the SPIE Conference on Health Monitoring and Smart Nondestructive Evaluation of Structural and Biological Systems III* (Kundu, T., ed.), vol. 6532, pp. 65321T–1–10, SPIE, 2007.

[88] Takatsubo, J., Wang, B., Tsuda, H., Toyama, N., and Urabe, K., "Ultrasonic spectroscopy for the identification of defects and environmental disturbances," *Transactions of the Japan Society of Mechanical Engineers. Series A*, vol. 72, no. 714, pp. 179–185, 2006.

[89] Baumeister, T., Avallone, E. A., and Baumeister, III, T., eds., *Marks' Standard Handbook for Mechanical Engineers.* McGraw-Hill Book Company, 1978.

[90] Salama, K. and Ling, C. K., "The effect of stress on the temperature dependence of ultrasonic velocity," *Journal of Applied Physics*, vol. 51, no. 3, pp. 1505–1509, 1980.

[91] Snieder, R., "Coda wave interferometry and the equilibrium of energy in elastic media," *Physical Review E*, vol. 66, no. 046615, pp. 1–8, 2002.

[92] Mallat, S. G. and Zhang, Z., "Matching pursuits with time-frequency dictionaries," *IEEE Transactions on Signal Processing*, vol. 41, pp. 3397–3415, 1993.

[93] Qian, S. and Chen, D., "Signal representation using adaptive normalized Gaussian functions," *Signal Processing*, vol. 36, pp. 1–11, 1994.

[94] Mallat, S., *A Wavelet Tour of Signal Processing*. San Diego: Academic Press, 1999.

[95] Hong, J.-C., Sun, K. H., and Kim, Y. Y., "The matching pursuit approach based on the modulated Gaussian pulse for efficient guided-wave damage inspection," *Smart Materials and Structures*, vol. 14, pp. 548–560, 2005.

[96] Raghavan, A. and Cesnik, C. E. S., "Guided-wave signal processing using chirplet matching pursuits and mode correlation for structural health monitoring," in *Proceedings of the SPIE Conference on Sensors and Smart Structures Technologies for Civil, Mechanical and Aerospace Systems* (Tomizuka, M., Yun, C.-B., and Giurgiutiu, V., eds.), vol. 6174, (Bellingham, Washington), pp. 61741B,1–12, SPIE, 2006.

[97] Ruiz-Reyes, N., Vera-Candeas, P., Curpian-Alonso, J., Cuevas-Martinez, J. C., and Lopez-Ferreras, F., "Matching pursuit-based approach for ultrasonic flaw detection," *Signal Processing*, vol. 86, pp. 962–970, 2006.

[98] Lu, Y. and Michaels, J., "Ultrasonic signal decomposition via matching pursuit with an adaptive and interpolated dictionary," in *Review of Progress in Quantitative Nondestructive Evaluation* (Thompson, D. O. and Chimenti, D. E., eds.), vol. 26A, pp. 579–586, 2007.

[99] Demirli, R. and Saniie, J., "Model-based estimation of ultrasonic echoes Part I: Analysis and algorithms," *IEEE Transactions on Ultrasonics, Ferroelectrics, and Frequency Control*, vol. 48, no. 3, pp. 787–802, 2001.

[100] Demirli, R. and Saniie, J., "Model-based estimation of ultrasonic echoes Part II: Nondestructive evaluation applications," *IEEE Transactions on Ultrasonics, Ferroelectrics, and Frequency Control*, vol. 48, no. 3, pp. 803–811, 2001.

[101] Demirli, R. and Saniie, J., "Model based time-frequency estimation of ultrasonic echoes for NDE," in *Proceedings of the IEEE Ultrasonics Symposium*, vol. 1, pp. 785–788, IEEE, 2000.

[102] Cardoso, G. and Saniie, J., "Ultrasonic data compression via parameter estimation," *IEEE Transactions on Ultrasonics, Ferroelectrics, and Frequency Control*, vol. 52, no. 2, pp. 313–325, 2005.

[103] Lu, Y., Demirli, R., Cardoso, G., and Saniie, J., "A successive parameter estimation algorithm for chirplet signal decomposition," *IEEE Transactions on Ultrasonics, Ferroelectrics, and Frequency Control*, vol. 53, no. 11, pp. 2121–2131, 2006.

[104] Hong, J.-C., Sun, K. H., and Kim, Y. Y., "Waveguide damage detection by the matching pursuit approach employing the dispersion-based chirp functions," *IEEE Transactions on Ultrasonics, Ferroelectrics, and Frequency Control*, vol. 53, no. 3, pp. 592–605, 2006.

[105] Gribonval, R. and Bacry, E., "Harmonic decomposition of audio signals with matching pursuit," *IEEE Transactions on Signal Proceessing*, vol. 51, no. 1, pp. 101–111, 2003.

[106] Czerepinski, P., Davies, C., Canagarajah, N., and Bull, D., "Matching pursuit video coding: Dictionaries and fast implementation," *IEEE Transactions on Circuits and Systems for Video Technology*, vol. 10, no. 7, pp. 1103–1115, 2000.

[107] McClure, M. R. and Carin, L., "Matching pursuit with a wave-based dictionary," *IEEE Transactions on Signal Processing*, vol. 45, no. 12, pp. 2912–2927, 1997.

[108] Bharadwaj, P. K., Runkle, P. R., and Carin, L., "Target identification with wave-based matching pursuits and hidden Markov models," *IEEE Transactions on Antennas and Propagation*, vol. 47, no. 10, pp. 1543–1554, 1999.

[109] Gribonval, R., "Fast matching pursuit with a multiscale dictionary of Guassian chirps," *IEEE Transactions on Signal Proceessing*, vol. 49, no. 5, pp. 994–1001, 2001.

[110] Yin, Q., Qian, S., and Feng, A., "A fast refinement for adaptive Gaussian chirplet decomposition," *IEEE Transactions on Signal Proceessing*, vol. 50, no. 6, pp. 1298–1306, 2002.

[111] Liu, Q., Wang, Q., and Wu, L., "Size of the dictionary in matching pursuit algorithm," *IEEE Transactions on Signal Processing*, vol. 52, no. 12, pp. 3403–3408, 2004.

[112] Giurgiutiu, V., "Tuned Lamb wave excitation and detection with piezoelectric wafer active sensors for structural health monitoring," *Journal of Intelligent Material Systems and Structures*, vol. 16, pp. 291–305, 2005.

[113] Fasel, T. R., Todd, M. D., and Park, G., "Piezoelectric active sensing using chaotic excitations and state space reconstruction," in *Proceedings of the SPIE Conference on Health Monitoring and Smart Nondestructive Evaluation of Structural and Biological Systems IV*, vol. 5768, pp. 253–263, SPIE, 2005.

[114] Nichols, J. M., Trickey, S. T., Todd, M. D., and Virgin, L. N., "Structural health monitoring through chaotic interrogation," *Meccanica*, vol. 38, no. 2, pp. 239–250, 2003.

[115] Sauer, T., Yorke, J. A., and Casdagli, M., "Embedology," *Journal of Statistical Physics*, vol. 64, no. 3/4, pp. 579–616, 1991.

[116] Takens, F., "Detecting strange attractors in turbulence," *in Lecture Notes in Mathematics, Dynamical Systems and Turbulence*, vol. 898, no. 6, pp. 366–381, 1981.

[117] Fraser, A. M. and Swinney, H. L., "Independent coordinates for strange attractors from mutual information," *Physical Review A*, vol. 33, no. 2, pp. 1134–1139, 1986.

[118] Kantz, H. and Schreiber, T., *Nonlinear Time Series Analysis*. University Press, Cambridge, 2004.

[119] Todd, M., Chang, L., Erickson, K., Lee, K., and Nichols, J., "Nonlinear excitation and attractor mapping for detecting bolt preload loss in an aluminum frame," in *Proceedings of the SPIE Conference on Health Monitoring and Smart Nondestructive Evaluation of Structural and Biological Systems III*, vol. 5394, pp. 317–328, 2004.

[120] Hay, T. R., Royer, R. L., Gao, H., Zhao, X., and Rose, J. R., "A comparison of embedded sensor Lamb wave ultrasonic tomography approaches for material loss detection," *Smart Materials and Structures*, vol. 15, no. 4, pp. 946–951, 2006.

[121] Zhang, L., Ume, C. I., Gamalski, J., and Galuschki, K.-P., "Detection of flip chip solder joint crack using correlation coefficient analysis of laser ultrasound signals," in *Proceedings of 54th Electronic Components and Technology Conference*, vol. 1, pp. 113–119, 2004.

[122] Hall, D. L. and Llinas, J., "An introduction to multisensor data fusion," *Proceedings of the IEEE*, vol. 85, no. 1, pp. 6–21, 1997.

[123] Varshney, P. K., "Multisensor data fusion," *Electronics & Communication Engineering Journal*, vol. 9, no. 6, pp. 245–253, 1997.

[124] Horn, D. and Mayo, W. R., "NDE reliability gains from combining eddy-current and ultrasonic testing," *NDT&E International*, vol. 33, no. 36, pp. 351–362, 2000.

[125] Liu, Q. C. and Wang, H.-P. B., "A case study on multisensor data fusion for imbalance diagnosis of rotating machinery," *Artificial Intelligence for Engineering Design, Analysis and Manufacturing*, vol. 15, no. 3, pp. 203–210, 2001.

[126] Sophian, A., Tian, G. Y., Taylor, D., and Rudlin, J., "A feature extraction technique based on principle component analysis for pulsed eddy current NDT," *NDT&E International*, vol. 36, no. 1, pp. 37–41, 2002.

[127] Nichols, J. M., Trickey, S. T., and Seaver, M., "Use of fiber optic sensors and recurrence quantification analysis in detecting and localizing damage in a thin steel plate," in *Proceedings of the SPIE Conference on Health Monitoring*

and Smart Nondestructive Evaluation of Structural and Biological Systems III, vol. 5394, pp. 329–339, SPIE, 2004.

VITA

Yinghui Lu was born in 1975 in Shanghai, China, and grew up in Shanghai, Jiujiang, and Wuhan. He attended the Zhejiang University in Hangzhou, China, and graduated with his Bachelor's degree in Electrical and Computer Engineering in 1996 .

Mr. Lu joined Shanghai Oil Refinery, a subsidiary company of China Petroleum and Chemical Corporation, in 1996. As an electrical engineer, he was involved in the design and field installation of industrial automation systems, electric machine drive systems, and real time power substation monitoring systems.

In 2000, he attended the University of Tennessee at Knoxville for graduate study in Electrical and Computer Engineering. From 2000 to 2002, he was a research assistant in the Power Electronics Laboratory where he developed a control platform for switched reluctance motors for the application of hybrid electric vehicles. He received his Master's degree from the University of Tennessee at Knoxville in 2002 and entered the Ph.D. program at the Georgia Institute of Technology in the same year. His doctoral research area is signal processing as applied to diffuse ultrasonic waves for structural health monitoring.